INVESTIGATION OF ION DIFFUSION IN CEMENTITIOUS MATERIALS WITH X-RAY IMAGING TECHNIQUES

By
AMIR BEHRAVAN
Bachelor of Science in Civil Engineering
Islamic Azad University-Khomeinishahr Branch
Isfahan, Iran
2009

Master of Science in Civil Engineering
Isfahan University of Technology
Isfahan, Iran
2012

Submitted to the Faculty of the
Graduate College of the
Oklahoma State University
in partial fulfillment of
the requirements for
the Degree of
DOCTOR OF PHILOSOPHY
July, 2020

INVESTIGATION OF ION DIFFUSION IN CEMENTITIOUS MATERIALS WITH X-RAY IMAGING TECHNIQUES

Dissertation Approved:

Dr. Matthew Tyler Ley

Dissertation Adviser

Dr. Norb Delatte

Dr. Julie Ann Hartell

Dr. Pankaj Sarin

ACKNOWLEDGEMENTS

This dissertation is based on several pieces of research conducted on the mass transport mechanism in cementitious materials. I am grateful for many faculties and friends who helped me finish this research and my Ph.D. study.

First, I would like to express my sincere appreciation to my advisor, Dr. Tyler Ley, for his continuous support of my Ph.D. study and research, for his patience, motivation, enthusiasm, and immense knowledge. His guidance helped me during the time of research and writing of this dissertation. Dr. Ley has consistently and enthusiastically given me valuable pieces of advice and suggestions that made this research unique.

Besides my advisor, I would like to thank the rest of my thesis committee: Dr. Norb Delatte, Dr. Julie Hartell, and Dr. Pankaj Sarin for their encouragement, insightful and constructive comments.

I would like to acknowledge the financial support from the Oklahoma Department of Transportation (ODOT), Federal Highway Association (FHWA), and the United States National Science Foundation (NSF).

The experimental works presented in this dissertation were performed in Bert Cooper Engineering, Advanced Technology Research Center, and Venture I Microscopy

Laboratories at Oklahoma State University. I would like to thank the technical staff of these laboratories who helped me run my experiments.

I would like to especially thank Professor Kerry Havner for his support through the “Havner Fellow Structures scholarship”.

I would like to extend my thanks to all my colleagues and friends at Oklahoma State University, especially, Dr. Dan Cook, Dr. Qinang Hu, Dr. Mehdi Khanzadeh Moradloo, Dr. Amir Hajibabaee, Anna Rywelski, and Alyssa Rogers, for their assistance and contributions to the content of this dissertation.

I want to thank my beloved wife and supportive family, for unconditionally loving and supporting me. I couldn't have done this journey without their love, inspiration, and endurance.

Name: AMIR BEHRAVAN

Date of Degree: JULY, 2020

Title of Study: INVESTIGATION OF ION DIFFUSION IN CEMENTITIOUS MATERIALS WITH X-RAY IMAGING TECHNIQUES

Major Field: CIVIL ENGINEERING

Abstract: The external penetration of ions into cementitious materials is the primary factor influencing the long-term durability of concrete structures. Most of the applied test methods to study ion transport in cement-based materials have some drawbacks and more importantly they cannot represent the exact multi-mechanistic transport of fluids into the concrete. It has been shown that the application of micro X-ray fluorescence (μXRF) and Transmission X-ray microscopy (TXM) helps to get a more fundamental observation of ion transport in a cementitious system. The present study uses the direct and non-destructive TXM technique to observe ion penetration into alternative cementitious materials (ACMs) paste samples cured for different durations. This work applies μXRF to compare the performance of ACMs in both laboratory and field applications. This study aims to develop a systematic approach to use a medical x-ray source to check the ion penetration into a cementitious system which is a rapid non-destructive x-ray technique. This work shows the CHIP is a reliable technique to measure the mass transport properties of a system. The results from this study help to expand our understanding of ion transport in cement-based materials and to greatly improve the current models of mass transport and service life predictions of the concrete.

TABLE OF CONTENTS

Chapter Page

Chapter Page

Chapter Page

Chapter Page

Chapter Page

Chapter Page

Chapter Page

LIST OF TABLES

Table Page

Table Page

LIST OF FIGURES

Figure Page

Figure Page

Figure Page

Figure Page

Figure Page

CHAPTER I

INTRODUCTION

1.1. Overview

The durability performance of concrete depends on different factors that can be classified into two main groups. The first group refers to the type of deterioration agent and its intensity acting on the concrete, and the deterioration mechanism involved in concrete degeneration. The second group refers to the concrete quality and its resistance to physical factors (like freeze/thaw, erosion, abrasion, fatigue, temperature, and humidity changes) or chemical factors (like corrosion, carbonization, and aggressive material ingress) or even biological impacts (like living microorganisms, animals, or plants growth) [1]. Several concrete durability problems are depending mainly on the mass transport properties of concrete. Transported matter can be various liquids, gases, dissolved, and more or less aggressive ions, concrete constituents, etc. [2]. Since free water usually acts as the carrier of destructive ions into the bulk concrete, therefore, fluid transport properties of concrete materials play an important role in the durability performance of concrete structures. It is desirable to develop methods, which can be used to it is desired to study fluid transport properties like porosity, permeability, ionic diffusivity, and the ionic binding capability of concrete to predict the service life span of the concrete structures [3]. Permeability,

defined as the movement of fluid through a porous medium under an applied pressure head [4]. Permeability of concrete depends on the porosity, arrangement of pores, and microcracks in the concrete [4]. Porosity gives the percentage of the total volume of pores that exist in a unit volume of concrete. The ionic diffusivity of concrete is the rate of movement of an ion from an area of high concentration to an area of low concentration. Ion diffusion into concrete is a multi-mechanism process; it means a combination of several parameters affects the diffusion coefficient in which each parameter is investigated fragmentally. Many past research projects have approved that parameters like water-to-cement ratio (w/c), curing method, temperature, ion type, relative humidity, various cementitious materials, porosity and permeability, using different binders, surface treatments, interaction between two or more effective parameters, type of stressor environment and the number of cycles, are highly important parameters influencing the ion diffusion into concrete [6–23].

1.2. Measuring fluid transport into concrete

Between all of the harmful external species and ions, chlorides have become a major concern due to the localized corrosion of embedded steel bars without noticeable damage to the cement matrix. The chloride content and rate of penetration of concrete can be investigated through a number of methods including: AASHTO T259 (salt ponding test) [24], ASTM C 1556 (bulk diffusion test) [25], silver nitrate spray on the surface (colorimetric technique) [26,27], AASHTO T277 (rapid chloride permeability test) [28–32], AASHTO T260 (Potentiometric Titration or Ion-Selective Electrode) [33,34] electrical migration [35–37], resistivity [38,39], pressure-induced fluid penetration [40], sorptivity [41,42], solvent counter diffusion [43], and gas diffusion [44]. Most of the applied test methods are not a reliable indicator of ion diffusion into the blended binders because of the difference in the pore solution chemistry induced by using different alternative cementitious materials or admixtures. Also, some of the current test methods are time consuming and destructive. Furthermore, most of the established test methods in the field of investigation of ion ingress into concrete cannot represent the exact multi-mechanistic transport of fluids into the concrete. In reality, harmful ions

transport into concrete under different mechanisms like diffusion, absorption, permeation, electromigration, convection, and wicking [45,46]. Also, in most of the current test methods, chemical reactions between the diffused ions and cement (binding effect) are not considered. Moreover, some of these methods are destructive, sensitive to the defects and cracks, moisture content, temperature, pore solution chemistry, etc. For this reason, these methods cannot provide fundamental observation of the mass transport properties of concrete. Therefore, a technique is needed that is rapid, non-destructive, and able to provide fundamental observations of fluid movement in concrete materials with high spatial resolution. One solution to this problem would be to use an x-ray imaging technique. X-ray imaging is considered a non-destructive technique because it does not destroy a sample and the same sample can be tested several times to monitor a change in the sample over time or the same sample can be used in another experiment.

1.3. X-ray imaging techniques to quantify mass transport in concrete

Three x-ray imaging techniques that are non-destructive to the sample to quantify mass transport in cement-based materials address some of the drawbacks of the current techniques in this field of study and summarized different mechanisms acting on the concrete in just one term of diffusion coefficient. Micro-analysis X-ray imaging techniques used in these three methods were micro X-ray fluorescence (μXRF), transmission X-ray microscopy (TXM), and checking ion penetration (CHIP). μXRF and TXM have been developed as reliable methods for investigation of fluid transport into concrete but CHIP will be introduced and established in this dissertation for the first time.

1.3.1. Micro X-ray fluorescence (μXRF)

μXRF is a powerful method for materials characterization. μXRF maps the distribution of the chemical elements in the sample and discern between the aggregate and the paste with the minimal human intervention [47]. This technique can detect a wide range of chemical elements from sodium to curium. The detection limits of the technique depend on the thickness of the detector window and the distance

to the sample-detector [48]. The instrument uses a stage to move the sample under a fixed x-ray beam. Once an x-ray photon exceeds the ionization energy of an inner shell electron, the latter electron may be ejected, producing a vacancy in the corresponding orbital. Subsequently, an electron from an upper orbital fills this vacancy, and the excess of energy can be emitted as a photon. The emitted energy is characteristic for each chemical element; thus, one can use this energy to identify each chemical element [49]. The x-ray detector counts the number of photons emitted from the sample at each location. This data is used to create elemental maps. Moreover, the number of emitted photons is directly proportional to the amount of emitting atoms. In other words, the brightness of each point on each map is an indication of the concentration level of each element at each point which can help to identify local abnormalities like cracks, chloride rich aggregates, or the presence of surface treatments.

1.3.2. Transmission X-ray microscopy (TXM)

TXM works similarly to the radiography technique that doctors use. In this technique, each sample is loaded on a fixed stage between the x-ray source and the detector. When x-rays are used to investigate the sample, some x-rays are absorbed, and others pass the sample to reach the detector. The detector produces grayscale images called radiographs based on the received x-rays. Radiographs are grayscale images in which each pixel has a gray value between “0” and “255”. Pure black has a gray value of “0” and pure white has a gray value of “255”. The gray values change by density, thickness, chemistry, or a combination of these. This method projects 3D data with high spatial resolution in 2D to obtain greater insight into the mechanisms of fluid transport into cement-based materials. Also, because this method is non-destructive it can be used to conduct in-situ imaging.

1.3.3. Checking Ion Penetration (CHIP)

Another technique that can be applied is using medical x-ray sources. This method is very similar to the TXM but more economical and faster. The only differences were the x-ray source and x-ray settings. Like TXM, the sample is loaded on a fixed stage between the x-ray source and a sensor (detector).

When the x-ray source is energized, some x-rays are absorbed in the sample, and some others pass the sample to reach the detector. The detector projects 3D information on a 2D radiograph from the received x-rays. Like TXM, captured radiographs are grayscale images in which each pixel has a value between "0" and "255". Contrary to TXM, in the CHIP method, 255 represents white regions which correspond to a maximum density. On the other hand, zero value represents black spots as a minimum density such as air in the background of each radiograph.

1.4. Research Objectives

Investigation of fluid transport properties in cementitious materials by using x-ray imaging techniques will considerably improve the current test methods in this field. These methods can enhance the current models of mass transport and service life predictions of the concrete by providing effective diffusion coefficient and surface concentration values to the modeler. This study aims to use micro X-ray fluorescence (μXRF) and Transmission X-ray microscopy (TXM) to study ion transport in different cementitious systems. Moreover, this study aims to develop a systematic approach to use the CHIP (Checking Ion Penetration) method which uses medical x-ray sources and works similar to TXM to investigate mass transport within cement-based materials as a faster and less expensive test method than TXM.

The main objectives of this research are to apply X-ray imaging techniques on different cementitious systems to study mass transport. The objectives of this study are explained in more details below:

1- Most of the current laboratory x-ray equipment is expensive, time-consuming, need sample preparation, specific machine training, special x-ray safety training to protect both the operators and the public. As a solution, the research team developed a dental X-ray radiography (CHIP) approach to investigate mass transport in the cement-based materials as a fast and cheap NDT test method. Since the newly established CHIP method has not the mentioned limitations of the existing laboratory x-ray equipment, it has both scientific and industrial applications. This new

method allows the experimenter to perform a greater number of tests in a laboratory or field in a relatively short time compared to the other techniques.

2- In recent years, ACMs have been increasingly used as a full or partial replacement of ordinary Portland cement (OPC) for concrete structures. These ACMs have been used sometimes because of their rapid hardening and early age strength gain that can allow traffic loads in a few hours. However, very little research has been conducted on these ACMs to understand the resistance to chloride penetration. This study aims to investigate the resistance of ACMs to chloride penetration both in the field and laboratory to investigate to what extent laboratory results are comparable with the field results.

3- One challenge with alternative cementitious materials (ACMs) is the lack of published information regarding their use and performance. Also, the use of many of the previous test methods is challenging to interpret because of differences in chemical composition and a lack of fundamental measurement data with which to compare these accelerated or indirect measurements. For this reason, the present study uses a direct and non-destructive X-ray mapping method called transmission X-ray microscopy (TXM) to observe iodide penetration into ACMs paste samples cured for different durations. The goal of this chapter is to apply the TXM technique to investigate the impact of curing time extension on the ACMs.

4- In most of the current test methods, chemical reactions between the diffused ions and cement (binding effect) are not considered. On the other hand, because of the difference of different fly ashes and their relative effectiveness and different curing times applied in different studies, there is not a consensus among the researchers on the potential of ion binding in cement-fly ash paste and concrete. Moreover, the beneficial effects of fly ash on permeability and diffusivity tend to become more apparent with time. This study investigates the impact of curing time on the ion diffusivity of blended cement pastes partially replaced with seven types

of fly ash. This work uses dental x-ray radiography (called checking ion penetration or CHIP) to image the movement of fluids in blended cement pastes.

1.5. Overview of Dissertation

This dissertation is written in a paper-based format. Each chapter is described as below:

Chapter 1: In this chapter, some basic information and definitions are presented as an introduction to show the importance of this study.

Chapter 2: in this chapter TXM was used to investigate the impact of curing time extension on the mass transport properties of ACMs. Four commercially available ACMs and an ordinary Portland cement are considered to make paste samples. Samples are cured from 35 days up to 365 days. The applied method shows the resistance of different cement-based materials with different chemistry against ion intrusion. Also, in this study, the impact of curing time on the mass transport properties of the considered materials is investigated.

Chapter 3: In this chapter, μXRF was applied to investigate the mass transport properties in ACMs field samples. Field samples gathered from four different sites to be tested. The test procedure followed here is the same experimental procedure was followed in the previous research in the lab done by Dr. Khanzadeh Moradloo. The results of the lab and field results are compared with each other. Both methods showed that laboratory testing can provide good insights to the performance of some ACMs while for calcium aluminum cement older laboratory samples may require to get acceptable insight into this material performance.

Chapter 4: This chapter presents the novel method of using CHIP, a fast and non-destructive test method, an economic imaging technique compared to the similar established test methods, to study mass transport into cement-based materials. CHIP is considered as a non-destructive test method because the sample which is used in this imaging technique can be used to scan several times to monitor

a change in the same sample over time or that sample can be used for another experiment after completing the CHIP imaging. Results from CHIP were compared to TXM and good agreement was found.

Chapter 5: In this chapter, CHIP was used to investigate the impact of curing time extension on the mass transport properties of fly ashes. Paste samples with a 20% replacement of cement with seven types of fly ashes were prepared. The samples were cured from 45 days up to 135 days. Similar to chapter three, the mass transport properties change at different curing times is studied.

Chapter 6: This final chapter summarizes all the findings of this study and discusses the main conclusions of the current dissertation. Suggestions for future work are also provided.

All of the researches presented in this dissertation are based on the work performed by the author at Oklahoma State University between the years 2016 and 2020. Each chapter was completed with help from several undergraduate researchers. These students are Alyssa Rogers, Anna Rywelsky, Megan Buchanan. These students helped to cast samples and to prepare the samples for each test. Special thanks to Anna Rywelski for her help in x-ray imaging.

References

[1] J. Hoła, J. Bień, K. Schabowicz, Non-destructive and semi-destructive diagnostics of concrete structures in assessment of their durability, Bulletin of the Polish Academy of Sciences Technical Sciences. 63 (2015) 87–96.

[2] S. Jacobsen, Calculating liquid transport into high-performance concrete during wet freeze/thaw, Cement and Concrete Research. 35 (2005) 213–219.

[3] Y. Wang, L. Li, C.L. Page, Modelling of chloride ingress into concrete from a saline environment, Building and Environment. 40 (2005) 1573–1582.

[4] N. Banthia, A. Biparva, S. Mindess, Permeability of concrete under stress, Cement and Concrete Research. 35 (2005) 1651–1655. doi:https://doi.org/10.1016/j.cemconres.2004.10.044.

[5] M.H.F. Medeiros, P. Helene, Surface treatment of reinforced concrete in marine environment : Influence on chloride diffusion coefficient and capillary water absorption, Construction and Building Materials. 23 (2009) 1476–1484. doi:10.1016/j.conbuildmat.2008.06.013.

[6] F. Leng, N. Feng, X. Lu, An experimental study on the properties of resistance to diffusion of chloride ions of fly ash and blast furnace slag concrete, Cement and Concrete Research. 30 (2000) 989–992. doi:https://doi.org/10.1016/S0008-8846(00)00250-7.

[7] M. Khanzadeh Moradllo, M.T. Ley, Quantitative measurement of the influence of degree of saturation on ion penetration in cement paste by using X-ray imaging, Construction and Building Materials. 141 (2017) 113–129. doi:10.1016/J.CONBUILDMAT.2017.03.007.

[8] A. Meyer, Importance of the Surface Layer for the Durability of Concrete Structures, Special Publication. 100 (1987). doi:10.14359/2608.

[9] S. Caré, Effect of temperature on porosity and on chloride diffusion in cement pastes, Construction and Building Materials. 22 (2008) 1560–1573. doi:https://doi.org/10.1016/j.conbuildmat.2007.03.018.

[10] A. Djerbi, S. Bonnet, A. Khelidj, V. Baroghel-bouny, Influence of traversing crack on chloride diffusion into concrete, Cement and Concrete Research. 38 (2008) 877–883. doi:https://doi.org/10.1016/j.cemconres.2007.10.007.

[11] V.T. Ngala, C.L. Page, Effects Of Carbonation On Pore Structure And Diffusional Properties Of Hydrated Cement Pastes, Cement and Concrete Research. 27 (1997) 995–1007. doi:https://doi.org/10.1016/S0008-8846(97)00102-6.

[12] R.V.S. Anna V. Saetta and Renato V. Vitaliani, Analysis of Chloride Diffusion into Partially Saturated Concrete, Materials Journal. 90 (1993). doi:10.14359/3874.

[13] V.G. Papadakis, Effect of supplementary cementing materials on concrete resistance against carbonation and chloride ingress, 30 (2000) 291–299.

[14] T. Sugiyama, T.W. Bremner, Y. Tsuji, Determination of chloride diffusion coefficient and gas permeability of concrete and their relationship, Cement and Concrete Research. 26 (1996) 781–790. doi:https://doi.org/10.1016/S0008-8846(96)85015-0.

[15] K. Hong, R.D. Hooton, Effects of cyclic chloride exposure on penetration of concrete cover, Cement and Concrete Research. 29 (1999) 1379–1386. doi:https://doi.org/10.1016/S0008-8846(99)00073-3.

[16] M.D.A. Thomas, R.D. Hooton, A. Scott, H. Zibara, The effect of supplementary cementitious materials on chloride binding in hardened cement paste, Cement and Concrete Research. 42 (2012) 1–7. doi:https://doi.org/10.1016/j.cemconres.2011.01.001.

[17] J. Liu, Q. Qiu, X. Chen, F. Xing, N. Han, Y. He, Y. Ma, Understanding the interacted mechanism between carbonation and chloride aerosol attack in ordinary Portland cement concrete, Cement and Concrete Research. 95 (2017) 217–225. doi:https://doi.org/10.1016/j.cemconres.2017.02.032.

[18] D. Conciatori, F. Laferrière, E. Brühwiler, Comprehensive modeling of chloride ion and water ingress into concrete considering thermal and carbonation state for real climate, Cement and Concrete Research. 40 (2010) 109–118. doi:https://doi.org/10.1016/j.cemconres.2009.08.007.

[19] A. Ben Fraj, S. Bonnet, A. Khelidj, New approach for coupled chloride/moisture transport in non-saturated concrete with and without slag, Construction and Building Materials. 35 (2012) 761–771. doi:https://doi.org/10.1016/j.conbuildmat.2012.04.106.

[20] A. Behravan, Z. Ahmadi, Laboratory Analysis of Barchip Fiber-Reinforced Concrete Durability Inside the lining of Water Supply Tunnels, International Conference of Civil Engineering, Architecture and Urbanization in Contemporary Iran-Tehran, August (2017).

[21] A. Hajibabaee, M. Khanzadeh Moradllo, A. Behravan, M.T. Ley, Quantitative measurements of curing methods for concrete bridge decks, Construction and Building Materials. 162 (2018) 306–313. doi:10.1016/J.CONBUILDMAT.2017.12.020.

[22] M.K. Moradllo, L. Montanari, P. Suraneni, S.R. Reese, J. Weiss, Examining Curing Efficiency using Neutron Radiography, Transportation Research Record. (2018) 0361198118773571. doi:10.1177/0361198118773571.

[23] M. Khanzadeh Moradllo, M.T. Ley, Comparing ion diffusion in alternative cementitious materials in real time by using non-destructive X-ray imaging, Cement and Concrete Composites. 82 (2017) 67–79.

[24] AASHTO T 259, Resistance of Concrete to Chloride Ion Penetration, (1980).

[25] ASTM C1556, Standard Test Method for Determining the Apparent Chloride Diffusion Coefficient of Cementitious Mixtures by Bulk Diffusion, (2016).

[26] E. Meck, V. Sirivivatnanon, Field indicator of chloride penetration depth, Cement and Concrete Research. 33 (2003) 1113–1117.

[27] V. Baroghel-Bouny, P. Belin, M. Maultzsch, D. Henry, AgNO3 spray tests: advantages, weaknesses, and various applications to quantify chloride ingress into concrete. Part 2: Non-steady-state migration tests and chloride diffusion coefficients, Materials and Structures. 40 (2007) 783.

[28] AASHTOT 277-93, Electrical Indication of Concrete's Ability to Resist Chloride, (1983).

[29] ASTM C1202-19, Standard Test Method for Electrical Indication of Chloride's Ability to Resist Chloride, (2019).

[30] T. Zhang, O.E. Gjørv, An electrochemical method for accelerated testing of chloride diffusivity in concrete, Cement and Concrete Research. 24 (1994) 1534–1548.

[31] R.K. Dhir, M.R. Jones, H.E.H. Ahmed, A.M.G. Seneviratne, Rapid estimation of chloride diffusion coefficient in concrete, Magazine of Concrete Research. 42 (1990) 177–185.

[32] P.E. Streicher, M.G. Alexander, A chloride conduction test for concrete, Cement and Concrete Research. 25 (1995) 1284–1294.

[33] AASHTO T260-94, Standard Method for Sampling and Testing for Chloride Ion in Concrete and Concrete Raw Materials, (1994).

[34] M.A. Climent, G. de Vera, J.F. López, E. Viqueira, C. Andrade, A test method for measuring chloride diffusion coefficients through nonsaturated concrete: Part I. The instantaneous plane source diffusion case, Cement and Concrete Research. 32 (2002) 1113–1123.

[35] A. Delagrave, J. Marchand, E. Samson, Prediction of diffusion coefficients in cement-based materials on the basis of migration experiments, Cement and Concrete Research. 26 (1996) 1831–1842.

[36] C. Ozyildirim, Rapid Chloride permeability testing of sílica-fume concrete, Cement, Concrete and Aggregates. 16 (1994) 53–56.

[37] A.A. Kyi, B. Batchelor, An electrical conductivity method for measuring the effects of additives on effective diffusivities in portland cement pastes, Cement and Concrete Research. 24 (1994) 752–764.

[38] C. Andrade, C. Alonso, S. Goni, Possibilities for electrical resistivity to universally characterise mass transport processes in concrete, Proceedings of the Concrete 2000 Conference. 2 (1993) 1639–1652.

[39] C. Andrade, Calculation of chloride diffusion coefficients in concrete from ionic migration measurements, Cement and Concrete Research. 23 (1993) 724–742.

[40] P. Halamickova, R.J. Detwiler, D.P. Bentz, E.J. Garboczi, Water permeability and chloride ion diffusion in Portland cement mortars: relationship to sand content and critical pore diameter, Cement and Concrete Research. 25 (1995) 790–802.

[41] C. Hall, Water sorptivity of mortars and concretes: a review, Magazine of Concrete Research. 41 (1989) 51–61.

[42] N.S. Martys, C.F. Ferraris, Capillary transport in mortars and concrete, Cement and Concrete Research. 27 (1997) 747–760.

[43] R.F. Feldman, Diffusion measurements in cement paste by water replacement using propan-2-ol, Cement and Concrete Research. 17 (1987) 602–612.

[44] A. Sharif, K.F. Loughlin, A.K. Azad, C.M. Navaz, Determination of the effective chloride diffusion coefficient in concrete via a gas diffusion technique, Materials Journal. 94 (1997) 227–233.

[45] M.D.A. Thomas, P.B. Bamforth, Modelling chloride diffusion in concrete: Effect of fly ash and slag, Cement and Concrete Research. 29 (1999) 487–495.

[46] A. Boddy, E. Bentz, M.D.A. Thomas, R.D. Hooton, An overview and sensitivity study of a multimechanistic chloride transport model, Cement and Concrete Research. 29 (1999) 827–837. doi:https://doi.org/10.1016/S0008-8846(99)00045-9.

[47] M.K. Moradllo, Use of Non-Destructive X-Ray Microscopic Techniques to Study Fluid Transport in Cement-Based Materials, (2016).

[48] M. Haschke, Laboratory micro-X-Ray fluorescence spectroscopy, Springer International Publishing. 10 (2014) 978–983.

[49] E.S. Rodrigues, M.H.F. Gomes, N.M. Duran, J.G.B. Cassanji, T.N.M. da Cruz, A. Sant'Anna Neto, S.M. Savassa, E. de Almeida, H.W.P. Carvalho, Laboratory Microprobe X-Ray Fluorescence in Plant Science: Emerging Applications and Case Studies, Frontiers in Plant Science . 9 (2018) 1588. https://www.frontiersin.org/article/10.3389/fpls.2018.01588.

CHAPTER II

IMPACT OF CURING TIME ON THE MASS TRANSPORT OF ALTERNATIVE CEMENTITIOUS MATERIALS

Abstract

Cement manufacturing is responsible for 5% of the yearly global emission of greenhouse gases. Because alternative cementitious materials (ACMs) have a lower carbon footprint, this can reduce cement consumption and consequently decrease the carbon footprint of concrete. In this study, the impact of extending the curing time on the selected ACMs is investigated by using the transmission X-ray microscopy (TXM) method. In this method, samples were scanned at different intervals after ponding with a potassium iodide salt solution as a tracer. Afterward, images obtained from the TXM were analyzed to derive the effective diffusion coefficient. This work shows that with time the conversion of calcium aluminate cement causes a detrimental impact on the diffusion coefficient that seems to be caused by cracking. The work also quantifies the reduction in the diffusion coefficient for mixtures with calcium sulfoaluminate cement, alkali-activated, and ordinary Portland cements over time.

Keywords: X-ray microscopy, Calcium aluminate cement, Calcium sulfoaluminate cement, Alkali-activated binders, Durability, Curing time

2.1.Introduction

The cement industry contributes 5% of the global emission of carbon dioxide (CO_2) because of the consumption of fossil fuels, extensive grinding, and the calcining of limestone [1]. In order to achieve sustainable concrete researchers have begun to investigate alternative cementitious materials (ACMs) to use instead of ordinary Portland cement (OPC) in concrete. One concern is the long-term durability performance of concretes made with ACMs [2].

A major concern with concrete durability is the corrosion of reinforcing steel due to the chloride (Cl) transport into the concrete [3]. The sources of Cl ions are typically deicing salts, ocean water, or contaminated aggregates [4–6]. Cl causes localized corrosion of embedded steel bars leading to load-carrying reduction or increasing the potential of structural failure [7,8]. Therefore, the estimation of the service life of a structure requires information about Cl penetration depth, chloride concentration profile, and the rate of penetration [9].

Cl content and fluid penetration into a concrete can be investigated through a number of methods including AASHTO T259 (salt ponding test) [10], ASTM C 1556 (bulk diffusion test) [11], silver nitrate spray on the surface (colorimetric technique) [12,13], AASHTO T277 (rapid chloride permeability test) [14–18], AASHTO T260 (Potentiometric Titration or Ion-Selective Electrode) [19,20] electrical migration [21–23], resistivity [24,25], pressure-induced fluid penetration [26], sorptivity [27,28], solvent counter diffusion [29], and gas diffusion [30]. Many of these tests are accelerated or use indirect methods to observe ion penetration into the samples. Test methods that directly measure the external ion penetration such as the bulk diffusion test (ASTM C 1556) are more powerful because it makes direct measurements of the ions penetrating the concrete.

One challenge with ACMs is the lack of published information regarding their use and performance. Also, the use of many of the previous test methods is challenging to interpret because of differences in chemical composition and a lack of fundamental measurement data with which to

compare these accelerated or indirect measurements. For this reason, the present study uses a direct and non-destructive X-ray mapping method called transmission X-ray microscopy (TXM) to observe iodide penetration into ACMs paste samples cured for different durations. X-ray imaging is considered a non-destructive method because it does not destroy a sample and the same sample can be tested several times to monitor a change in the sample over time or the same sample can be used in another experiment. Iodide is used because of two reasons. First, iodide strongly absorbs x-ray waves due to its high electron density. Secondly, iodide has a similar atomic diameter as chloride (iodide radius is 206 pm versus a chloride radius of 167 pm). Since TXM is non-destructive then it allows repeat measurements to be made on the same samples and the method is reliable in the previous testing as it shows good agreement with micro x-ray fluorescence (μXRF) mapping [31].

The ACMs considered in this study are calcium aluminate cement (CAC3), calcium sulfoaluminate belite cement (CSA2), calcium sulfoaluminate belite cement with polymer additive (CSA2B), alkali-activated binder with a Class C fly ash (AA1). The difference between CSA2 and CSA2B is the existence of a polymer additive in CSA2B to reduce the porosity. All of these products are available commercially. The results are compared to OPC. Paste samples made with the considered binders were sealed cured for different periods up to one year and then subjected to a potassium iodide solution ponding test and the effective diffusion coefficients were determined and compared.

2.2.Experimental Methods

2.2.1. Materials

The calcium aluminate cement (CAC3), calcium sulfo-aluminate cement (CSA2), calcium sulfo-aluminate belite cement (CSA2B), alkali-activated binder with a Class C fly ash (AA1), and ordinary Portland cement (OPC) were considered in this study. These materials are commercially available in North America. The chemical compositions of these cementitious materials were

measured by using bulk XRF and are represented in Table 2-1. For the AA1 paste mixture, a commercial two-component activator was used to activate the solution and react with the fly ash to produce cementitious properties; water was used as a plasticizer according to the AA1 manufacturer's recommendation. For OPC, CSA2, and CSA2B a polycarboxylate based high-range water-reducing (HRWR) admixture was used as a plasticizer. The dosage level was chosen for each mixture to match the dosage needed to provide a consistent slump in concrete mixtures. These concrete mixtures are part of a larger study which are not shown here [33]. To postpone the setting time of CSA2, and CSA2B binders, a food-grade citric acid was used as a retarder. To improve the workability and to delay the setting time of CAC3, a plasticizer – set retarder (PSR) was used. The dosages of the recent set modifying admixtures were chosen based on isothermal calorimetry experiments so that rapid hydration began at 2 hours [32].

Table 2-1. Chemical composition of binders with bulk XRF (% weight) [32]

Binder type	OPC	CSA2, CSA2B	CAC3	AA1
SiO_2	17.39	14.24	5.50	38.24
Al_2O_3	4.87	14.84	45.16	17.87
Fe_2O_3	4.71	1.12	6.90	5.88
CaO	65.15	49.23	37.68	24.75
MgO	1.40	1.55	0.22	6.24
SO_3	2.51	13.55	0.07	1.56
K_2O	0.48	0.67	0.26	0.34
Na_2O	0.46	0.21	0	1.85
P_2O_5	0.13	0.11	0.09	-
TiO_2	0.39	0.70	2.11	-
Mn_2O_3	0.11	0.02	0.02	-
SrO	0.15	0.20	0.04	-
ZnO	0.03	0.01	0	-
Cr_2O_3	0.09	0.05	0.089	-
LOI	2.12	3.51	1.86	0.20

2.2.2. Sample preparation

For all the considered ACMs except AA1, the water-to-binder ratio (w/b) was kept constant at 0.40. For AA1, water was used as the plasticizer; for this reason, w/b was chosen 0.21. This was chosen because it provided a comparable slump in concrete mixtures. In the AA1 mixture, cement replaced with the Class C fly ash and the two-component activator was added to the water. The mixture proportions were shown in Table 2-2. These materials were mixed based on ASTM C 305 procedures [34].

Table 2-2. Mixtures proportions

Binder type	Binder (g)	Water (g)	HRWR (mL)	PSR (mL)	Citric acid (g)	Activator (g)
OPC	891	354	1	-	-	-
CSA2	875	350	0.7	-	4	-
CSA2B	875	350	0.5	-	4	-
CAC3	886	353	-	0.4	-	-
AA1	1381	284	-	-	-	55.9

Four miniature plastic cylindrical vials with inner dimensions of 9.5×46 mm were used as a mold for each mixture. The vials were filled within 5 mm of the top as shown in Figure 2-1(a). Air voids within the sample were removed by manually rodding with a 1.45 mm in diameter wire. After casting, the samples were packed tightly to keep them upright and sealed. These sealed samples were stored in a temperature-controlled room at 23°C. Sealed curing was done to use a consistent method of treating all of the samples. After the curing was terminated, the samples were demolded, and a hydrophobic wax was applied to all sides of the sample except the finished surface. The wax was applied to ensure that there is only penetration from the finished surface. Next, a hexagonal polyvinyl chloride (PVC) nut was attached to the bottom of the samples as shown in Figure 2-1(b). The attached nut helped to load each sample with the same orientation, degree, and direction in the x-ray machine to scan consistently at each interval. Since the goal was to compare the radiographs

taken at the considered intervals with the reference radiograph, consistent imaging was a necessity for good image alignment. To start the ion diffusion test, prepared samples with the attached nut were transferred into the vials.

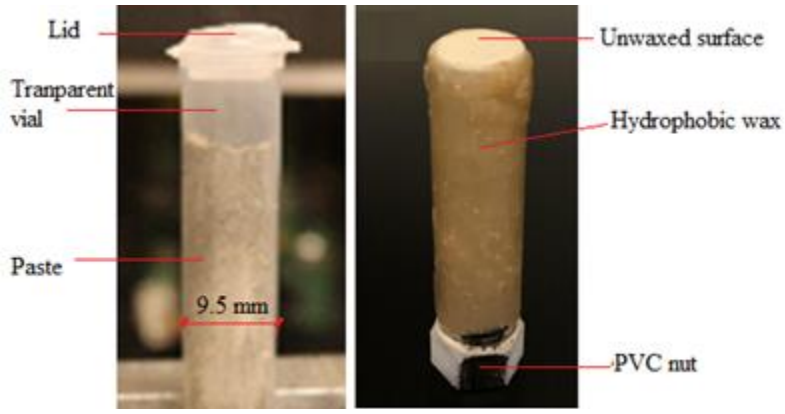

Figure 2-1. Sample figuration a) casted sample b) demolded and waxed sample

All ACM performance was compared with paste samples. Four paste samples were tested for each considered binder type at each curing time. Samples were cast and then were sealed for 35, 56, 90, 180, and 365 d while being stored at 23℃. Because of the conversion of CAC binders [35], curing times of 45, 70, 120, and 250 d were also investigated to provide more insight.

2.2.3. TXM Measurements

TXM is a direct observational technique of studying mass transport within cementitious materials. It has been shown that the average sample to sample variation of the calculated diffusion coefficients with TXM for the paste samples is $\pm 0.16\times10^{-11}$ m^2/s and the coefficient of variance (CV) of 9.88% which shows good repeatability of the method [31]. Moreover, it has been shown that there is an acceptable agreement between the iodide diffusion coefficient and chloride diffusion coefficient; in the previous study, it is shown that iodide gives diffusion coefficients 24% higher than chloride [31].

The benefits of TXM are: <1 min per scan, minimal sample preparation required, sample consistency can be obtained from 2D radiographs, and the resolution of the method is 8.8 μm which is sufficient for these measurements. The challenges with TXM are: it only detects the movement of iodide, it is sensitive to sample rotation and sample position at different imaging intervals, the obtained data at each pixel is an average over the depth of the sample, it needs unique calibration curves for different cementitious materials, and the energy used must be adjusted to the sample size.

The samples were scanned with TXM to get the initial image or radiograph before ponding with a 0.6 mol/L potassium iodide (KI) solution for 28 d. Since TXM can capture materials with high electron density, KI was chosen to be used as the penetrating tracer. Iodide in the KI strongly absorbs x-ray waves due to its high electron density.

After taking the reference radiograph, the same samples were scanned at intervals of 5 minutes, 1, 3, 7, 10, 14, 21, and 28 d after ponding and then returned to their solution after each scan. Since the iodide solution acts as a tracer it could be observed with the X-rays as it penetrates the sample. The captured images at the considered intervals were compared with the reference radiograph to observe the concentration changes, the penetration depth of the applied solution, surface concentration, and diffusion coefficient. More details are provided in appendix A and other publications [31]. For all of the concentration profiles shown in this study, a threshold level of 0.05 % of the concrete weight (0.21% by the weight of paste) was assumed as the threshold level for corrosion [36]. The threshold value is defined as the minimum concentration of chloride at the depth of the reinforcement that can initiate corrosion of the steel [37]. For chloride-induced corrosion, it is desirable to have a reliable chloride threshold value to predict when corrosion can initiate on metals embedded in a particular cementitious material [38]. Despite extensive research on threshold level value, no agreement among the values obtained is found. However, threshold chloride concentration values vary but are typically in the range of 0.05 to 0.1% by weight of concrete (0.4 to 0.8% by weight of

cement) [39]. Comparing the concentration profiles intersection with the threshold level line and the location of the embedded steel bars gives a better insight to the modelers and designers for evaluating the service life of a reinforced structure.

2.2.4. Porosity measurement

The porosity of each sample was determined by following the procedures of ASTM C642 [40] with some minor changes. For each binder, three samples were used to measure the porosity. Samples were submerged in water in a vacuum chamber to reach a constant value (equilibrium condition with mass change less than 0.03%). This saturated surface dried (SSD) weight was recorded as (W_{sa}). Next, the suspended apparent mass of the saturated samples was measured and recorded as (W_{su}). Next, the samples were dried in an oven at 110 ºC until an equilibrium mass was achieved (W_d). Eq. (2-1) was used to calculate the porosity of each sample.

$$Porosity = \frac{W_{sa} - W_d}{W_{sa} - W_{su}} \times 100 \qquad \text{Eq. (2-1)}$$

2.3. Results and discussions

2.3.1. Ordinary Portland cement (OPC)

Figure 2-2 shows a typical data set for different ages of curing for OPC. This is included to give the reader an overview of the raw data that is measured after 28 days of ponding. The threshold level is also shown as a dashed horizontal line. A visual inspection of the profiles slopes shows that by increasing curing time, penetration depth decreases. The sample with 35 d of curing shows a flatter slope compared to the other profiles, meaning a higher rate of penetration. There seems to be a minimal difference between the concentration profiles between 56 and 180 d. The sample that was cured for 365 d does show a decrease in slope and a lower amount of iodide penetration. This suggests that there is some improvement to the microstructure over extended periods in the OPC

samples. This may be caused by the hydration of belite [41]. Typical curves for the other binders can be found in the appendix.

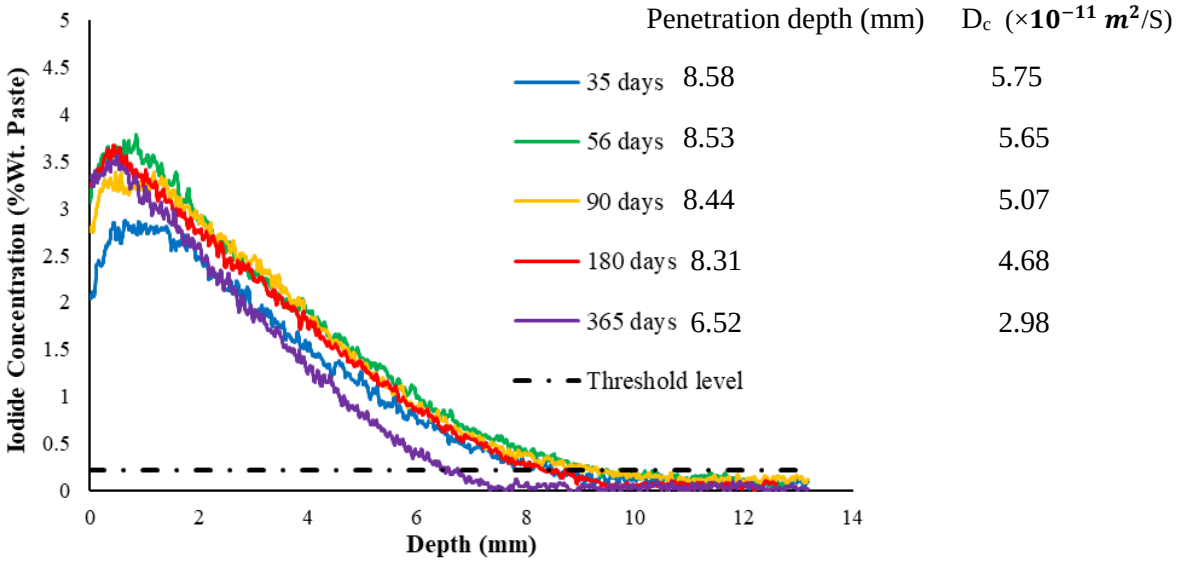

Figure 2-2. Iodide concentration profiles of OPC binder after different curing times

To more quantitatively compare the impact of curing time on mass transport, the diffusion coefficient (D_c), porosity, surface concentration (C_s), and penetration depth of each curing time are compared in Figure 2-3, 2-4, and 2-5 and a detailed discussion of the performance of each binder is included in subsequent sections. The results show that increasing the curing time to one year for OPC helps to improve the diffusion rate by 50% and reduce the porosity and penetration depth by 7% and 25%, respectively. Moreover, results in Figure 2-4 show that extending the curing time improved the binding capability of moving ions near the surface.

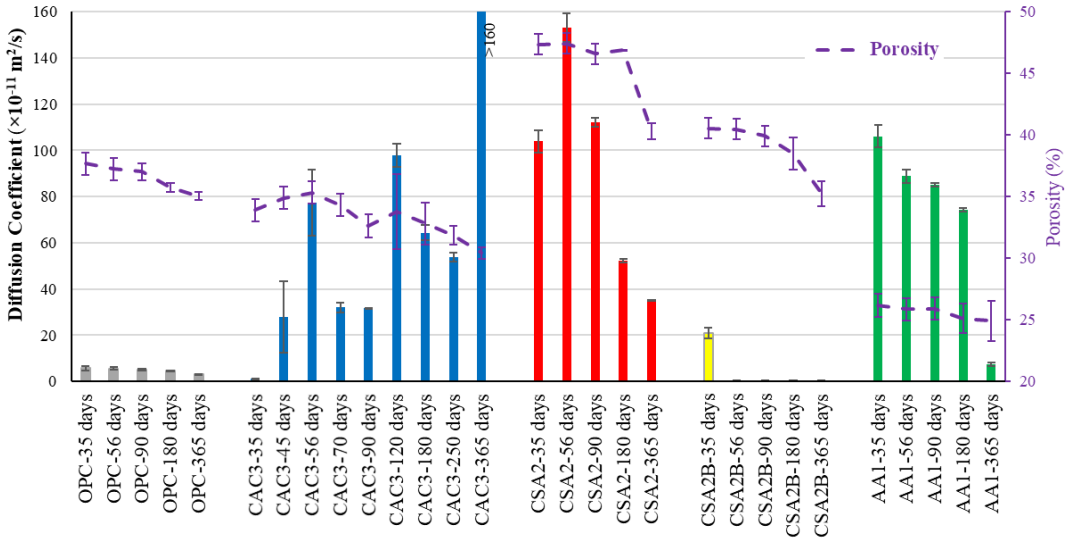

Figure 2-3. Diffusion coefficients along with the porosity

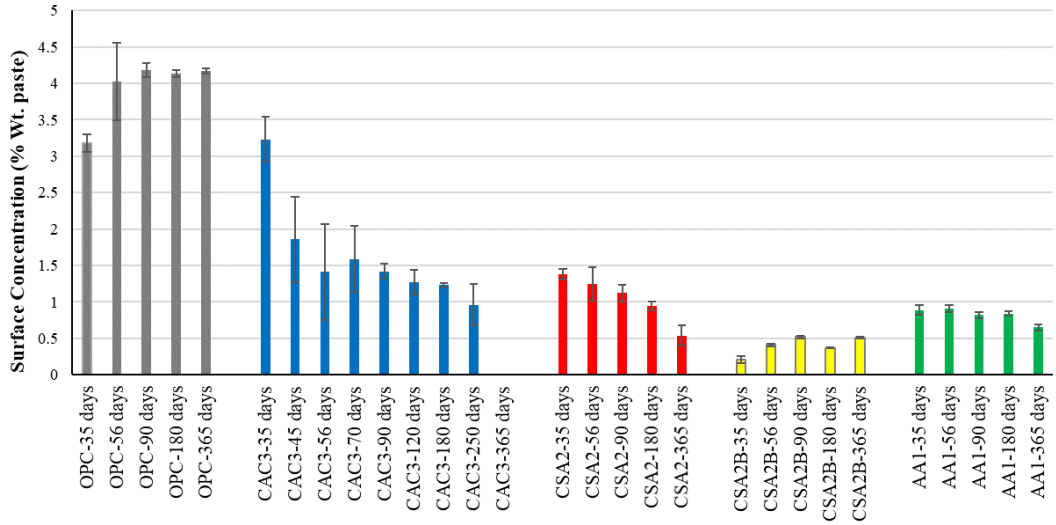

Figure 2-4. Surface concentrations

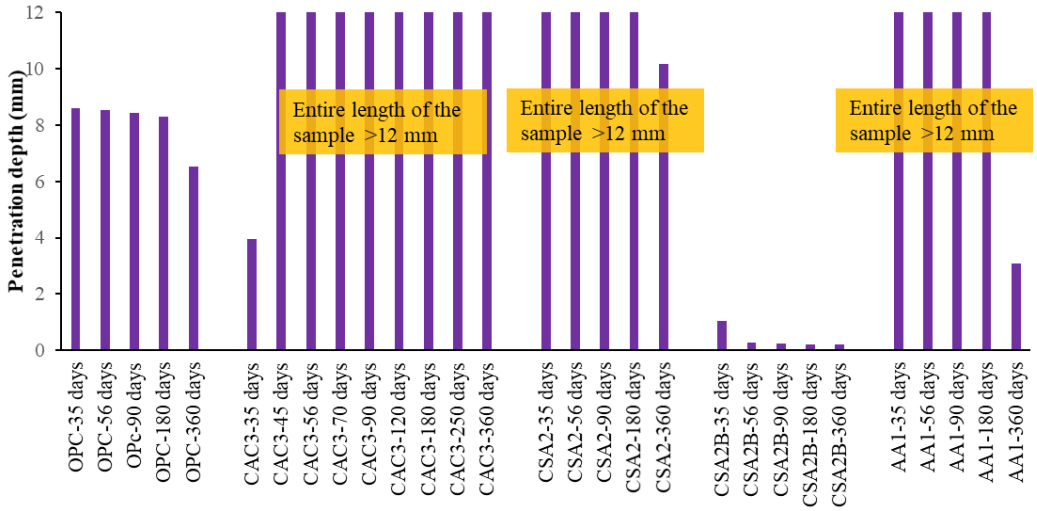

Figure 2-5. Tracer penetration depth

2.3.2. Calcium aluminate cement (CAC3)

For CAC3 more curing times were considered to study the impact of conversion. Conversion is known to cause changes in the microstructure that would cause a loss in strength and possible impacts on the D_c [42,43]. Figure 2-3 shows that 35 d of curing is the lowest D_c and the D_c at 45 d has a 27x increase of D_c. The depth of penetration is also >12 mm for all the samples after 35 d. This sudden increase in both D_c and the penetration depth is likely caused by cracking. This cracking may be random in the samples and depend on the propagation of these cracks that may have different impacts on the D_c of the samples. This may explain why there is no apparent trend to the D_c overtime for the samples from 45 d to 180 d besides all of them are significantly increased over the measurement at 35 d. However, it should be noted that the D_c at 365 d of curing cannot be determined. This suggests that the cracks have coalesced and are allowing the iodide to directly penetrate the sample.

Figure 2-4 shows that CAC3 samples with short curing times have higher surface concentration compared to the CAC3 samples with longer curing times. The surface concentration is typically an indication of the amount of binding. This higher amount of binding may be explained by the high amount of Al_2O_3 in this cement. Aluminum hydration products have been shown to bind ions and

form more stable products such as Friedel's salt [42]. This seems to be happening at early ages in CAC3. However, after 35 d the surface concentration decreases. This could be caused by conversion and consequently formation of hydration products with a decreased binding capacity. This is an area of future study.

Previous studies of CAC show that the early hydration products are not stable and will change over time. As this conversion occurs the later age hydration products cause a reduction in solid volume which damages the microstructure and releases water [43,44]. As shown in Figure 2-3, the porosity continues to decrease with time, but D_c continues to increase. This may occur because the cracks may change the overall volume of the sample but not the size or number of the pores. The continued hydration does seem to refine the pore system between the cracks. Microscopy studies of the samples at different periods may provide more insight into the changes.

Another study has shown that reinforced calcium aluminate cement concrete, with the pH of the pore solution between 11.4 and 12.5, maybe more susceptible to corrosion compared with OPC concrete [45]. However, assessment of the long-term durability of CAC3 by literature review alone is questionable and needs further work. This study just examined the resistance of CAC3 against fluid transport. Long-term resistance to other durability issues like sulfate attack, aggregate reactions, freeze-thaw action is essential to be studied.

2.3.3. Calcium sulfoaluminate cement (CSA2)

According to Figure 2-3 and Figure 2-5, CSA2 shows higher D_c values at all ages compared to OPC and also a higher ion penetration depth. One possible reason is the high pore interconnectivity due to the non-uniform formation of ettringite crystals (AFt) [46]. However, extending the curing time helps to reduce the D_c. For example, by increasing the curing time from 35 d to 180 d and 365 d, the D_c reduces by 50% and 66%, respectively. D_c improvement resulted in penetration depth reduction from the whole sample length (>12 mm) to 10.15 mm after 365 d of curing. This could

happen because belite phase reacts and produces more hydration products or monosulfate (AFm). Monosulfate formation has been suggested to take days or even months and the AFm phase has a higher binding capacity than AFt [47,48]. However, the surface concentration measurements in Figure 2-4 decreased as the hydration time increased. Since the surface concentration decreases over time it is not likely that the AFm phases are forming and the refinement in the microstructure is probably from the hydration of the belite.

2.3.4. Calcium sulfoaluminate cement with polymer additives (CSA2B)

Results in Figure 2-3 and Figure 2-5 show that the D_c and depth of penetration did not significantly decrease after 35 d and were the lowest of any material investigated. One should use the reported D_c values with care as the concentration profiles are very low in the samples and so the diffusion coefficients calculated may not be comparable to the other measurements. The surface concentration was very consistent for the times investigated. Penetration depth for CSA2B was considerably lower than other tested binders. This testing shows that the additive contained in CSA2B was able to decrease the porosity enough to make a significant change in the measured D_c value. This shows that CSA cement with the right additives can significantly decrease the ion penetration into the concrete.

2.3.5. Alkali-Activated Binder (AA1)

Figure 2-3 and Figure 2-5 show that extending the curing time for AA1 helps to decrease the D_c and penetration depth over time. There is a significant decrease in the D_c between 180 d and 365 d. After 365 d of hydration the penetration depth of the samples to those comparable to OPC. While the D_c and the depth of penetration improved over time the porosity of the AA1 samples did not. This shows that porosity is not always a reliable criterion for evaluating the permeability of a binder. The surface concentration for AA1 as shown in Figure 2-4 was very consistent at the times investigated compared to other investigated binders.

The extended curing time may either increase the degree of crystallinity of calcium silicate hydrate (C–S–H) or increase the formation of the tobermorite-type calcium silicate hydrate phase ($Ca_5Si_6O_{16}(OH)_2$) [49]. The reader must remember that the type of fly ash, the activity and chemical consistency of the activator, and the temperature has important impacts on the hydration mechanism of this type of ACMs and consequently affect its binding capacity [49,50]. This means that changes in materials may produce different results but these findings are still useful to evaluate a commercially available alkali-activated binder.

2.3.6. Comparing all binders

This paper tried to increase understanding of how to best utilize ACMs in new infrastructure. Overall, both the variation in ACM composition and the lack of published information regarding their use and performance has inhibited their widespread adoption and use. To begin to address the issues preventing a larger-scale usage of ACMs, this paper compares the mass transport properties of several commercially produced ACMs by applying a direct observational test method. This comparison will use the 365 d cured samples because they are most likely representative of the long-term performance of the different binders. The results of D_c in Figure 2-3 show that the highest D_c is for CAC3 at 365 d followed by CSA2, AA1, OPC, and finally, CSA2B has the lowest D_c. The outstanding performance of CSA2B shows that adding the polymer to CSA2 can improve the performance of the mixture under outside chemical penetration. Other researchers recommend blending ACMs with high D_c with OPC or other cementitious materials or using other additives to improve ACMs performance [35,50–59]. Porosity measurement shows that CSA2 has the highest porosity followed by OPC, CSA2B, CAC3, and AA1. OPC ranked first among all studied binders for surface concentration value while CAC3 ranked second followed by AA1, CSA2, and CSA2B. The lowest penetration depth is recorded for CSA2B which is the binder with the lowest D_c value. AA1 is the second binder with the lowest penetration depth while it has not the second-lowest D_c. OPC showed a moderate penetration depth while CSA2 and CAC3 showed higher penetration. The

recent rankings show that having one mass transport property is not enough to decide or evaluate the performance of different binders. Having higher D_c value for most of the ACMs compared to OPC does not mean that they are not suitable for using in infrastructures. A reader must remember that each binder has its unique properties that can be used in different structures with unique technical requirements. On the other hand, the results of this study represent a comparison of mass transport properties not resistance to degradation from carbonation, freezing, and thawing, alkali-silica reaction, sulfate attack, or heat performance. Some application of different ACMs can be accounted but not limited to the recommendations listed below:

- CAC3 with higher early strength, chemical resistance, and higher temperature resistance compared to OPC can be used in sewage networks, where sulfuric acid generation by bacteria is a problem, in hydraulic dams, where resistance to abrasion is critical, in heat-resisting and refractory concrete, fire training facilities, heat resistant coating for concrete in tunnels during a fire, or other applications that excellent performance at temperatures above 1700 °C is required [60–65].

- Contrary to OPC, Ettringite is the main hydration phase of CSA2 and CSA2B binders. Because of this, both CSA2 and CSA2B cement can achieve acceptable setting times and good strength development in a shorter time frame than OPC systems. CSA2 and CSA2B binders are often used in self-leveling screeds, as well as in repairs due to the expansive ability of certain formulations of the material. The pH of the pore solution in CSA2 and CSA2B lies between 10 and 11.5 due to the different hydration chemistry. This low alkalinity provides an advantage for making glass-fiber reinforced concrete (GRC) products [66,67]. Unique properties of CSA2 and CSA2B make them as potential candidates for the immobilization of wastes that contain reactive metals [67].

- AA1 binders with low production cost, energy efficiency, and environmentally friendly characteristics in comparison to OPC have a major role in the waste disposal and are popular for systems requiring high heat resistance such as naval runways, high resistance to freezing and thawing, alkali-aggregate reaction, and high acid resistance [50,66,68]. Also, AA1 will have uses in fixation of hazardous wastes such as radioactive wastes, and applications where the rapid setting is desired [69].

2.3.7. Comparing porosity and diffusion coefficient

The porosity and D_c are both included in Figure 2-3 so that they can be easily compared. The results show that porosity is not a reliable method to predict the D_c for the binders investigated. For instance, AA1 has the lowest porosity at all studied ages but its D_c values are not the lowest. Another example of this is that CSA2B has the lowest D_c values while the porosity values are higher than many of the other types of cement investigated. Besides, the porosity measurements did not indicate the same binder. For instance, the porosity of CAC3 and AA1 changed by 10.2% and 4.8%, respectively after 365 d while the D_c values for these two binders changed >12480% and 93%, respectively. These differences could be caused by differences in the degree of saturation (DoS), cracking, interconnectivity, and pore arrangement are important parameters that impact the ion penetration of the samples and these are not accurately measured by the porosity.

2.4. Practical Implications

One of the primary concerns with using ACMs is their long-term durability performance. This work shows that several commercial ACMs have the potential to show performance that is much better than OPC and some that are worse. Further, these experiments are carried out on samples from 35 d to 365 d in age. This focus on long term performance is important because it shows the potential for these materials to continue to change the D_c over time. While many of these materials showed an improvement, the CAC samples did not. This means that testing results before 45 d may not be

representative of the long-term performance of these materials. If durability is a concern for CAC materials, then it is recommended that testing of these materials only be done after conversion has occurred. For this testing, it was at least 45 d but the properties at 365 d were significantly worse.

This work also shows that CSA2B has outstanding potential to reduce the penetration of ions into concrete and that they may be a useful tool for samples in extreme exposure conditions. It should be noted that this paper focused solely on the outside penetration of ions and not on subsequent reactions like corrosion or salt attack that may come afterward. These deterioration processes would have to be studied with these ACMs in relevant conditions to determine how the pore solution and chemical consistency of the matrix change these values. However, it should be noted that the first step in most deterioration mechanisms is the penetration of outside chemicals. This work shows that the choice of ACM has important ramifications on this performance.

Furthermore, this study shows that porosity is not a useful parameter by itself to predict ion penetration into these materials. The D_c obtained from TXM is a direct method of measuring mass transport and so it provides more realistic insights into fluid transport.

It is not clear if the performance of the paste in this study is representative of the field performance of the concrete for these materials, but the paste is the primary mode of transport within a concrete sample. It is also not clear if the curing in the field will be representative of what is observed in this work. These are areas for future study.

2.5.Conclusions

This work investigates the impact of time on the porosity and ion penetration of OPC and several alternative cementitious materials (ACMs) for paste samples with a w/cm of 0.40. The considered ACMs in this study are calcium aluminate cement (CAC3), calcium sulfoaluminate cement (CSA2), calcium sulfoaluminate cement with a pore reducing additive (CSA2B), and alkali-

activated binder with a Class C fly ash (AA1). Samples were prepared with the mentioned binders and sealed cured for 35 d to 365 d.

After curing the samples, each sample was scanned at different intervals by the non-destructive transmission X-ray microscopy (TXM) method with applying 0.6 Mol/L potassium iodide (KI) solution. The following findings were made:

1- The diffusion coefficient (D_c) for OPC was consistent between 35 d to 180 d and then there was a 48% improvement in performance from 180 d to 365 d.

2- The D_c for CAC3 increased over time because of cracking caused by the conversion. After 365 d the pore structure seems to be interconnected and this allows the iodide to freely penetrate into the sample.

3- For CSA2, there was not much change in the D_c between 35 d and 90 d; however, after 180 d and 356 d, the D_c decreased by 50% and 66%, respectively.

4- The D_c and ion penetration for CSA2B was the lowest of all the samples investigated. After 35 d of hydration, there was minimal penetration of the iodide into the sample.

5- For AA1, the most effective curing time between those investigated is 365 d with a 93% improvement in D_c compared to the values measured at 35 d. The reduction in the D_c also reduced the depth of penetration of the iodide into the sample to values that are comparable to OPC.

6- Porosity is not a useful parameter for evaluating the D_c or depth of penetration for the binders investigated. The direct measurement of the D_c obtained from the TXM test method provides a more realistic insight into the fluid transport into the concrete.

While many possible mechanisms have been suggested in this work to cause this change in ion penetration, the findings should be verified with additional microanalysis studies focused on the changes in the structure and chemical composition of the binders. However, this work is important because it provides useful observations of the bulk properties of these materials also the timing over which they change.

Acknowledgment

The authors acknowledge the financial support from the Federal Highway Association (FHWA) Exploratory Advanced Research (EAR) Program (Project No. CMMI 1030972), and the United States National Science Foundation CMMI 1635878. The authors would like to thank Ms. Megan Buchanan and Ms. Alyssa Rogers for their assistance with casting the samples. The authors would like to thank Dr. Dan Cook and Mr.Ali Hendi for giving valuable feedback and comments.

References

[1] E. Worrell, L. Price, N. Martin, C. Hendriks, L.O. Meida, Carbon dioxide emissions from the global cement industry, Annual Review of Energy and the Environment. 26 (2001) 303–329.

[2] I. Ismail, S.A. Bernal, J.L. Provis, R. San Nicolas, D.G. Brice, A.R. Kilcullen, S. Hamdan, J.S.J. van Deventer, Influence of fly ash on the water and chloride permeability of alkali-activated slag mortars and concretes, Construction and Building Materials. 48 (2013) 1187–1201.

[3] K.Y. Ann, J.H. Ahn, J.S. Ryou, The importance of chloride content at the concrete surface in assessing the time to corrosion of steel in concrete structures, Construction and Building Materials. 23 (2009) 239–245.

[4] P.D. Cady, R.E. Weyers, Chloride penetration and the deterioration of concrete bridge decks, Cement, Concrete and Aggregates. 5 (1983) 81–87.

[5] A. Costa, J. Appleton, Chloride penetration into concrete in marine environment—Part I: Main parameters affecting chloride penetration, Materials and Structures. 32 (1999) 252.

[6] F. Debieb, L. Courard, S. Kenai, R. Degeimbre, Mechanical and durability properties of concrete using contaminated recycled aggregates, Cement and Concrete Composites. 32 (2010) 421–426.

[7] A. Neville, Chloride attack of reinforced concrete: an overview, Materials and Structures. 28 (1995) 63.

[8] A. Ababneh, F. Benboudjema, Y. Xi, Chloride penetration in nonsaturated concrete, Journal of Materials in Civil Engineering. 15 (2003) 183–191.

[9] E. Proverbio, F. Carassiti, Evaluation of chloride content in concrete by X-ray fluorescence, Cement and Concrete Research. 27 (1997) 1213–1223.

[10] AASHTO T 259, Resistance of Concrete to Chloride Ion Penetration, (1980).

[11] ASTM C1556, Standard Test Method for Determining the Apparent Chloride Diffusion Coefficient of Cementitious Mixtures by Bulk Diffusion, (2016).

[12] E. Meck, V. Sirivivatnanon, Field indicator of chloride penetration depth, Cement and Concrete Research. 33 (2003) 1113–1117.

[13] V. Baroghel-Bouny, P. Belin, M. Maultzsch, D. Henry, AgNO3 spray tests: advantages, weaknesses, and various applications to quantify chloride ingress into concrete. Part 2: Non-steady-state migration tests and chloride diffusion coefficients, Materials and Structures. 40 (2007) 783.

[14] AASHTOT277-93, Electrical Indication of Concrete's Ability to Resist Chloride, (1983).

[15] ASTM C1202-19, Standard Test Method for Electrical Indication of Chloride's Ability to Resist Chloride, (2019).

[16] T. Zhang, O.E. Gjørv, An electrochemical method for accelerated testing of chloride diffusivity in concrete, Cement and Concrete Research. 24 (1994) 1534–1548.

[17] R.K. Dhir, M.R. Jones, H.E.H. Ahmed, A.M.G. Seneviratne, Rapid estimation of chloride diffusion coefficient in concrete, Magazine of Concrete Research. 42 (1990) 177–185.

[18] P.E. Streicher, M.G. Alexander, A chloride conduction test for concrete, Cement and Concrete Research. 25 (1995) 1284–1294.

[19] AASHTO T260-94, Standard Method for Sampling and Testing for Chloride Ion in Concrete and Concrete Raw Materials, (1994).

[20] M.A. Climent, G. de Vera, J.F. López, E. Viqueira, C. Andrade, A test method for measuring chloride diffusion coefficients through nonsaturated concrete: Part I. The instantaneous plane source diffusion case, Cement and Concrete Research. 32 (2002) 1113–1123.

[21] A. Delagrave, J. Marchand, E. Samson, Prediction of diffusion coefficients in cement-based materials on the basis of migration experiments, Cement and Concrete Research. 26 (1996) 1831–1842.

[22] C. Ozyildirim, Rapid Chloride permeability testing of sílica-fume concrete, Cement, Concrete and Aggregates. 16 (1994) 53–56.

[23] A.A. Kyi, B. Batchelor, An electrical conductivity method for measuring the effects of additives on effective diffusivities in portland cement pastes, Cement and Concrete Research. 24 (1994) 752–764.

[24] C. Andrade, C. Alonso, S. Goni, Possibilities for electrical resistivity to universally characterise mass transport processes in concrete, Proceedings of the Concrete 2000 Conference. 2 (1993) 1639–1652.

[25] C. Andrade, Calculation of chloride diffusion coefficients in concrete from ionic migration measurements, Cement and Concrete Research. 23 (1993) 724–742.

[26] P. Halamickova, R.J. Detwiler, D.P. Bentz, E.J. Garboczi, Water permeability and chloride ion diffusion in Portland cement mortars: relationship to sand content and critical pore diameter, Cement and Concrete Research. 25 (1995) 790–802.

[27] C. Hall, Water sorptivity of mortars and concretes: a review, Magazine of Concrete Research. 41 (1989) 51–61.

[28] N.S. Martys, C.F. Ferraris, Capillary transport in mortars and concrete, Cement and Concrete Research. 27 (1997) 747–760.

[29] R.F. Feldman, Diffusion measurements in cement paste by water replacement using propan-2-ol, Cement and Concrete Research. 17 (1987) 602–612.

[30] A. Sharif, K.F. Loughlin, A.K. Azad, C.M. Navaz, Determination of the effective chloride diffusion coefficient in concrete via a gas diffusion technique, Materials Journal. 94 (1997) 227–233.

[31] M. Khanzadeh Moradllo, Q. Hu, M.T. Ley, Using X-ray imaging to investigate in-situ ion diffusion in cementitious materials, Construction and Building Materials. 136 (2017) 88–98.

[32] M. Khanzadeh Moradllo, M.T. Ley, Comparing ion diffusion in alternative cementitious materials in real time by using non-destructive X-ray imaging, Cement and Concrete Composites. 82 (2017) 67–79.

[33] P.A. Lisa E. Burris Kimberly E. Kurtis, Amir Hajibabaee, M. Tyler Ley, Understanding Shrinkage in Alternative Binder Systems, ACI Symposium Publication. 336 (2019) 73–90.

[34] ASTM C305, Standard Practice for Mechanical Mixing of Hydraulic Cement Pastes and Mortars of Plastic Consistency, (2006).

[35] C. Gosselin, Microstructural development of calcium aluminate cement based systems with and without supplementary cementitious materials, (2009).

[36] M.D.A. Thomas, P.B. Bamforth, Modelling chloride diffusion in concrete: Effect of fly ash and slag, Cement and Concrete Research. 29 (1999) 487–495.

[37] S. Poulsen, H.E. Sørensen, Chloride Threshold Values-State of the art, Danish Expert Centre for Infrastructure Constructions. 1 (2012).

[38] S.K. Lee, Literature Review of Chloride Threshold Values for Grouted Post-Tensioned Tendons, Federal Highway Administration, FHWA-HRT-12-067, McLean. (2012).

[39] K.R. Larsen, Study Evaluates Chloride Limits for Structural Reinforced Concrete, (2017).

[40] ASTM C642, Standard Test Method for Density, Absorption, and Voids in Hardened Concrete, (2013).

[41] N. Banthia, S. Mindess, Water permeability of cement paste, Cement and Concrete Research. 19 (1989) 727–736.

[42] J. Newman, B.S. Choo, Advanced concrete technology set, (2003).

[43] S. Lamberet, Durability of ternary binders based on Portland cement, calcium aluminate cement and calcium sulfate, (2004).

[44] H.J. Yang, S.H. Jin, K.Y. Ann, Chloride Transport of High Alumina Cement Mortar Exposed to a Saline Solution, Advances in Materials Science and Engineering. (2016).

[45] R.J. Currie, N.J. Crammond, BRE, Assessment Of Existing High Alumina Cement Construction In The Uk, Proceedings of the Institution of Civil Engineers-Structures and Buildings. 104 (1994) 83–92.

[46] J. Zhao, G. Cai, D. Gao, S. Zhao, Influences of freeze-thaw cycle and curing time on chloride ion penetration resistance of Sulphoaluminate cement concrete, Construction and Building Materials. 53 (2014) 305–311.

[47] H.F.W. Taylor, Cement chemistry, 475 (1990).

[48] H. Hirao, K. Yamada, H. Takahashi, H. Zibara, Chloride Binding of Cement Estimated by Binding Isotherms of Hydrates, Journal of Advanced Concrete Technology. 3 (2005) 77–84.

[49] O. Burciaga-Díaz, J.I. Escalante-García, Structure, mechanisms of reaction, and strength of an alkali-activated blast-furnace slag, Journal of the American Ceramic Society. 96 (2013) 3939–3948.

[50] D.M. Roy, W. Jiang, M.R. Silsbee, Chloride diffusion in ordinary, blended, and alkali-activated cement pastes and its relation to other properties, Cement and Concrete Research. 30 (2000) 1879–1884.

[51] I. Janotka, A. Ray, S.C. Mojumdar, The hydration phase and pore structure formation in the blends of sulfoaluminate-belite cement with Portland cement, Cement and Concrete Research. 33 (2003) 489–497.

[52] M. García-Maté, A.G. De la Torre, L. León-Reina, M.A.G. Aranda, I. Santacruz, Hydration studies of calcium sulfoaluminate cements blended with fly ash, Cement and Concrete Research. 54 (2013) 12–20.

[53] J. Péra, J. Ambroise, New applications of calcium sulfoaluminate cement, Cement and Concrete Research. 34 (2004) 671–676.

[54] S.A. Rodger, D.D. Double, The chemistry of hydration of high alumina cement in the presence of accelerating and retarding admixtures, Cement and Concrete Research. 14 (1984) 73–82.

[55] T. Matusinović, D. Čurlin, Lithium salts as set accelerators for high alumina cement, Cement and Concrete Research. 23 (1993) 885–895.

[56] T. Matusinović, N. Vrbos, Alkali metal salts as set accelerators for high alumina cement, Cement and Concrete Research. 23 (1993) 177–186.

[57] F. Goetz-Neunhoeffer, Hydration kinetics of calcium aluminate cement in the presence of Li2CO3, Proceedings of the Centenary Conference, Avignon. 30 (2008).

[58] L. Pelletier-Chaignat, F. Winnefeld, B. Lothenbach, C.J. Müller, Beneficial use of limestone filler with calcium sulphoaluminate cement, Construction and Building Materials. 26 (2012) 619–627.

[59] P. Chaunsali, P. Mondal, Influence of calcium sulfoaluminate (CSA) cement content on expansion and hydration behavior of various ordinary portland cement-CSA blends, Journal of the American Ceramic Society. 98 (2015) 2617–2624.

[60] J. Ding, Y. Fu, J.J. Beaudoin, Strätlingite formation in high alumina cement-silica fume systems: significance of sodium ions, Cement and Concrete Research. 25 (1995) 1311–1319.

[61] K.L. Scrivener, J.-L. Cabiron, R. Letourneux, High-performance concretes from calcium aluminate cements, Cement and Concrete Research. 29 (1999) 1215–1223.

[62] W.E. Lee, W. Vieira, S. Zhang, K.G. Ahari, H. Sarpoolaky, C. Parr, Castable refractory concretes, International Materials Reviews. 46 (2001) 145–167.

[63] R. Montgomery, Heat-resisting and refractory concretes, Advanced Concrete Technology. 3 (2003) 4.

[64] A.G. Holterhoff, Fire Training facilities: Materials and methods, Calcium Aluminate Cements, Edinburgh, (2001), pp. 577–583.

[65] E. Wagner, H. HÖNL, Heat resistant coating for concrete in tunnels during fire, Calcium Aluminate Cements, Edinburgh, (2001), pp. 585–593.

[66] L.E. Burris, P. Alapati, R.D. Moser, M.T. Ley, N. Berke, K.E. Kurtis, Alternative cementitious materials: Challenges and opportunities, International Workshop on Durability and Sustainability of Concrete Structures, Bologna, Italy. (2015).

[67] Q. Zhou, N.B. Milestone, M. Hayes, An alternative to Portland cement for waste encapsulation—the calcium sulfoaluminate cement system, Journal of Hazardous Materials. 136 (2006) 120–129.

[68] D.M. Roy, Alkali-activated cements Opportunities and challenges, Cement and Concrete Research. 29 (1999) 249–254.

[69] A. Roy, P.J. Schilling, H.C. Eaton, Alkali activated class C fly ash cement, (1995).

[70] MATLAB (R2016a), version 9.0.0, (2016).

[71] V.C. Tidwell, L.C. Meigs, T. Christian-Frear, C.M. Boney, Effects of spatially heterogeneous porosity on matrix diffusion as investigated by X-ray absorption imaging, Journal of Contaminant Hydrology. 42 (2000) 285–302.

[72] L. Cavé, T. Al, Y. Xiang, P. Vilks, A technique for estimating one-dimensional diffusion coefficients in low-permeability sedimentary rock using X-ray radiography: Comparison with through-diffusion measurements, Journal of Contaminant Hydrology. 103 (2009) 1–12.

[73] Curve fitting toolbox : for use with MATLAB® : user's guide, (2001).

[74] J. Crank, The mathematics of diffusion, (1975).

[75] K.L. Scrivener, A. Capmas, 13-Calcium Aluminate Cements, Lea's Chemistry of Cement and Concrete (Fourth Edition). Butterworth-Heinemann, Oxford. (2003) 713–782.

APPENDICES

Appendix. A. TXM technique

In this study, a Skyscan 1172 μCT scanner with the settings summarized in Table 2-1.Ap was used to conduct the experiments. Scanning with TXM results in capturing grayscale images that each pixel has a gray value between 0 and 255. The gray value changes by density, thickness, chemistry, or a combination of them. In this method, materials with the higher density are darker (have low gray values) and materials with the low density are brighter (have high gray values). The concept behind this technique is that when a solution with high electron density penetrates a sample, the penetrated depths get lower gray values and consequently become darker because of the free, absorbed, and bound ions.

Since TXM can capture materials with high electron density, potassium iodide (KI) was chosen as the penetrating tracer. Iodide in KI has a similar atomic diameter size and chemical properties to chloride (Cl) but has a high electron density. Since the goal was to compare the time series radiographs with the reference radiograph, it was necessary to get identical radiographs at each interval of scanning. For taking consistent radiographs for each individual sample an appropriate stage was designed to be matched with the attached nut on the samples in order to fix the position of the samples in the X-ray scanner. This stage forced to load the sample in a constant manner and scan the same side of the samples at each considered interval. Keeping the direction constant becomes more important when composite materials like concrete samples are investigating. A small

rotation of the sample or minor differences in the angle of scanning in the reference radiograph compared to the other radiographs leads to imperfect image alignment.

Table 2-1.Ap. Settings used in TXM

Pixel size (μm)	Voltage (keV)	Current (μA)	Filter	Acquisition time	Chamber condition
8.8	100	100	0.5 mm Al +Cu	8 s	air

To analyze the taken radiographs, a software programming code [69] with minimal user intervention was prepared to align the images taken at other intervals with reference images. Alignment of the radiographs means applying local displacements (i.e. shifting and rotating) to the all taken radiographs of one individual sample in a way to establish a point-by-point correspondence between the reference and other radiographs. Then, to get the average of gray values at each depth for each sample, the central region of each radiograph with a width of 0.88 mm (approximately 100 columns of pixels) as shown in Figure 2-1.Ap was considered to eliminate cupping artifact[1].

Each line passed from a column of the pixels returns a gray value profile. The final gray value profile was an average of all 100 gray value profiles for each taken radiograph as shown in Figure 2-2.Ap (a). The legend expresses the ponding time for each profile. As ponding time increases and more solution penetrates in the samples, gray values at the corresponded depths decrease because of the free, absorbed, and bound ions. The averaged gray value profile for each radiograph was

[1] Cupping artifact refers to a locally bright appearance along the periphery of a sample. Because the tested samples were small cores with cylindrical shape, the center of the sample is denser than the regions near the sides. For this reason, the x-ray beam is "hardened" by passing through the center region of the sample and the mean photon energy will be higher around the center. Since higher energy photons are less attenuated by denser region, the beam will be less attenuated versus identical material near the sides.

subtracted from the averaged gray value profile of the reference radiograph correlated to a single sample in the logarithm scale to calculate attenuation (Δμ) according to Beer-Lambert Law in Eq.(2-2) [70,71]. Plotting the attenuation values versus depth gives attenuation profiles as shown in Figure 2-2.App (b).

$$(\Delta\mu)_x = \ln (I_{ref})_x - \ln (I_t)_x \qquad \text{Eq. (2-2)}$$

where $(I_{ref})_x$ is the transmitted X-ray intensity (gray value) at each depth (x) of the reference profile and $(I_t)_x$ is the transmitted X-ray intensity at the same depth in other radiographs taken at other intervals. To convert the calculated attenuations to concentration, calibration curves were applied. To develop the calibration curves, standard samples with different selected iodide concentrations added to the mixtures during mixing were used for each of the investigated binders. After scanning the standard samples, the attenuation related to each iodide concentration was extracted. The obtained correlated attenuations and concentrations were plotted in a scatter X-Y chart. Ultimately, a curve was fitted on the obtained spots to get an equation that converts the attenuation to the iodide concentration for each binder. The same sample sizes, mixtures, curing procedure, and scan setup explained in sections 2.2.2 and 2.2.3 were used to make and analyze the standard samples. The calibration curves used in this study are shown in Figure 2-3.Ap.

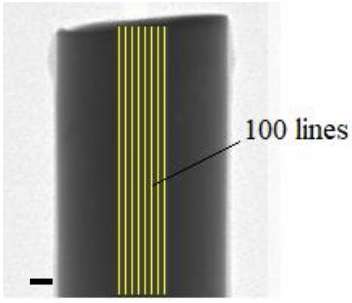

Figure 2-1.Ap. A radiograph and considered 100 lines in the middle part of the sample for data analyzing

Then each point on the attenuation profiles was put in the calibration equation to get the correlated iodide concentration. Finally, by plotting the concentration values versus depth, iodide

concentration profiles similarly shown in Figure 2-2 were obtained. Nonlinear regression using the Matlab curve fitting toolbox [72] was then conducted on iodide concentration profiles with Fick's second law as stated in Eq. (2-3) [73], to find the values of effective diffusion coefficient (D_c) and surface concentration (C_s). The last two parameters are important for service life models to predict the life span of each structure. The diffusion coefficient obtained from this test method combines the impact of fluid transport mechanisms of diffusion, absorption, convection, and chemical binding in one term. For this reason, the diffusion coefficient obtained from the observation of the applied technique in this study provides a more realistic insight into the fluid transport into the concrete.

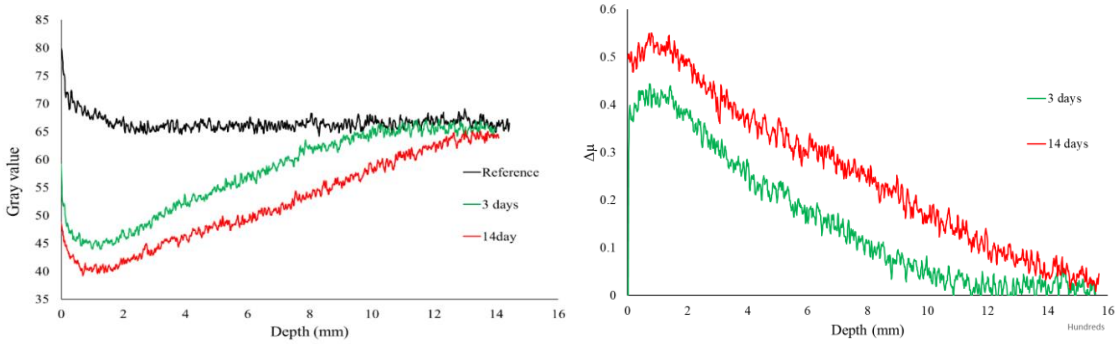

(a) (b)

Figure 2-2.Ap. a) an example of gray value profiles at different ponding days and b) correlated attenuation profiles

$$C_{(x,t)} = C_s\left(1 - \text{erf}\left(\frac{x}{2\sqrt{D_c t}}\right)\right) \qquad \text{Eq. (2-3)}$$

$$C_{(x,0)} = 0 \quad x > 0, \quad C_{(0,t)} = C_s \quad t \geq 0$$

Where x is the distance from sample surface; t denotes time; D_c is diffusion coefficient; C_s is surface iodide concentration; C(x,t) represents iodide concentration at the depth of x from the surface after time t; and erf is the error function.

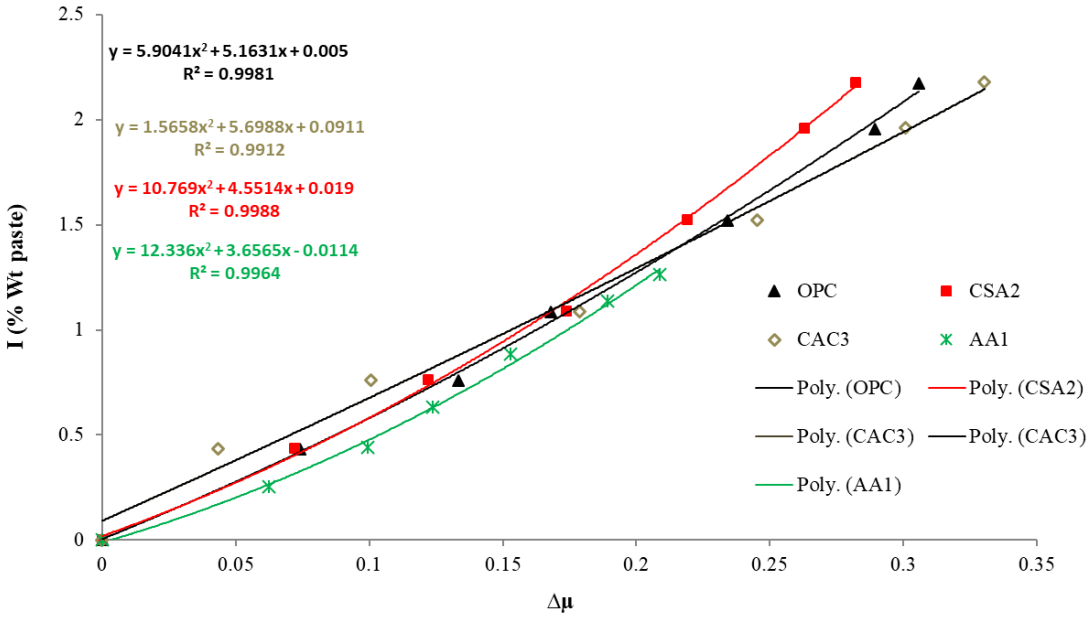

Figure 2-3.Ap. Calibration curves used to convert the attenuation to concentration

Appendix. B. Mass transport properties of all studied binders

Table 2-2.Ap. Mass transport properties of the considered binders

Curing time	Mass transport properties	OPC	AA1	CSA2	CSA2B	CAC3
35 d	C_s (%Wt.Paste)	3.18	0.89	1.38	0.21	3.23
	D_c ($\times 10^{-11}$ m^2/s)	5.75	106	103.90	20.90	1.28
	R^2	0.97	0.60	0.91	0.33	0.94
	Penetration depth (mm)	8.58	E*	E	1.05	3.94
45 d	C_s (%Wt.Paste)					1.86
	D_c ($\times 10^{-11}$ m^2/s)					27.76
	R^2					0.76
	Penetration depth (mm)					E
56 d	C_s (%Wt.Paste)	4.02	0.91	1.25	0.41	1.41
	D_c ($\times 10^{-11}$ m^2/s)	5.65	88.80	153.03	0.047	77.39
	R^2	0.99	0.40	0.81	0.36	0.75
	Penetration depth (mm)	8.53	E	E	0.26	E
70 d	C_s					1.59
	D_c ($\times 10^{-11}$ m^2/s)					31.99
	R^2					0.86
	Penetration depth (mm)					E
90 d	C_s (%Wt.Paste)	4.18	0.82	1.12	0.52	1.42
	D_c ($\times 10^{-11}$ m^2/s)	5.07	85.10	112.11	0.042	31.57
	R^2	0.99	0.65	0.61	0.62	0.58
	Penetration depth (mm)	8.44	E	E	0.25	E
120 d	C_s (%Wt.Paste)					1.27
	D_c ($\times 10^{-11}$ m^2/s)					97.91
	R^2					0.55
	Penetration depth (mm)					E
180 d	C_s (%Wt.Paste)	4.13	0.84	0.95	0.37	1.23
	D_c ($\times 10^{-11}$ m^2/s)	4.68	74.43	52.20	0.0326	64.37
	R^2	0.993	0.646	0.902	0.449	0.533
	Penetration depth (mm)	8.31	E	E	0.21	E
250 d	C_s (%Wt.Paste)					0.96
	D_c ($\times 10^{-11}$ m^2/s)					53.82
	R^2					0.566
	Penetration depth (mm)					E
365 d	C_s (%Wt.Paste)	4.17	0.65	0.54	0.51	N/A**
	D_c ($\times 10^{-11}$ m^2/s)	2.98	7.35	35.08	0.0237	N/A
	R^2	0.991	0.598	0.876	0.585	N/A
	Penetration depth (mm)	6.52	3.08	10.151	0.20	E

E*: Entire length of the sample

N/A**: Fick's second law could not be fitted on the results

Appendix. C. More discussions on the results of different binders

1. CAC3

The hydration of CAC3 is time-temperature dependent on the production of three possible phases according to Eq. (2-4) to Eq. (2-6) [43,74]:

Low temperatures (<15º): $CA+10\ H \rightarrow CAH_{10}$ Eq. (2-4)

Intermediate temperatures (15º≤ ≤30º): $2\ CA+ 16\ H \rightarrow C_2AH_8+AH_3$ Eq. (2-5)

High temperatures (30º -60º<): $3CA+ 12\ H \rightarrow C_3AH_6+2AH_3$ Eq. (2-6)

The thermodynamically stable hydration products of CAC are hydrogarnet (C_3AH_6) and gibbsite (AH_3).

For this reason, the other two unstable phases of CAH_{10} and stratlingite will convert to the two stable phases of hydrogarnet and gibbsite over time. The conversion of unstable products to stable products accompanied by a reduction in solid volume and water is released which is available to hydrate any remaining anhydrous phases [44,53].

Figure 2-4.Ap represents the iodide concentration profiles of CAC3 at different curing times. In Figure 2-4.Ap, as the curing time increased then the concentration profiles became flatter. A flatter profile means a higher diffusion rate. Figure 2-4.Ap suggests that the conversion of hydration products probably starts after 45 d and continues to increase the permeability of the samples for the studied w/c ratio in this paper. For higher w/c ratios, the conversion is more important because more water exists to convert unstable products to stable products.

2. CSA2

Figure 2-5.Ap represents the real-time series of iodide concentration profiles for the considered curing times in CSA2. Concentration profiles of curing times <90 d do not show considerable

changes compared to each other. Extending the curing time to >90 d shows a decrease in the iodide concentration profiles.

3. CSA2B

Figure 2-6.Ap shows the iodide concentration profiles in CSA2B materials at the studied curing times. As can be seen, all the profiles cured for different times performed are similar to one another. It means, extending the curing time > 35 d is not beneficial for this material.

4. AA1

Figure 2-7.Ap shows the iodide concentration profiles of AA1 binder after different curing times. Results show that curing times less than 180 d show almost the same impact on AA1.

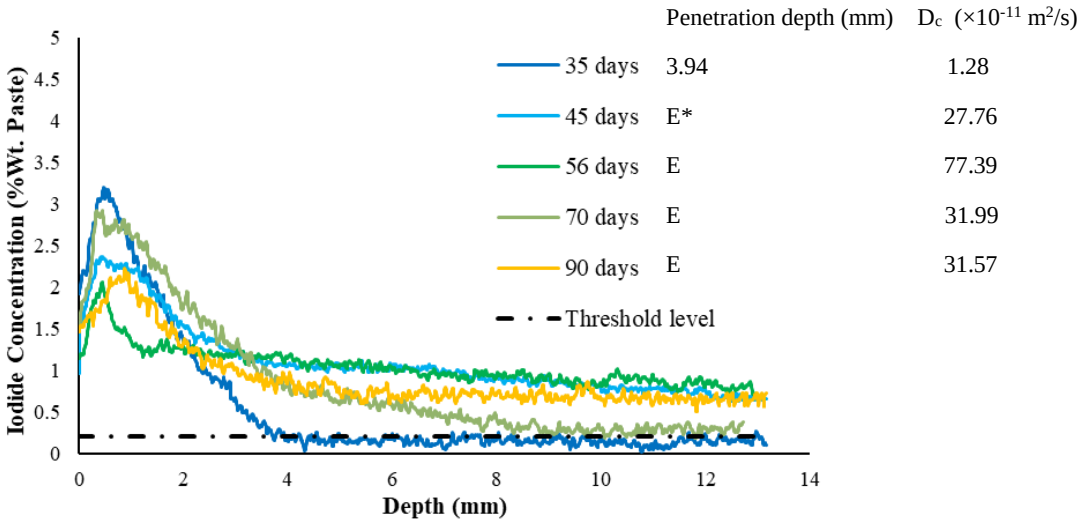

(a)

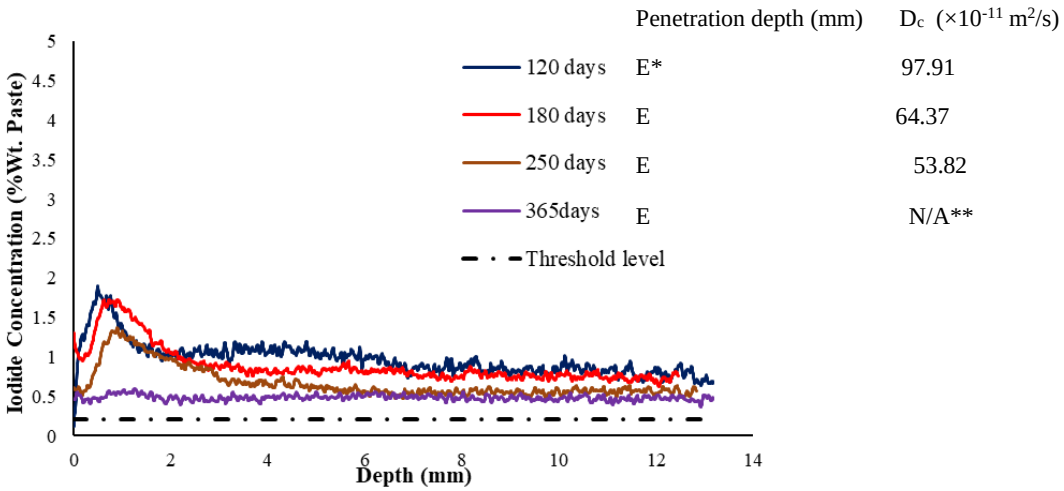

(b)

E: Entire length of the sample*

*N/A**: Fick's second law could not be fitted*

Figure 2-4.Ap. Iodide concentration profiles of CAC3 binder after different curing times a) concentration profiles for curing times 35 d≤ ≤90 d b) concentration profiles for curing times 90 d< ≤365 d

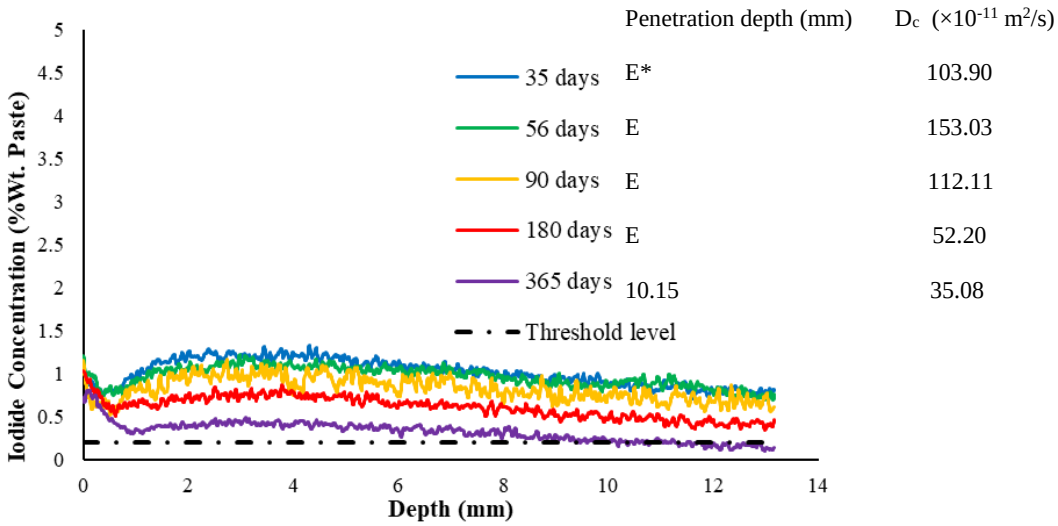

E: Entire length of the sample*

Figure 2-5.Ap. Iodide concentration profiles of CSA2 binder after different curing times

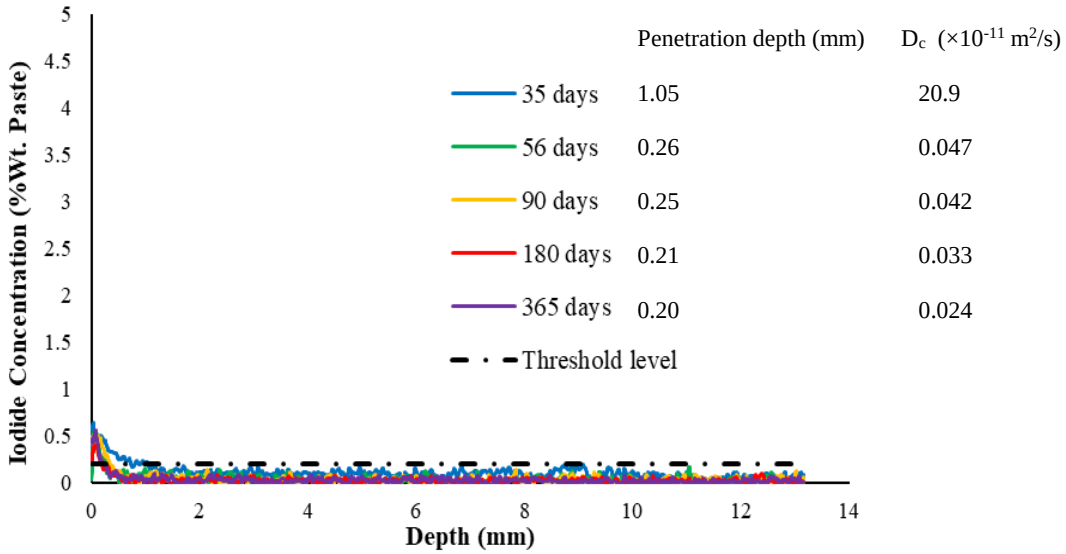

Figure 2-6.Ap. Iodide concentration profiles of CSA2B binder after different curing times

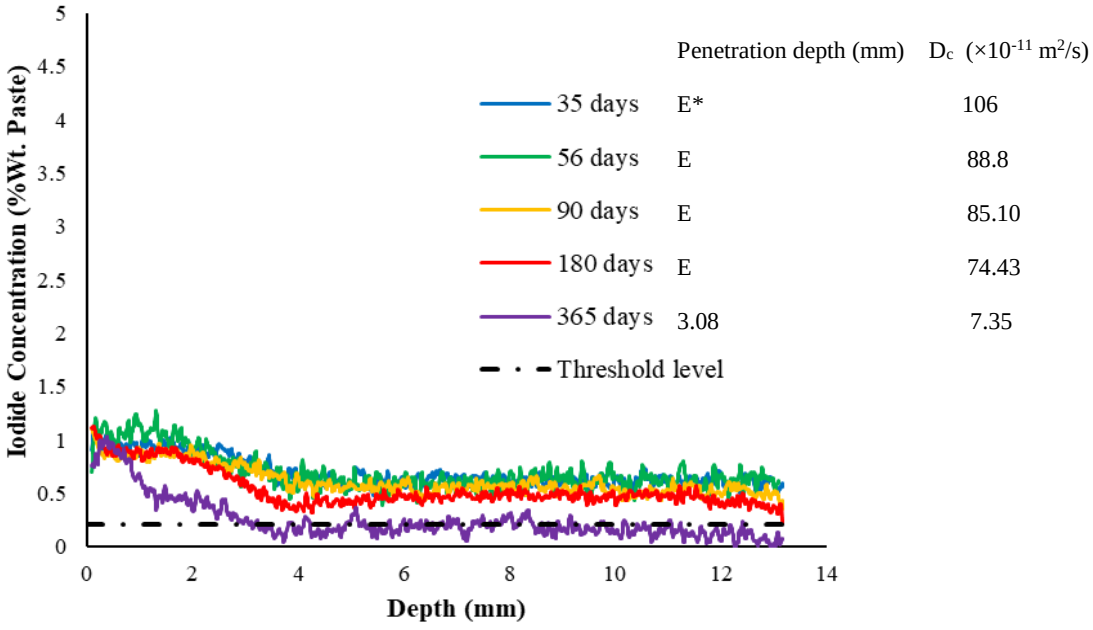

E: Entire length of the sample*

Figure 2-7.Ap. Iodide concentration profiles of AA1 binder after different curing times

CHAPTER III

LABORATORY AND FIELD INVESTIGATION OF ALTERNATIVE CEMENTITIOUS MATERIAL RESISTANCE TO CHLORIDE PENETRATION USING X-RAY IMAGING

Abstract

Alternative cementitious materials (ACMs) of calcium aluminate cement (CAC3), calcium sulfoaluminate (CSA2B), and alkali-activated binder (AA1) were investigated for chloride ion penetration in both field and laboratory samples. X-ray imaging was used to measure the concentration, depth, and rate of chloride penetration for these ACMs. The diffusion coefficient was calculated for each of the samples and the lab and field performance was compared. The results of these cementitious materials demonstrate how not all binders have the same resistance to ion penetration and can varied performance when compared to ordinary portland cement (OPC). There was a good agreement between the performance of the lab and field samples cured for 14 days with different ages for CSA2B and AA1. The CAC3 cement was the only ACM to show measurable ion binding in the lab samples cured for 14 days. Diffusion coefficient of the lab-made CAC3 sample

was lower than OPC considerably; however, the field results showed that 14 days of lab curing is not enough to evaluate the long-term performance of the CAC3 in the field. Moreover, the porosity measurements showed that porosity cannot solely represent the long-term performance of the binders both in the lab and field.

Keywords: Alternative cementitious materials, Corrosion, Chloride penetration, Diffusion coefficient, X-ray imaging, μXRF.

3.1.Introduction

The World's infrastructure has been plagued by concrete durability [1–4]. A prominent durability issue for concrete structures has been the corrosion on internal reinforcing steel. Chlorides (Cl) typically from deicing salts, ocean seawater, and contaminated aggregates can speed up the rate of corrosion [5–7]. As a result of corrosion, the concrete structure begins to crack, parts of the concrete surface spalls, a reddish-orange color stain appears on the concrete surface, and the cross-section of the reinforcement will be reduced. Therefore, the structural integrity and service life of the concrete structure diminishes, putting the concrete durability in danger [8,9]. This is why there are many methods to measure the chloride content and rate of penetration such as: AASHTO T259 (salt ponding test) [10], ASTM C 1556 (bulk diffusion test) [11], silver nitrate spray on the surface (colorimetric technique) [12,13], AASHTO T277 (rapid chloride permeability test) [14‑18], AASHTO T260 (Potentiometric Titration or Ion-Selective Electrode) [19,20] electrical migration [21‑23], resistivity [24,25], pressure-induced fluid penetration [26], sorptivity [27,28], solvent counter diffusion [29], and gas diffusion [30]. Obtaining the information about Cl concentration and rate of penetration for a concrete structure provides great insight into the long-term durability of the concrete and also allows the service life of the concrete structure to be estimated using the diffusion coefficient [31].

In recent years, alternative cementitious materials (ACMs) such as calcium aluminate cement (CAC3), calcium sulfoaluminate cement (CSA2B), and alkali-activated binder (AA1) have been increasingly used as a full or partial replacement of ordinary Portland cement (OPC) for concrete structures. These ACMs have been used because of their rapid hardening and early age strength gain that can allow traffic loads in a few hours. However, very little research has been conducted on these ACMs to understand the resistance to chloride penetration.

To provide more information, the performance of ACMs in both the lab and the field are compared. Cores were taken from field repairs that used these materials and the results were compared to laboratory performance of the same materials. These samples are investigated with micro X-ray fluorescence (μXRF) microscope that can image the Cl concentration and depth of penetration for each sample. The porosity of each sample is also measured, and the results are compared. This work aims to provide new insights into the performance of ACMs between laboratory and field measurements.

3.2.Experimental Methods

3.2.1. Materials

The laboratory samples investigated mortar mixtures containing one of the following binder types: Type I ASTM C150 ordinary Portland cement (OPC), ASTM C1600 calcium aluminate cement (CAC3), ASTM C1600 calcium sulfoaluminate with a polymer additive (CSA2B), and an alkali-activated binder (AA1) with ASTM C618 Class C fly ash. The oxide analysis of these binders used in the laboratory samples is presented in Table 3-1. Admixtures were incorporated into these laboratory mixtures based on cementitious performance. The high-range water reducer (HRWR) met the ASTM C494 standard for Type F, the high-range WR with retarder met the ASTM C494

standard for Type G, and a food-grade citric acid was used as a retarder to postpone the setting time of CSA2B. These mixtures used a natural sand meeting ASTM C33 and had a specific gravity (SG) of 2.60 and absorption of 0.86% [32].

For the field investigation, the ACM concrete samples were from the same sources as the laboratory samples. The mixture designs are unknown, but they were approved for use for the repairs and met all early age strength requirements from the respective state highway agencies. It is unfortunate that more information is not known about these mixtures, but useful comparisons can still be made about their overall performance in comparison to the laboratory samples.

Table 3-1. Chemical composition in weight percentage of binders from bulk XRF [32]

Binder Type	OPC	CSA2B	CAC3	AA1
SiO_2	17.39	14.24	5.50	38.24
Al_2O_3	4.87	14.84	45.16	17.87
Fe_2O_3	4.71	1.12	6.90	5.88
CaO	65.15	49.23	37.68	24.75
MgO	1.40	1.55	0.22	6.24
SO_3	2.51	13.55	0.07	1.56
K_2O	0.48	0.67	0.26	0.34
Na_2O	0.46	0.21	0	1.85
P_2O_5	0.13	0.11	0.09	-
TiO_2	0.39	0.70	2.11	-
Mn_2O_3	0.11	0.02	0.02	-
SrO	0.15	0.20	0.04	-
ZnO	0.03	0.01	0	-
Cr_2O_3	0.09	0.05	0.089	-
LOI	2.12	3.51	1.86	0.20

3.2.2. Sample preparation

3.2.2.1.Laboratory samples

Laboratory samples were made to compare to the field samples. These mixture proportions are shown in Table 3-2. The water-to-binder (w/b) for all of the laboratory mixtures was kept constant at 0.40, except AA1. For AA1, water was used as the plasticizer; for this reason, w/b was chosen 0.21. This was chosen because it provided a comparable slump in concrete mixtures. The AA1 binder has a two-component activator with water as a plasticizer per the manufacturer [32]. This means the w/b ratio for this material will be substantially different than the other samples. A polycarboxylate based high-range water-reducing (HRWR) admixture was used to enhance the workability for OPC and CSA2B. A food-grade citric acid was used as a retarder to postpone the setting time of CSA2B. A plasticizer with set retarder (PSR) was used to improve the workability and delay the setting time of CAC3. The mixing was done in accordance with ASTM C305 procedures [33].

Table 3-2. Laboratory mixtures proportions

Binder Type	Binder (g)	Water (g)	Aggregate (g)	HRWR (mL)	PSR (mL)	Citric Acid (g)	Activator (g)
OPC	891	354	1337	1.0	-	-	-
CSA2B	875	350	1313	0.5	-	4.0	-
CAC3	886	353	1329	-	0.4	-	-
AA1	1381	284	2284	-	-	-	55.9

Three transparent vials with dimensions of 9.5 mm diameter and 46 mm in height as shown in Figure 3-1 were used to cast the laboratory samples. The space at the top of the vial was used for ponding the solution on top of the sample to only allow penetration into the sample from the surface. Large air voids were removed from the samples by rodding with a 1.45 mm wire. Then, samples were sealed cured for 14 days in a 23°C room.

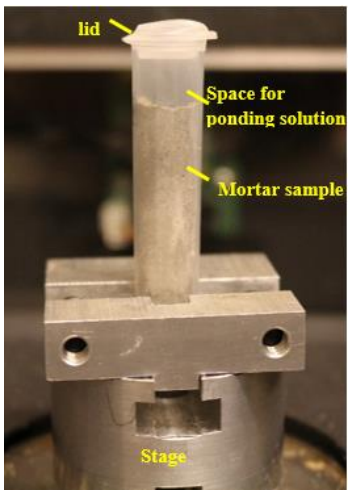

Figure 3-1. Mortar sample figuration

After curing the laboratory samples, a 0.6 mol/L NaCl solution was applied on top of the samples. This solution was renewed every five days to keep the concentration constant. Since the samples were stored within the vials this created one-directional mass transport into the samples from the surface. After 28 days of ponding, the samples were demolded, and they were polished to expose a cross-section parallel to the NaCl penetration. The polishing was done with 120 grit sandpaper belt for approximately one minute to remove any rough or uneven areas on the sample. The samples were then ready for µXRF analysis. More details about µXRF analysis are provided in section 3.2.3 and the appendix.

3.2.2.2.*Field samples*

All known mixture designs for the field samples were reported in Table 3-3. It was known that all field mixtures had water to binder ratio (w/b) < 0.45 and were placed with oversight by their respective department of transportations and the performance of these materials was deemed to be satisfactory during the mixture design approval and placement in the field. Details about each project are included in Table 3-4.

Table 3-3. Mixture proportions of the field samples per cubic meter

Location	Binder type	Binder (kg)	Water (kg)	W/b	Limestone aggregate (kg)	Natural sand (Kg)	Air (%)	Citric acid (g)
Illinois	CAC3	403	148	0.37	1068	750	5	-
Missouri	CSA2B	339	152	0.45	889	955	3.5	✓
Washington	CSA2B	N/P*	N/P	N/P	N/P	N/P	N/P	N/P
Georgia	AA1	N/P	N/P	N/P	N/P	N/P	N/P	N/P

*N/P: Not Provided

Table 3-4. State DOT ACM usage reports [34]

Binder	State usage	Application	Age (Year)	Treatment	Observation
CSA2B	Missouri	bridge deck overlay	7	Was used for a bridge in a major metropolitan area and received deicer salt applications regularly	• Low severity cracking noted; most occurred early in the deck overlays life. • Several of the cracks appear to be reflective. • Sounded various locations and appears to be well bonded. • No freeze/thaw durability cracking noted. • Surface scaling noted at several locations. • Pop-outs noted in the overlay surface.
	Washington	Pavement repair	3	The roadway was treated with a 32% CaCl2 solution as an anti-icing agent and then a blend of sand and NaCl was used to provide traction for vehicles on the roadway. However, the pavement was near the coast and so it did not receive deicer salts regularly.	• About 20 percent of panels showed cracking within a few years of placement but these had not caused performance issues. • There are no signs of durability problems.
CAC3	Illinois	Pavement repair	5-6	salted regularly with NaCl	• the material seems to be holding up well • experienced and well-organized contractors with the proper placement equipment are required to obtain satisfactory results
AA1	Georgia	Replacement slabs	11	Did not receive deicer salts regularly	• No evidence indicated salt scaling or delamination

For each location, two prisms were cut that are approximately 1.5 cm × 1.5 cm × 3.6 cm. Cutting oil was used instead of water to minimize the loss of initial Cl received in the field. Next, the samples were polished on a 120 grit sandpaper belt for approximately two minutes to remove any rough or uneven areas on the sample. This removed approximately 2 mm of the surface and helped create a flat and smooth surface for analysis with μXRF. This polishing process also exposes a surface that had not been subjected to the solution.

All the samples were scanned according to Section 3.2.3 to find the initial Cl concentration in the sample. This is the first μXRF scan of the sample and initial concentration is called C_0. After finding C_0, the samples were further processed to find their effective diffusion coefficient (D_c) and compare that to the laboratory samples. To do this the field samples were then vacuum saturated at 5 Pa for 48 hours with water. Next, a hydrophobic wax was used to cover all faces of the samples except the finished surface as shown in Figure 3-2(a). All sides of the sample were covered to force the moisture to penetrate from only the finished surface. This ensures that diffusion occurs in only one direction in the sample.

The samples are then placed in a storage container that is filled with 0.6 mol/L NaCl solution. The final setup used in this experiment is shown in Figure 3-2(b). The container in Figure 3-2(b) is partially removed for better observation of the final setup. The solution was replaced every 5 days to ensure that the concentration remained constant at the surface. The samples were removed after 28 days of ponding and then the samples were polished to expose a cross-section parallel to the NaCl penetration. The polishing was done with 120 grit sandpaper belt for approximately two minutes to remove any rough or uneven areas on the sample. The samples were then scanned with the μXRF to complete the second scan. This data will be known as C_{28}. The difference between C_0 and C_{28} will be used to determine the D_c of the sample and compare them to the values measured in the laboratory. This will be discussed in more detail later in the paper.

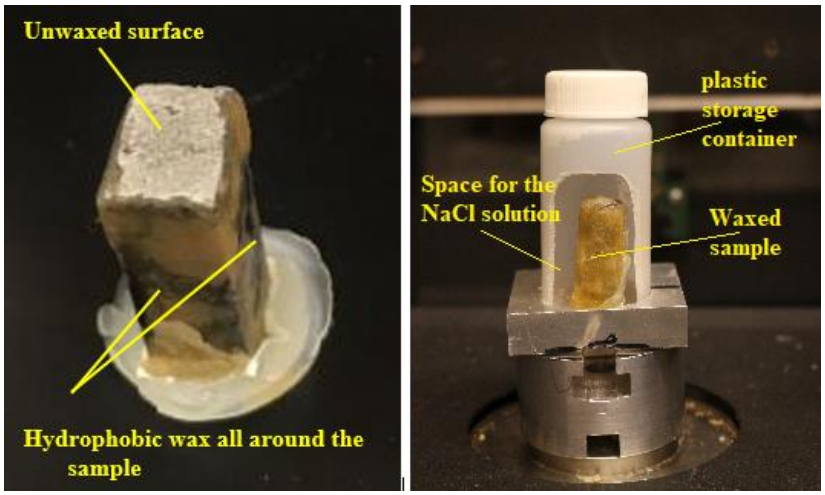

(a) (b)

Figure 3-2. a) Sample preparation before putting in the plastic storage container b) partially peeled off the final setup used in this experiment

3.2.3. µXRF imaging

Micro X-ray fluorescence (µXRF) is a non-destructive method that can collect spatially resolved maps of chemical concentrations. The instrument uses a stage to move the sample under a fixed X-ray beam. The detection limits of the technique depend on the thickness of the detector window and the distance to the sample-detector [35]. The spatial resolution of µXRF is 50 µm. Details about the instrument and the settings can be found in the appendix and other publications [36,37].

The cross-sections of the polished samples were visually investigated to find a region with a high paste fraction to study. Next, elemental maps were created for regions that are 2.3 mm across by 28 mm high on average. The X-ray detector counts the number of photons emitted from the sample at each location. This data is used to create elemental maps. The brightness of each point on each map is an indication of the concentration level of each element at each point. A typical map is shown in Figure 3-3 and other samples are included in the appendix.

To quantify the concentration of different elements, calibration curves were needed to convert the raw counts information to concentration. Calibration curves can be obtained by scanning standard

samples that are created with known concentrations of Cl. Samples from each binder were made with different Cl concentration levels. Thirty different points on each sample were scanned with the same settings used for the lab and field samples and the mean and standard deviation were determined. Then a curve was on the counts data correlated to each concentration.

To further analyze the μXRF results, the elemental maps were combined in an image processing software package called Lispix [38]. This allowed regions of unique chemical composition like aggregate and paste phases to be separated as shown in Figure 3-4. This is important because it allows the pixels that correspond to aggregate to be removed from the analysis. This is helpful because the ions primarily diffuse through the paste and not through the aggregates and this provides a more accurate Cl concentration profile as the aggregates were not uniformly distributed in the concrete. A programming code was written in Matlab [39] to only use the data from the paste phase and to detect the surface of the sample. The Matlab code considers a shell parallel to the surface with a thickness of 50 μm (which equals the used optic size) and moves it from the surface to the whole height of the scanned area to get the average counts at each depth of the paste. This technique has been compared to manual profiling and it has been shown that the concentration profiles show general agreement between the two methods, but the diffusion coefficients from μXRF were on average 30% higher than grinding technique. More details can be found in other publications [37].

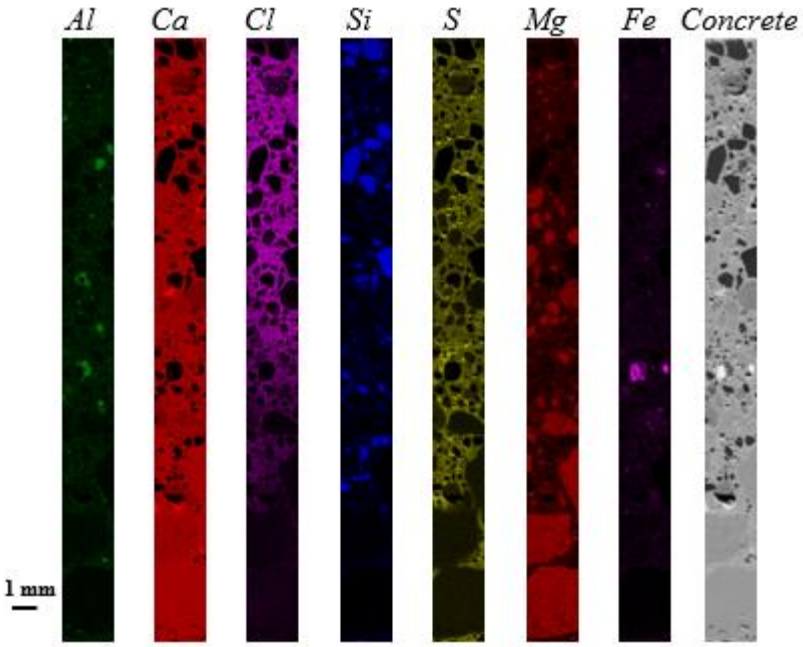

Figure 3-3. Chemical elements distribution map obtained by μXRF analysis

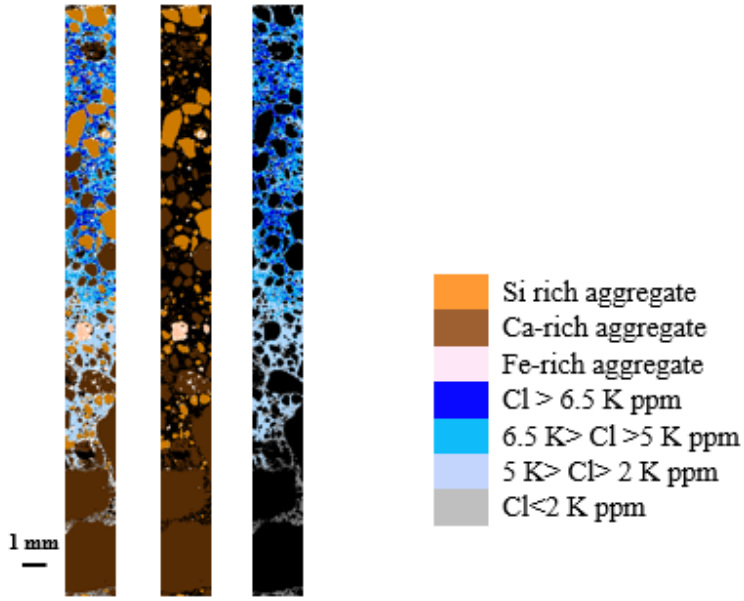

Figure 3-4. Fabricated compositional map showing concrete phase (left), aggregate phase (middle), and cement paste phase (right)

3.2.4. Determining Cl Profiles

For the laboratory samples, the Cl profiles could be obtained directly from the samples scans because these samples did not contain any Cl when they were prepared. However, this is not the case with the field samples. Since the field samples had been used in service then they received deicing treatments that created an initial Cl concentration inside the samples. To deal with this, the field samples were scanned twice. The first Cl profile was called C_0 and it is completed after receiving the samples. The second scan was completed after 28 d of ponding with 0.6 mol/L NaCl solution in the lab and it is called C_{28}. The C_{net} is concentration after 28 days of ponding in the lab. Eq. (3-1) was used to calculate C_{net}:

$$C_{net} = C_{28} - C_0 \qquad \text{Eq.(3-1)}$$

Where C_{net} was the difference between C_{28} and C_0. The net chloride concentration after 28 days is a useful method to evaluate the in-place properties of the ACM concrete without being influenced by the local salting practices for the field samples. This also allowed the mass transport of the samples from the laboratory testing to be compared to the performance of the field structures. Since both the laboratory and field samples were ponded for the same period of time with the same concentration of salt then this was a useful way to quantitatively compare the ability for the mixture to keep the Cl from penetrating into the concrete.

This work compares the depth of penetration for a Cl content of 0.21% of the paste (0.05 % of the concrete weight). This value was chosen since it was expected to cause corrosion in OPC samples [32]. This provides a useful value to compare the depth of penetration of the external Cl into the samples.

3.2.5. Calculating the diffusion coefficient (D_c) and surface concentration (C_s)

Nonlinear regression analysis by using Fick's second law was conducted on the Cl profiles from the direct measurements from the laboratory samples and the net profiles from the field samples. This allowed the surface concentration (C_s) and the diffusion coefficient (D_c) to be calculated. The general solution of Fick's second law as shown in Eq. (3-2) was used to determine the value of effective D_c and C_s. Additional details about this technique can be found in previous studies [32,37,40–43].

$$C_{(x,t)} = C_s\left(1 - \mathrm{erf}\left(\frac{x}{2\sqrt{D_c t}}\right)\right) \quad C_{(x,0)} = 0 \;\; x > 0, \;\; C_{(0,t)} = C_s \;\; t \geq 0 \qquad \text{Eq.(3-2)}$$

Where x is the distance from sample surface; t denotes time; D_c is diffusion coefficient; C_s is surface iodide concentration; C(x,t) represents iodide concentration at the depth of x from the surface after time t; and erf is the error function.

To calculate the D_c, the first part of each graph which had an upward trend was ignored. It means that for D_c calculations, concentration profiles began with the highest concentration. This was done to better fit the concentration profiles with Eq. (3-2) and get higher R^2 values.

3.2.6. Porosity testing

The porosity of each sample was determined by ASTM C 642 [44] with some minor changes. Instead of measuring the saturated mass after boiling, vacuum saturated mass was recorded. The sample was determined to be saturated when the mass change was < 0.03% after putting the samples in a vacuum chamber with 5 Pa for 24 hours. The next difference was the order of measurements. In order to prevent cracking from drying, the saturated mass was measured followed by submerged apparent mass and finally, the dried mass measurements were made. To prevent decomposition of the polymers in some samples (like CSA2B), the samples were dried at 50 ºC until an equilibrium mass change was achieved.

3.3.Results and discussions

Figure 3-5 shows the Cl concentration profiles for the laboratory samples. The C_{net} concentration profiles of field samples are represented in Figure 3-6. Each graph represents two measurements for each binder type. For a visual investigation in both Figure 3-5 and Figure 3-6, a flatter slope for the concentration profile means a higher D_c and consequently a higher rate of penetration. The porosity and D_c are compared in Figure 3-7. Surface concentrations of both lab and field samples are compared in Figure 3-8. If no error bar is shown in Figure 3-7 and Figure 3-8, it means that only one sample was able to be fit by Eq.3-2. The D_c and C_s of both lab and field samples are summarized and compared in Table 3-5. The results shown in Table 3-5 are the average of two measurements for each binder.

3.3.1. Lab samples

In Figure 3-5 the laboratory data showed consistent performance between the repeated measurements. Based on Figure 3-5, Figure 3-7(a), Figure 3-8, and Table 3-5 each ACM performs differently when compared to OPC from an early age. Lab results in Figure 3-5 show that CAC3 has the lowest penetration depth and has a sharp slope which indicates a low D_c after 14 days of curing. Results in Figure 3-8 show that CAC3 has 1.65x higher C_s than OPC and had the highest C_s among all tested samples. Higher values of C_s signify the capability of binding more ions. A high level of Al_2O_3 oxides of CAC3 (50%–60%) possibility has led to binding more Cl ions near the surface [47]. Aluminum hydration products have been shown to bind ions and form more stable products such as Friedel's salt. This seems to be happening at early ages in CAC3. CAC3 showed 6x less penetration (to reach the zero concentration) than OPC.

Lab results shown in Figure 3-7(a) indicate that AA1 and CSA2B lab samples showed 2.85x and 4x higher D_c compared to OPC, respectively. In both AA1 and CSA2B samples in the lab Cl penetrated to the whole length of the sample while for OPC after the depth of 13.25 mm no Cl was

observed in the sample. One possible reason for CSA2B to have a higher depth of penetration is the high pore interconnectivity due to the non-uniform formation of ettringite crystals (AFt). One possible reason for observing higher D_c for AA1 compared to OPC can be due to a low degree of crystallinity of calcium silicate hydrate (C–S–H) or inadequate formation of the tobermorite-type calcium silicate hydrate phase ($Ca_5Si_6O_{16}(OH)_2$) phase in 14 days. AA1 and CSA2B showed the lowest surface concentration which shows that these two materials have a weak potential of binding ions. Generally, AA1 and CSA2B showed less resistance to outside chemical transport into the samples compared to OPC.

3.3.2. Field samples

CAC3-field samples showed very low net Cl concentrations in Figure 3-6. Results in Table 3-5 confirm that the D_c value of CAC3 has a very poor R^2 value (R^2=0.014) and therefore cannot be considered in the quantitative discussion. However, comparisons could be made on the depth of Cl penetration and the porosity of the samples and by adopting a visual comparison. A visual inspection of Figure 3-6 shows that there was little binding in CAC3 field samples because both measurements on CAC3 field samples showed the lowest surface concentration among all tested samples. Also, the CAC3 field sample showed a 10x higher penetration depth compared to the lab sample to reach the threshold level. The recent results are not in accordance with the lab results discussed above. In the laboratory testing, the CAC3 samples showed the highest C_s, limited depth of penetration within the samples. This may imply that 14 days of curing is not enough to evaluate the long-term performance of CAC3. One reason for the worse performance of the field sample may be the conversion of the microstructure for CAC binders [48]. Conversion reduces the solid volume and also the binding capacity. The binding was beneficial as it does not allow Cl to penetrate the concrete and reach the reinforcing steel. Since conversion happens over time, longer curing times for lab samples may give more realistic results for CAC3. Further work is needed to be able to evaluate the long-term performance of CAC3. This is the subject of future work.

A visual investigation in Figure 3-6 reveals that both CSA2B-M and CSA2B-W showed a flat profile with deep penetration similar to what has been obtained in the lab testing after 28 days of ponding. Figure 3-7(b) shows that CSA2B-M had a high D_c in the field (>50 $\times 10^{-12}$ m^2/s) which is 1.7x higher than the D_c in the lab. This can be due to the transition zones that exist in the concrete field samples. In Figure 3-8, both CSA2B field and lab data showed minimal binding. The CSA2B-M lab sample had 1.5x higher C_s compared to the field sample. It still indicates that there is an acceptable agreement between field and lab data for CSA2B for three main reasons: 1- transition zones in the concrete samples interfere with the fluid transport in sample 2- CSA2B-M field sample had >180x more age than CSA2B lab sample, 3- CSA2B-M was under service load which can induce microcracks in the concrete as noted in Table 3-4. In Figure 3-6 only one measurement is represented for CSA2B-W because one of the samples was broken during preparation. For the other CSA2B-W sample only the surface could be evaluated because this sample broke in half during preparation. Since there was not enough data for the CSA2B-W sample, D_c could not be calculated for this sample, but visual inspection shows that both field and lab samples show similar slopes that are flat for the CSA2B concentration profile. Both field and lab results showed that CSA2B does not show good resistance against Cl penetration.

Contrary to the lab results, AA1 field data had some anomalies. The results of the first measurement of AA1 in Figure 3-6 showed a sudden jump in the Cl content about 12 mm from the surface. This seems to be caused by a crack with an average width of 28 μm in the sample that initiated from the surface. It seems that this crack has allowed Cl to penetrate at a faster rate in this region. Details of this crack are shown in the appendix. For this reason, Eq. (3-2) was fitted on the results of the first measurement at depths between 2.25 mm and 10.75 mm where the crack does not exist. Results of the second measurement of AA1 sample with high Cl concentration peaks near the surface as shown in Figure 3-6 reveal an irregular behavior in the Cl concentration profile. This may be caused by some anomalies that are not observable on the exposed cross-section. For this reason, the results of

the second measurement were not considered in the average of D_c calculated for AA1 presented in Table 3-5. AA1 field sample with 11 years old of service life is a very mature sample. For this reason, the D_c of AA1 field sample was 3.4x less than the D_c of AA1 lab sample. One reason for the improved D_c for AA1 field sample is that the increase in the sample age is accompanied by an increase in the formation of the tobermorite-type calcium silicate hydrate phase. For both field and lab AA1 samples, the penetration depth is greater than the studied area to reach the zero concentration as represented in Table 3-5. Figure 3-7(b) indicates that similar to lab samples, AA1 had a lower D_c compared to CSA2B. Both field and lab samples showed that AA1 does not have good resistance to chloride penetration even if the concrete is mature. The reader must remember that the type of fly ash, the activity and chemical consistency of the activator, and the temperature has important impacts on the hydration mechanism of this type of ACMs and consequently affect its binding capacity [45,46]. This means that changes in materials may produce different results. Despite the lack of information on the mixture design of AA1 field samples, the lab results provided good insight into the long-term performance of AA1 field samples.

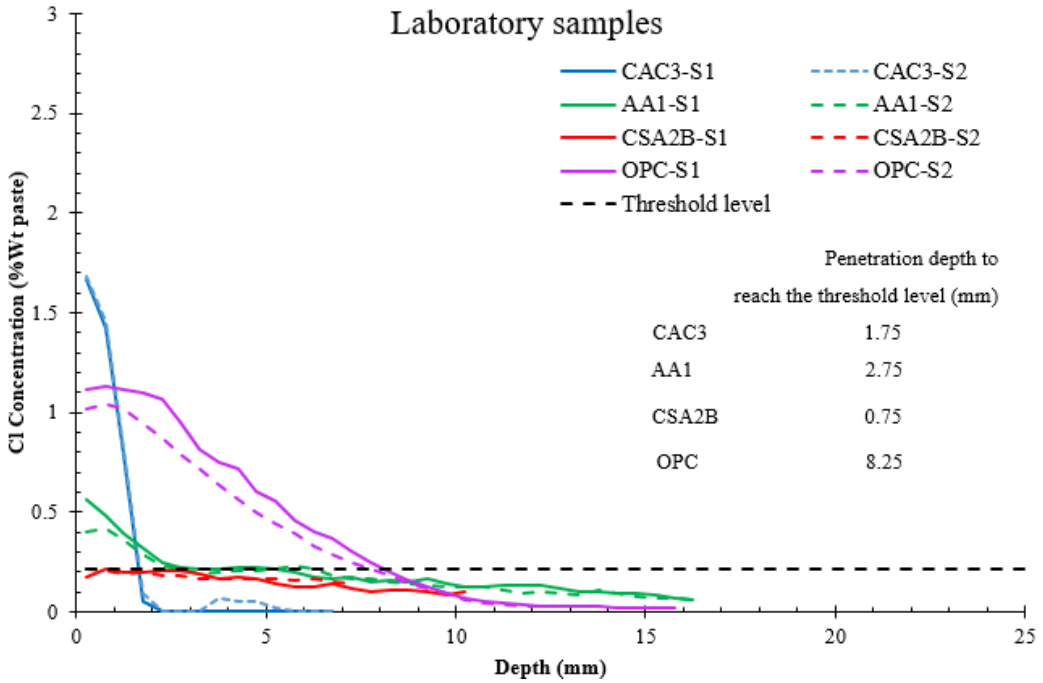

Figure 3-5. Cl concentration profiles for the laboratory samples after 14 days of curing and 28 days of ponding.

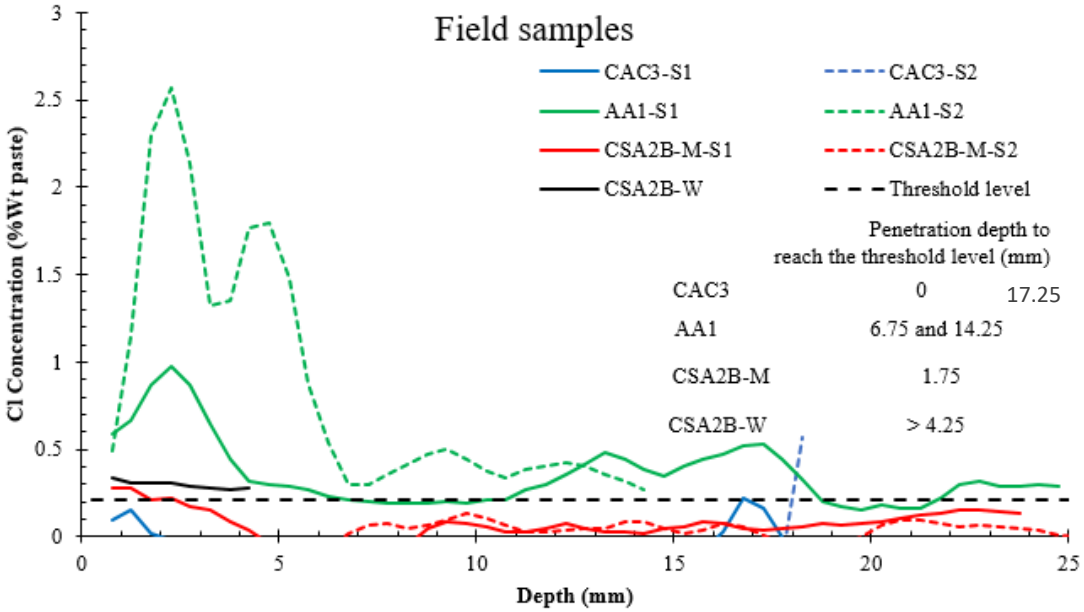

Figure 3-6. Net Cl concentration profiles for field samples after 28 days of ponding

Note: (CSA2B-M= CSA2B sample collected from Missouri CSA2B-W= CSA2B samples collected from Washington)

Table 3-5. Mass transport properties of lab and field samples

Binder	$D_c \times 10^{-12}$ (m^2/sec)	R^2	C_s (%wt paste)	Penetration depth to zero concentration (mm)	Penetration depth to threshold level (mm)	Porosity (%)	Std.
OPC	7.65	0.98	1.33	13.25	8.25	33.18	0.07
CAC3-Lab	0.30	0.95	2.19	2.25	1.75	25.8	0.47
CAC3-Field	0.42	0.014	0.21	17.75	17.25	13.47	5.67
AA1-Lab	21.80	0.78	0.39	>16	2.75	18.17	0.32
AA1-Field	6.50	0.80	1.07	>24	6.75	9.19	0.97
CSA2B-Lab	30.60	0.89	0.22	>10	0.75	18	0.95
CSA2B-M	51.8	0.24	0.15	>24	1.75	20.29	4.47
CSA2B-W	N/A	N/A	N/A	N/A	N/A	14.89	3.67

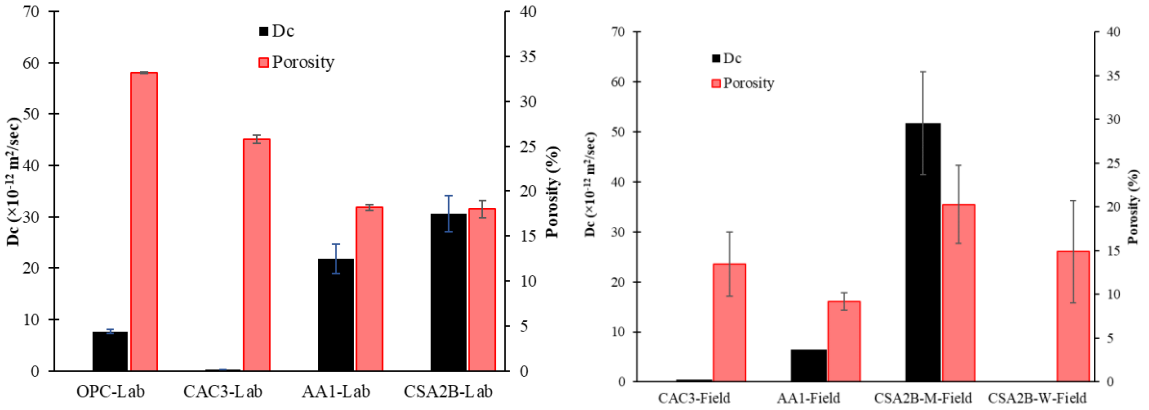

(a) (b)

Figure 3-7. Comparing the porosity and diffusion coefficients for a) lab mortar sample b) field concrete samples

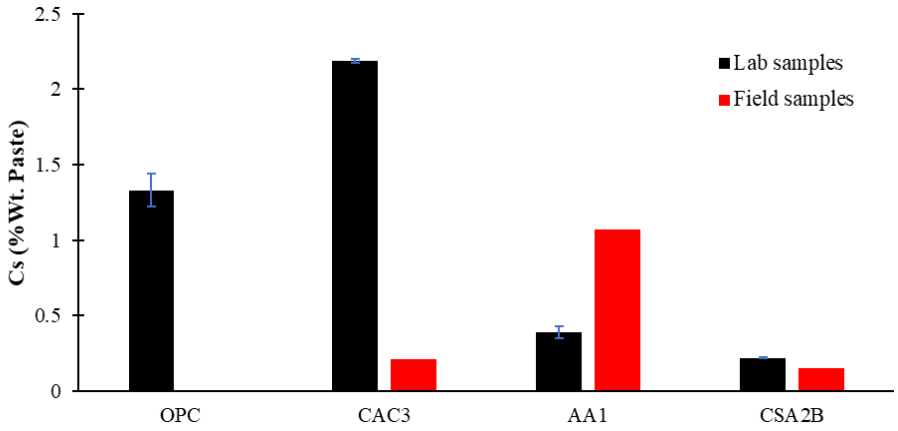

Figure 3-8. Surface concentration for both lab and field samples

3.3.3. Porosity measurement

Porosity results are represented in Figure 3-7. Porosity testing was completed for all of the laboratory and field samples. Figure 3-7(a) shows the porosity for the ACMs used to make mortar at the lab. All of the ACMs have a lower porosity compared to OPC. CAC3 showed 43% higher porosity compared to AA1 and CSA2B on average. Figure 3-7(b) shows the porosity of the concrete field samples. The CSA2B field samples on average showed a higher porosity than CAC3 and AA1 by 51% and 91%, respectively. The difference between porosity measurements in the lab and field is due to the differences in concrete compared to mortar, mixture design, casting practice, and curing. Moreover, since the porosity measures the total volume of pores in the paste phase, the existence of aggregate in a small sample will change the proportion of paste existed in the tested sample and therefore change the porosity. Moreover, the field samples have all been in service for > 3 years. For this reason, the concrete samples with less paste proportion and older ages compared to lab samples have lower porosity. For example, the field samples for AA1 had a 49.4% lower porosity than the AA1 lab samples and CAC3 field samples had a 47.8% lower porosity than the lab sample. One must remember that the porosity of a sample gives the total volume of pores and does not provide insight into how these pores were arranged. Furthermore, the pore arrangement

and ability for the material to bind chlorides were much more important to determine the mass transport properties.

Comparing the porosity and D_c as shown in Figure 3-7 reveals that porosity is not a reliable method to evaluate the resistance of ion penetration into the different ACM binders. For instance, AA1 and CSA2B lab samples have lower porosity than OPC but their D_c values are not the lowest. The reason is that the porosity gives the overall volume of the pores in a sample and cannot measure the interconnectivity and pore arrangement which are more important in mass transport through cementitious based materials.

3.4.Practical Significance

Most durability experiments are completed on lab samples. There is a concern about the agreement between the long-term performance of concrete in the field and the results obtained from the lab testing. This work investigated the mass transport properties of both laboratory mortar samples and field concrete samples made with similar binders. The results of field samples were compared with the results obtained from lab-made samples. On the other hand, the long-term performance of using alternative cementitious materials (ACMs) is not well known. Like other new materials, enough evidence is needed to learn about long-term performance.

This study showed that conducting diffusion experiment on 14 days cured AA1 and CSA2B lab-made mortar samples can help to get an insight into the long-term chloride penetration into samples with these binders in the field. Both the lab and field results showed that CSA2B and AA1 binders have poor resistance against Cl penetration. The observed quantitative differences between lab and field measurements are due to the differences in concrete compared to mortar, mixture design, casting practice, curing regime, age, and service load.

Furthermore, the results of this study revealed that 14 days of curing for CAC3 is not enough to evaluate the long-term performance of this binder. Lab mortar CAC3 samples cured for 14 days showed excellent mass transport resistance properties while the results of the concrete field samples with six years of performance showed poor resistance against mass transport. For this reason, more research is needed to better understand how the diffusion coefficients change for CAC3 at different curing times. It should be noted that this paper focused solely on the outside penetration of Cl ions and not on subsequent reactions like corrosion or salt attack that may come afterward. These deterioration processes would have to be studied with these ACMs in relevant conditions to determine how the pore solution and chemical consistency of the matrix change these values.

3.5.Conclusions

This work systematically examined the performance of ACMs in both laboratory and field applications. The ACMs considered are calcium aluminate cement (CAC3), calcium sulfoaluminate cement with a pore reducing additive (CSA2B), and an alkali-activated binder with a Class C fly ash (AA1). The study compared these materials on their porosity, depth of Cl penetration, and diffusion coefficient for laboratory and field applications. This work compares both laboratory and field usage of ACMs and shows that not all binders have the same resistance to chloride (Cl) penetration. This means that the performance of these materials must be well understood before their widespread use can be recommended to provide long term durability in Cl rich environments. Generally, the following conclusions can be drawn:

- For CAC3, 14 days of lab curing was not enough to reflect the long-term performance of the field sample. CAC3 lab results showed an excellent durability performance against Cl penetration while CAC3 field samples with 6 years old showed poor resistance to Cl transport.

- The CAC3 lab sample was the only ACM to show a higher surface concentration than OPC. This suggests a higher level of surface binding. This was important as it will decrease the level of ions that penetrate into the concrete. This was not the case for the CAC3 field sample.

- There was a good agreement between laboratory and field results for CSA2B and AA1 because both lab and field results showed CSA2B and AA1 have worse resistance to Cl penetration than OPC. This matches the laboratory results.

- CSA2B and AA1 binders showed minimal binding both in the lab and field.

- Porosity by itself does not represent the performance of concrete against fluid transport into concrete because the void distribution and connectivity play important roles in this process.

References

[1] M.G. Stewart, D. V. Rosowsky, Time-dependent reliability of deteriorating reinforced concrete bridge decks, Structural Safety. 20 (1998) 91–109. doi:10.1016/S0167-4730(97)00021-0.

[2] P.K. Mehta, Greening of the concrete industry for sustainable development, Concrete International. 24 (2002) 23–28.

[3] C.L. Page, M.M. Page, Durability of concrete and cement composites, (2007).

[4] S.-H. Han, W.-S. Park, E.-I. Yang, Evaluation of concrete durability due to carbonation in harbor concrete structures, Construction and Building Materials. 48 (2013) 1045–1049. doi:https://doi.org/10.1016/j.conbuildmat.2013.07.057.

[5] P.D. Cady, R.E. Weyers, Chloride penetration and the deterioration of concrete bridge decks, Cement, Concrete and Aggregates. 5 (1983) 81–87.

[6] A. Costa, J. Appleton, Chloride penetration into concrete in marine environment—Part I: Main parameters affecting chloride penetration, Materials and Structures. 32 (1999) 252.

[7] F. Debieb, L. Courard, S. Kenai, R. Degeimbre, Mechanical and durability properties of concrete using contaminated recycled aggregates, Cement and Concrete Composites. 32 (2010) 421–426.

[8] A. Neville, Chloride attack of reinforced concrete: an overview, Materials and Structures. 28 (1995) 63.

[9] A. Ababneh, F. Benboudjema, Y. Xi, Chloride penetration in nonsaturated concrete, Journal of Materials in Civil Engineering. 15 (2003) 183–191.

[10] AASHTO T 259, Resistance of Concrete to Chloride Ion Penetration, (1980).

[11] ASTM C1556, Standard Test Method for Determining the Apparent Chloride Diffusion Coefficient of Cementitious Mixtures by Bulk Diffusion, (2016).

[12] E. Meck, V. Sirivivatnanon, Field indicator of chloride penetration depth, Cement and Concrete Research. 33 (2003) 1113–1117.

[13] V. Baroghel-Bouny, P. Belin, M. Maultzsch, D. Henry, AgNO3 spray tests: advantages, weaknesses, and various applications to quantify chloride ingress into concrete. Part 2: Non-steady-state migration tests and chloride diffusion coefficients, Materials and Structures. 40 (2007) 783.

[14] AASHTOT277-93, Electrical Indication of Concrete's Ability to Resist Chloride, (1983).

[15] ASTM C1202-19, Standard Test Method for Electrical Indication of Chloride's Ability to Resist Chloride, (2019).

[16] T. Zhang, O.E. Gjørv, An electrochemical method for accelerated testing of chloride diffusivity in concrete, Cement and Concrete Research. 24 (1994) 1534–1548.

[17] R.K. Dhir, M.R. Jones, H.E.H. Ahmed, A.M.G. Seneviratne, Rapid estimation of chloride diffusion coefficient in concrete, Magazine of Concrete Research. 42 (1990) 177–185.

[18] P.E. Streicher, M.G. Alexander, A chloride conduction test for concrete, Cement and Concrete Research. 25 (1995) 1284–1294.

[19] AASHTO T260-94, Standard Method for Sampling and Testing for Chloride Ion in Concrete and Concrete Raw Materials, (1994).

[20] M.A. Climent, G. de Vera, J.F. López, E. Viqueira, C. Andrade, A test method for measuring chloride diffusion coefficients through nonsaturated concrete: Part I. The instantaneous plane source diffusion case, Cement and Concrete Research. 32 (2002) 1113–1123.

[21] A. Delagrave, J. Marchand, E. Samson, Prediction of diffusion coefficients in cement-based materials on the basis of migration experiments, Cement and Concrete Research. 26 (1996) 1831–1842.

[22] C. Ozyildirim, Rapid Chloride permeability testing of sílica-fume concrete, Cement, Concrete and Aggregates. 16 (1994) 53–56.

[23] A.A. Kyi, B. Batchelor, An electrical conductivity method for measuring the effects of additives on effective diffusivities in portland cement pastes, Cement and Concrete Research. 24 (1994) 752–764.

[24] C. Andrade, C. Alonso, S. Goni, Possibilities for electrical resistivity to universally characterise mass transport processes in concrete, Proceedings of the Concrete 2000 Conference. 2 (1993) 1639–1652.

[25] C. Andrade, Calculation of chloride diffusion coefficients in concrete from ionic migration measurements, Cement and Concrete Research. 23 (1993) 724–742.

[26] P. Halamickova, R.J. Detwiler, D.P. Bentz, E.J. Garboczi, Water permeability and chloride ion diffusion in Portland cement mortars: relationship to sand content and critical pore diameter, Cement and Concrete Research. 25 (1995) 790–802.

[27] C. Hall, Water sorptivity of mortars and concretes: a review, Magazine of Concrete Research. 41 (1989) 51–61.

[28] N.S. Martys, C.F. Ferraris, Capillary transport in mortars and concrete, Cement and Concrete Research. 27 (1997) 747–760.

[29] R.F. Feldman, Diffusion measurements in cement paste by water replacement using propan-2-ol, Cement and Concrete Research. 17 (1987) 602–612.

[30] A. Sharif, K.F. Loughlin, A.K. Azad, C.M. Navaz, Determination of the effective chloride diffusion coefficient in concrete via a gas diffusion technique, Materials Journal. 94 (1997) 227–233.

[31] E. Proverbio, F. Carassiti, Evaluation of chloride content in concrete by X-ray fluorescence, Cement and Concrete Research. 27 (1997) 1213–1223.

[32] M. Khanzadeh Moradllo, M.T. Ley, Comparing ion diffusion in alternative cementitious materials in real time by using non-destructive X-ray imaging, Cement and Concrete Composites. 82 (2017) 67–79.

[33] ASTM C305, Standard Practice for Mechanical Mixing of Hydraulic Cement Pastes and Mortars of Plastic Consistency, (2006).

[34] Federal Highway Administration Research and Technology, Novel Alternative Cementitious Materials for Development of the Next Generation of Sustainable Transportation Infrastructure, (n.d.). https://www.fhwa.dot.gov/publications/research/ear/16017/003.cfm#si1.

[35] M. Haschke, Laboratory micro-X-Ray fluorescence spectroscopy, Springer International Publishing. 10 (2014) 978–983.

[36] EDAX, X-Ray Fluorescence Metrology Tools-Technology Guide, (2016).

[37] M. KhanzadehMoradllo, B. Sudbrink, Q. Hu, M. Aboustait, B. Tabb, M.T. Ley, J.M. Davis, Using micro X-ray fluorescence to image chloride profiles in concrete, Cement and Concrete Research. 92 (2017) 128–141.

[38] D.S. Bright, LISPIX: image processing and data visualization tool for the PC and Macintosh, SCANNING J SCANNING MICROSC. 22 (2000) 111–112.

[39] MATLAB (R2016a), version 9.0.0, (2016).

[40] B. Sudbrink, M. Khanzadeh Moradllo, Q. Hu, M.T. Ley, J.M. Davis, N. Materer, A. Apblett, Imaging the presence of silane coatings in concrete with micro X-ray fluorescence, Cement and Concrete Research. 92 (2017) 121–127. doi:10.1016/j.cemconres.2016.11.019.

[41] M. Khanzadeh Moradllo, M.T. Ley, Quantitative measurement of the influence of degree of saturation on ion penetration in cement paste by using X-ray imaging, Construction and Building Materials. 141 (2017) 113–129. doi:10.1016/J.CONBUILDMAT.2017.03.007.

[42] M. Khanzadeh Moradllo, B. Sudbrink, Q. Hu, M. Aboustait, B. Tabb, M.T. Ley, J.M. Davis, Using micro X-ray fluorescence to image chloride profiles in concrete, Cement and Concrete Research. 92 (2017) 128–141.

[43] M. Khanzadeh Moradllo, Q. Hu, M.T. Ley, Using X-ray imaging to investigate in-situ ion diffusion in cementitious materials, Construction and Building Materials. 136 (2017) 88–98.

[44] ASTM C642, Standard Test Method for Density, Absorption, and Voids in Hardened Concrete, (2013).

[45] O. Burciaga-Díaz, J.I. Escalante-García, Structure, mechanisms of reaction, and strength of an alkali-activated blast-furnace slag, Journal of the American Ceramic Society. 96 (2013) 3939–3948.

[46] D.M. Roy, W. Jiang, M.R. Silsbee, Chloride diffusion in ordinary, blended, and alkali-activated cement pastes and its relation to other properties, Cement and Concrete Research. 30 (2000) 1879–1884.

[47] S.H. Jin, H.J. Yang, J.P. Hwang, K.Y. Ann, Corrosion behaviour of steel in CAC-mixed concrete containing different concentrations of chloride, Construction and Building Materials. 110 (2016) 227–234. doi:10.1016/j.conbuildmat.2016.02.032.

[48] C. Gosselin, Microstructural development of calcium aluminate cement based systems with and without supplementary cementitious materials, (2009).

[49] K.H.A. Janssens, F. Adams, A. Rindby, Microscopic X-ray fluorescence analysis, Wiley Chichester, 2000.

[50] K. Janssens, B. Vekemans, L. Vincze, F. Adams, A. Rindby, A micro-XRF spectrometer based on a rotating anode generator and capillary optics, Spectrochimica Acta Part B: Atomic Spectroscopy. 51 (1996) 1661–1678

APPENDICES

Appendix. A. μXRF analysis

The μXRF analysis in this work was conducted using the Orbis by EDAX with the stings summarized in Table 3-1.Ap This instrument has a chamber size of 350 mm in diameter, an 80 mm^2 Silicon Drift Detector Energy Dispersive Spectrometer (SDD-EDS), and a rhodium X-ray tube which focuses the produced polychromatic x-ray beams by using one of the three stationary X-ray optics. In this imaging technique, the sample will be loaded on a motorized stage which can move in three directions of X, Y, and Z. By finding the optimum dimension of Z which obtains the highest resolution, the focal length becomes fixed to ensure a consistent geometry between the X-ray source, sample, and detector. The capillary optic in the instrument focuses x-ray beams to a specific diameter on the sample and causes characteristic fluorescence X-rays to be emitted at each spot. The X-ray detector counts the number of photons emitted from the samples from each energy level (counts data) which was typically called a spectrum. This data was used to identify and quantify the existing chemical elements at 0.1% by weight. In addition, this method gives chemical elements distribution maps of individual elements that a sample contains as shown in Figure 3-3. Figure 3-2.Ap to Figure 3-5.Ap show three important chemical maps of all field samples in both scans (before ponding and after ponding). In this study, the chamber becomes vacuumed to reduce the absorption of X-ray emission by N_2, O_2, and Ar gases [49,50].

Table 3-1.Ap. Settings used in µXRF x-ray imaging technique

Parameter	µXRF settings
Pixel size (µm)	50
Voltage (KeV)	40
Current (µA)	1000
Filter	25 µm Al
Acquisition time(dwell time)	400 ms/pixel
Chamber condition	vacuum
Deadtime	Maximum of 20%

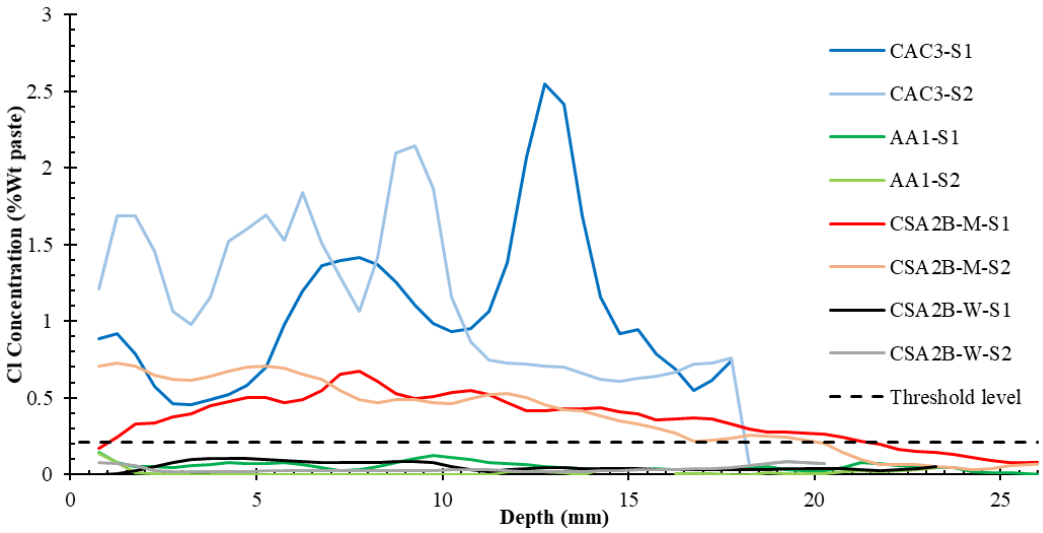

Figure 3-1.Ap. Initial Cl concentration profiles

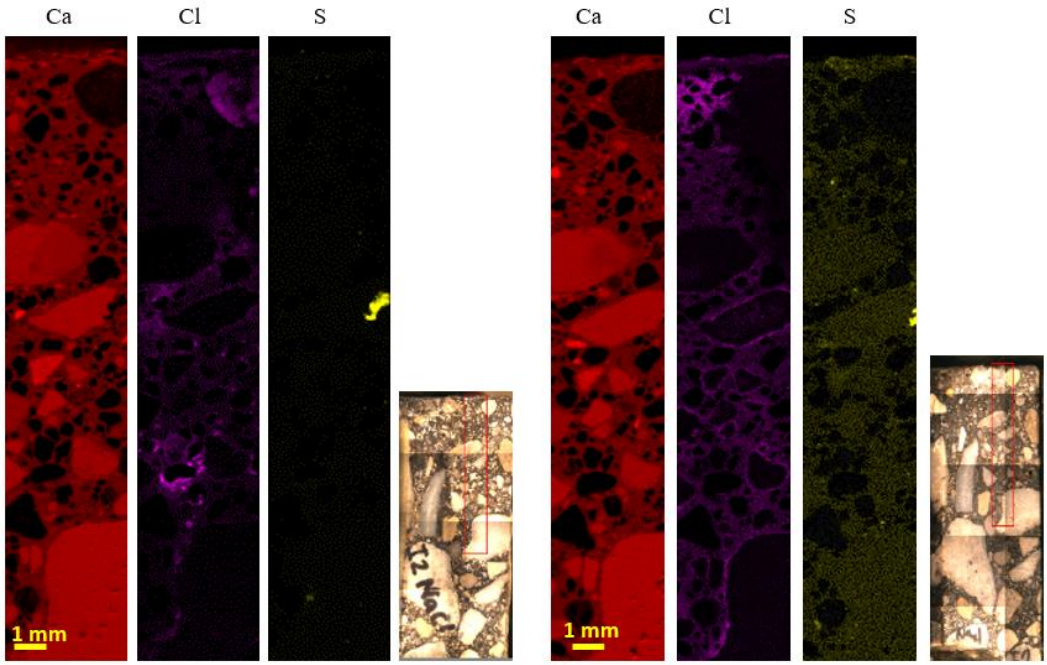

Results before ponding

Results after 28 days of ponding

(a)

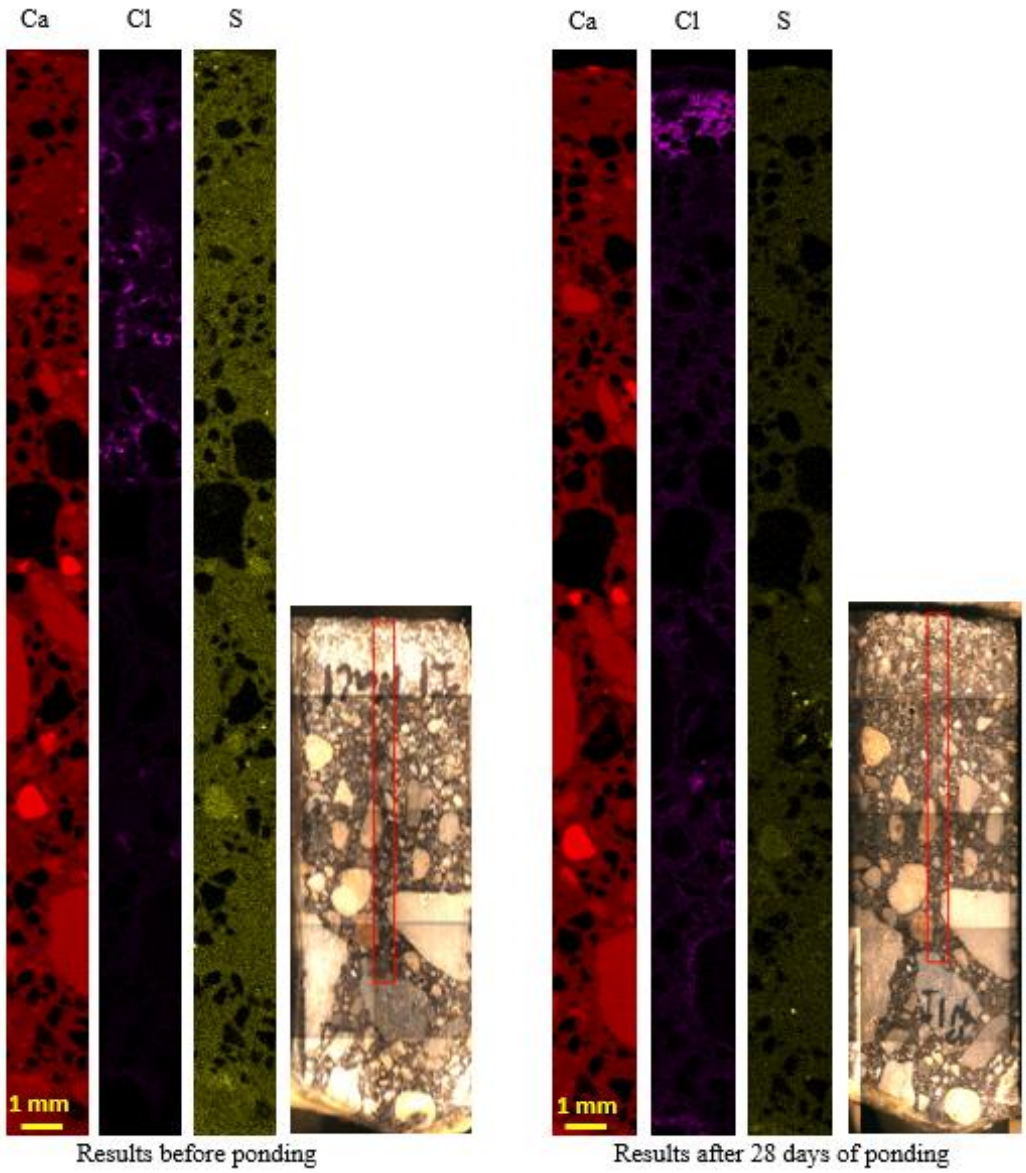

(b)

Figure 3-2.Ap. µXRF results of CAC3 field samples a) the first measurement b) the second measurement

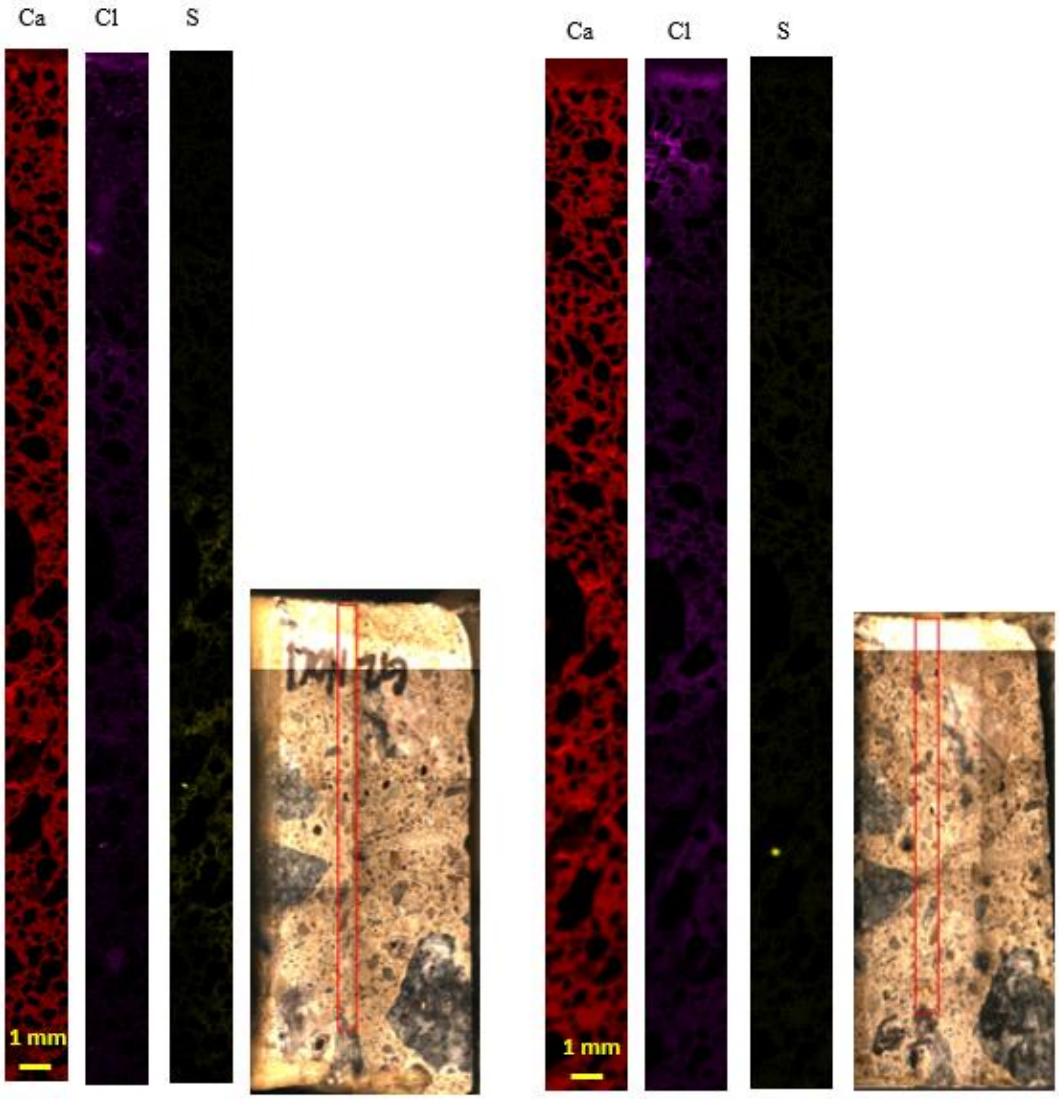

Results before ponding

Results after 28 days of ponding

(a)

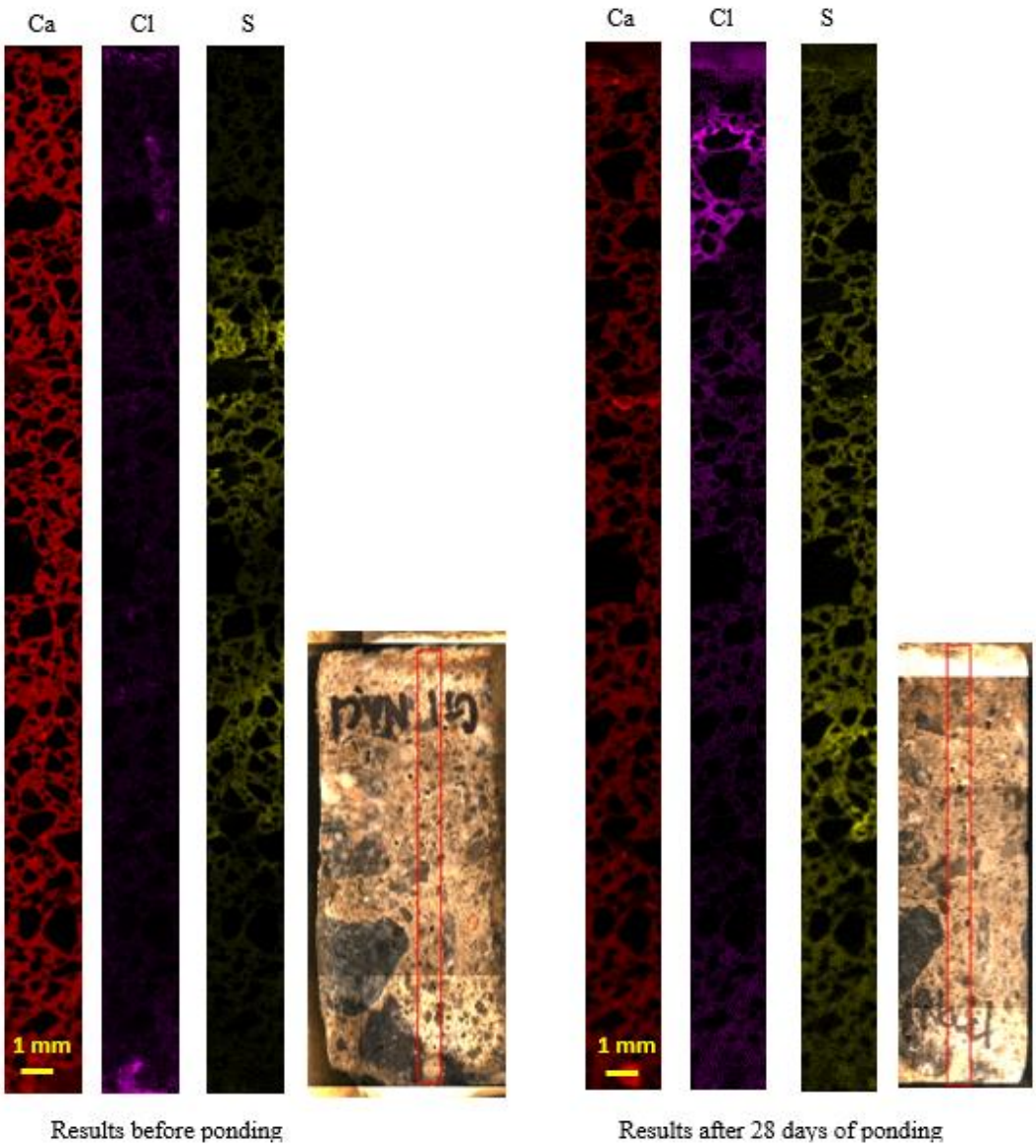

(b)

Figure 3-3.Ap. µXRF results of AA1 field samples a) the first measurement b) the second measurement

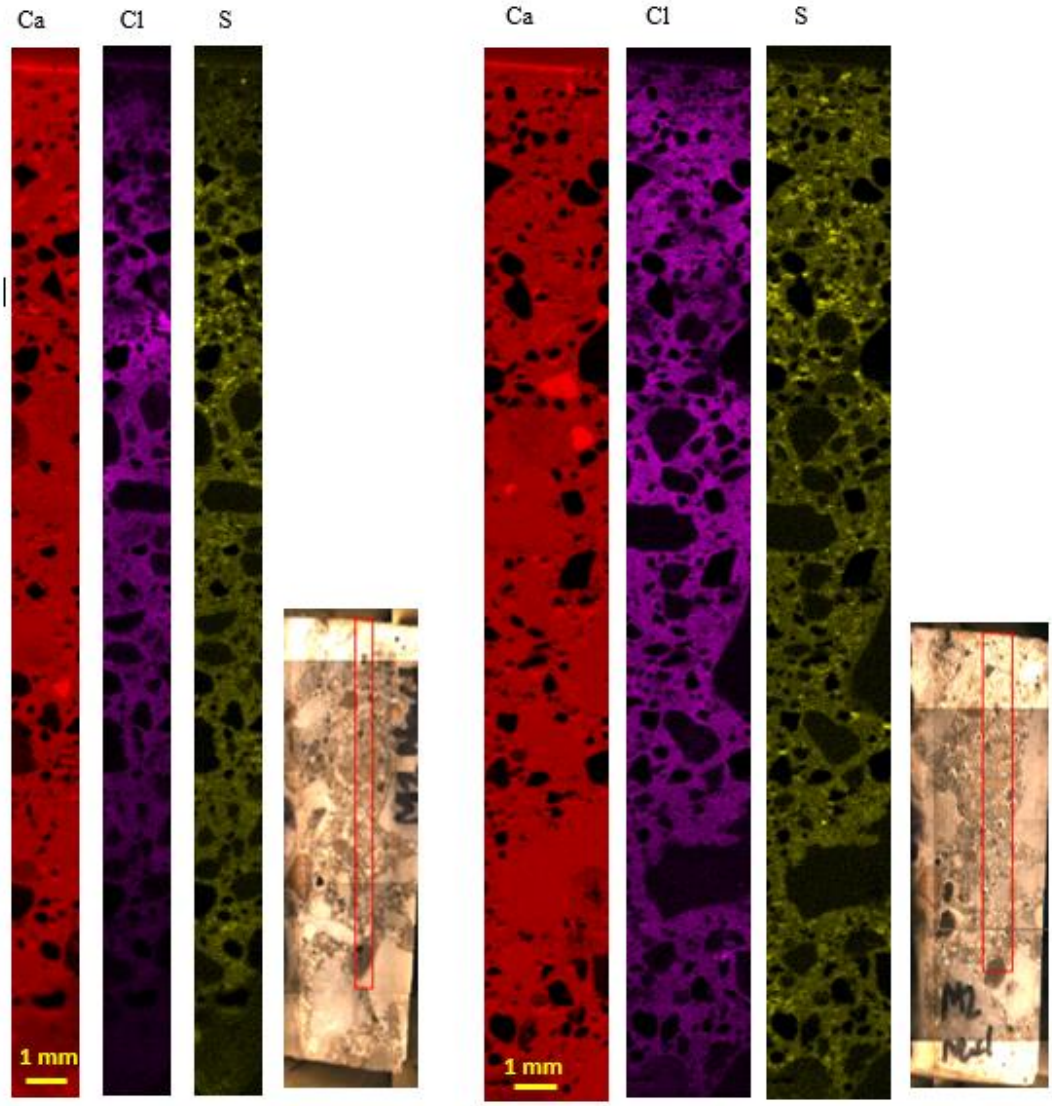

Results before ponding

Results after 28 days of ponding

(a)

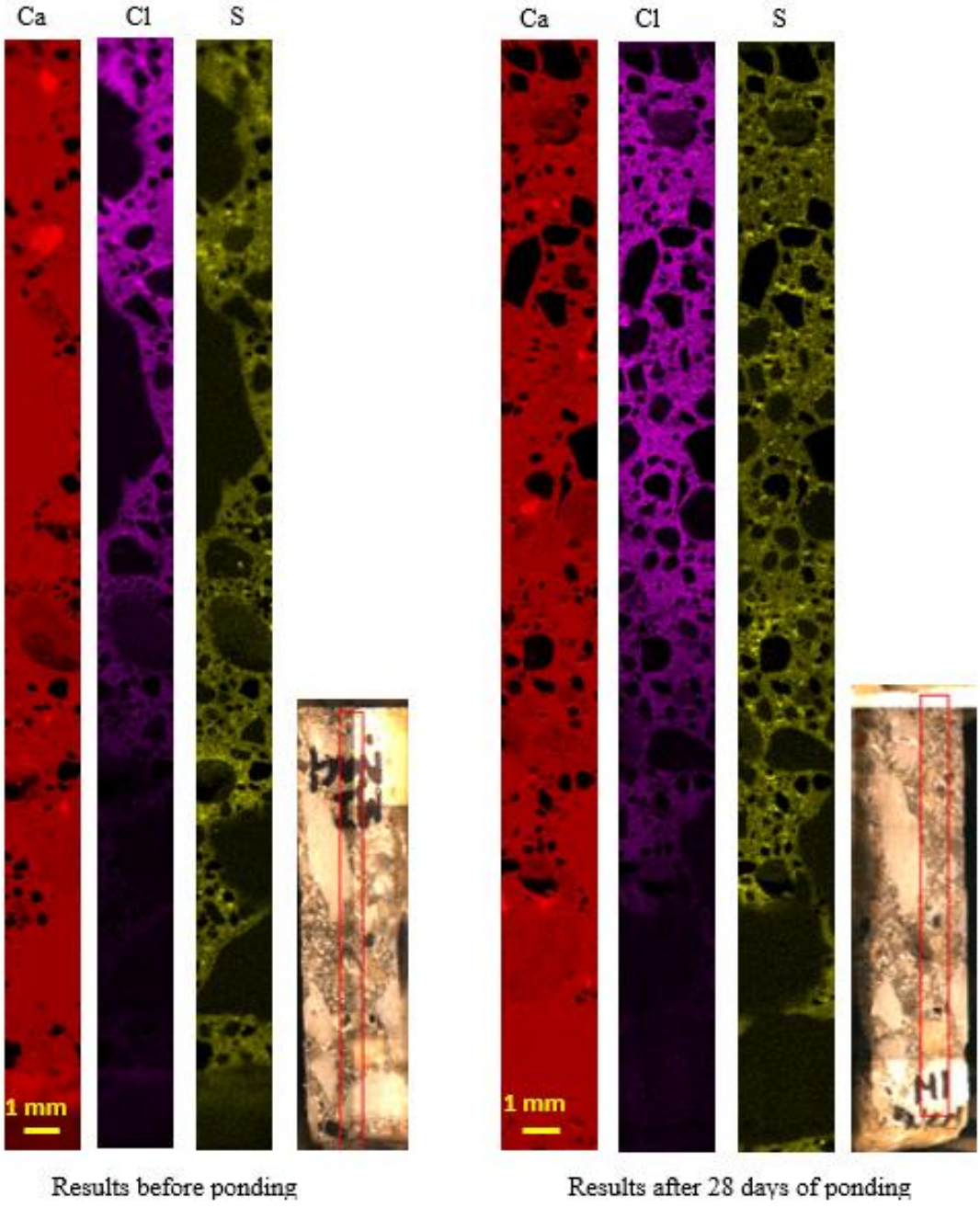

(b)

Figure 3-4.Ap. µXRF results of CSA2B-M field samples a) the first measurement b) the second measurement

Figure 3-5.Ap. µXRF results of CSA2B-W field sample (The second sample was broken during the polishing)

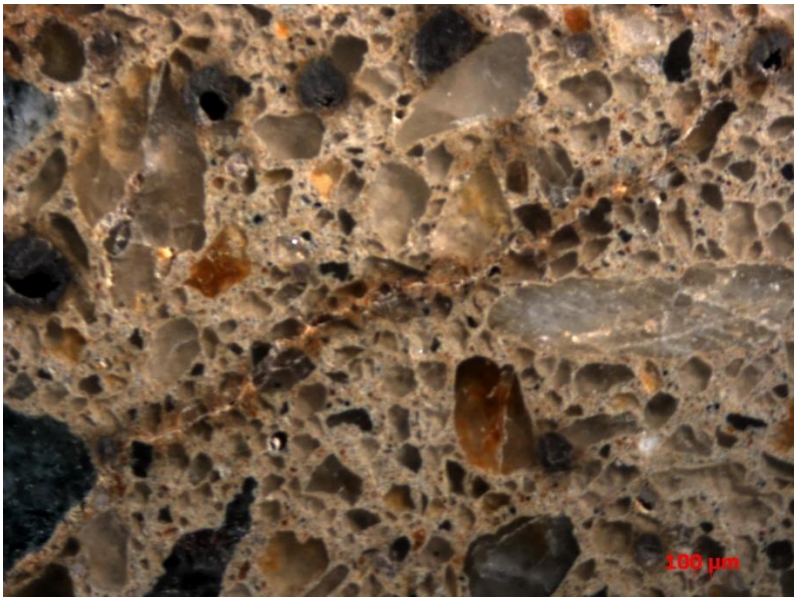

Figure 3-6.Ap. Crack detected in the first measurement of AA1 field sample

CHAPTER IV

USING MEDICAL X-RAY MACHINES TO DETERMINE THE SERVICE LIFE OF CONCRETE

Abstract

The durability of concrete may be defined as the ability of concrete to maintain serviceability within a specific environment due to issues such as corrosion, freeze-thaw, sulfate attack, and physical abrasion. Many researchers have developed and used a variety of test methods and equipment to study multiple aspects of concrete durability. This study aims to investigate the feasibility of using a medical x-ray device to measure the penetration of a tracer within the concrete. These measurements can be used to calculate the diffusion coefficient (D_c) of the concrete. The D_c can be used in a computer model to predict the service life of a concrete structure. The results from the new testing device are compared to the results from other established equipment. The results show that using a medical x-ray device can generate reliable and accurate results similar to the transmission x-ray microscopy (TXM) method. The average percent difference between the two

methods is 1.02% with a maximum difference of nearly 17%. Also, compared to TXM, a medical x-ray device is more economical and requires less time to complete the test.

Keywords: Dental x-ray, transmission x-ray microscopy, Durability, Corrosion, Concrete, Chloride penetration

4.1.Introduction

Concrete has been used for over a century as the building material of choice for a long service life. One concern with concrete is deterioration from the corrosion of embedded reinforcing, freeze-thaw, sulfate attack, physical abrasion, carbonation, and alkali-silica reaction (ASR) [1, 2]. Because of the importance and significant investment of concrete structures predicting the service life of concrete has been a major goal. Currently, many test methods are used to try and measure the properties of concrete and then determine the durability of the concrete.

Generally, the durability of concrete is governed by the resistance of concrete to the transport of outside ions [3]. The mass transport mechanisms for many durability issues are due to ion diffusion into the concrete as a key component to corrode the steel reinforcement [4]. The most widely used method to investigate ion ingress into cement-based materials is the bulk diffusion test. This test is completed by ponding a salt solution on top of the sample described in ASTM C 1556 and AASHTO T259 followed by a titration test from materials at different depths as described in ASTM C 1152 and AASHTO T260 [5–8]. However, this technique is destructive and requires that a significant mass of powder be collected from a number of different depths of the concrete. The measurement is an average of all of the material collected. The test is also time consuming and labor intensive.

The ASTM C1202, or the rapid chloride permeability test (RCPT), is another common test to assess concrete's ability to evaluate the ability for chloride ions to penetrate into concrete. This test

monitors the electrical current passed through a water-saturated concrete specimen subjected to 60 V of direct current for 6 hours [9]. The current measured in the RCPT is related to all the ions in the pore solution and not just the chloride ions [10]. This can cause a false estimate of the concrete chloride ion diffusion when supplementary cementing materials, certain chemical admixtures, or steel fibers are used [9,11,12]. Additional challenges with this test can be found in other publications [9,11–14]. The concrete resistivity test (AASHTO TP95 and ASTM C 1760) is another common test measuring the electrical resistance of the concrete [15,16]. The resistivity test is similar to the RCPT test, but it requires less effort to complete the test. The test measures the resistance against the flow of a fixed electrical current [17]. This test has been shown to give equivalent results to RCPT when the samples are conditioned correctly. Unfortunately, like RCPT, the resistivity test has the same disadvantages plus issues with conditioning the sample including temperature, moisture content, amount of surface carbonation and the impact of some aggregate [17–20].

Several studies have used x-ray imaging techniques to investigate concrete durability [1, 9–21]. Most of this equipment is expensive, time-consuming, and needs significant sample preparation. Recently, Transmission X-ray microscopy (TXM) have been used to learn more about moisture movement in cement-based materials. This technique is non-destructive, fast, requires minimal sample preparation, and the technique can image at a spatial resolution of 200 nm to 20 μm [33]. TXM can be considered a non-destructive technique due to the X-ray image not destroying the sample and being able to use the same sample in another experiment. One drawback of the TXM imaging is that it requires a high energy source that is typically costly. This reduces the availability of the TXM method. The goal of this study is to develop the CHIP (Checking Ion Penetration) method which uses a medical x-ray source and works similar to TXM to investigate mass transport within cement-based materials as a faster and less expensive test method than TXM.

4.2. Overview of experiment program

This study is divided into two parts. The first will focus on establishing the validity of the CHIP and the second will highlight the variability of the method. In the first part, the results of CHIP are compared with TXM. TXM is an already established and reliable x-ray imaging technique to study mass transport into concrete [33–38]. Further, TXM and CHIP are similar that they both image tracers penetrating into concrete samples. The primary difference between them is the equipment used to do the imaging.

In the first part, paste and concrete samples were tested. In total, 81 paste samples with different w/c ratios were made and cured for 28 days (27 samples per each w/c). Eight samples of the prepared samples for each group of w/c were tested with both TXM and CHIIP and 81 samples were tested only with CHIP. The concrete samples were cored from different field samples. Samples were prepared for the test and scanned with TXM and CHIP to get the initial images before starting the test by ponding the samples with a salt solution tracer as explained in detail within section 4.3.2. After capturing the initial image without any tracer, the samples were ponded with the 0.6 mol/lit potassium iodide (KI) tracer for 14 days. Since both methods are NDT techniques, the same samples were used in both imaging techniques to compare the results. After 14 days of ponding, the same samples were scanned again with both TXM and CHIP techniques. Then the captured raw images called radiographs were analyzed according to the approach explained in section 4.3.5 to get concentration profiles. Next, the concentration profile from each sample was compared using both techniques. Finally, a study was conducted on the concrete samples to investigate the reliability of CHIP. In that section, reproducibility, repeatability of the method along with the impact of scan direction are investigated. Each step of the experiment is explained in detail later in the relevant sections.

4.3. Methods

4.3.1. Sample preparation

4.3.1.1. Materials

For making paste samples ordinary ASTM C150 Type I Portland cement [39] was used. The chemical composition of the cement is shown in Table 4-1. Tap water at room temperature was used during the mixing. No chemical admixtures or secondary cementitious material were used in these samples.

Table 4-1. Chemical composition of cement with bulk XRF (% weight)

SiO_2	Al_2O_3	Fe_2O_3	CaO	MgO	SO_3	K_2O	Na_2O	P_2O_5	TiO_2	Mn_2O_3	SrO	ZnO	Cr_2O_3	LOI
17.39	4.87	4.71	65.15	1.40	2.51	0.48	0.46	0.13	0.39	0.11	0.15	0.03	0.09	2.12

4.3.1.2. Mixture proportion and mixing

Mixture proportions of both the paste and mortar samples are provided in Table 4-2. The paste samples investigated had three different water-to-cement ratios (w/c) of 0.35, 0.40, and 0.45. Different w/c were chosen to get samples with different permeability in order to examine the accuracy of the CHIP results for fluid transport within the cementitious materials with different properties. The raw components were mixed according to ASTM C305 [40].

Table 4-2. Mixture proportions

Mixture	Cement (g)	Water (g)
Paste (w/c=0.35)	891	312
Paste (w/c=0.40)	891	354
Paste (w/c=0.45)	891	401

4.3.1.3. Sample Preparation

4.3.1.3.1. Paste samples

Cylindrical micro vials with an inside dimension of 9.5 mm × 46 mm were used as a mold to cast samples as shown in Figure 4-1. Vials were partially filled within 5 mm of the top to provide a space for ponding solution on top of the sample. Large air voids in each sample mixture were removed from the samples by physically rodding with a 1.45 mm wire. The consolidation was considered to be finished when all visible large air voids were removed from the samples. Three samples were made from each mixture. Then, the plastic lids of the vials were closed. The sealed samples were then transferred into a covered box in a 23°C moist curing room for 28 days. The moisture room used for curing the samples meets the requirements of ASTM C511 [41].

After curing, a metal hexagonal nut was attached to the bottom of the samples. This nut was matched with the magnetic hexagonal stage to load the samples consistently in the x-ray machine. The stage and sample are shown in Figure 4-2. The hose clamp shown in Figure 4-1 was used to prevent the movement of the applied solution between the walls of the sample holder and the sample. This ensured that the only penetration into the sample will come from the surface or a one-directional penetration.

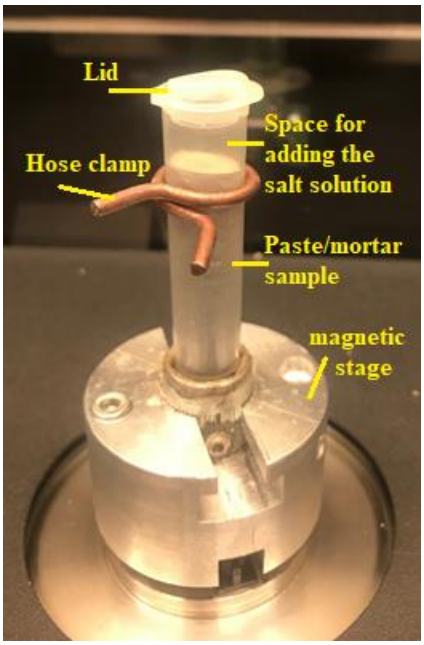

Figure 4-1. Sample figuration loaded in TXM machine

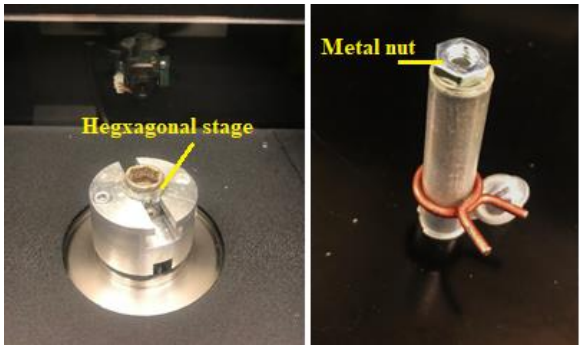

Figure 4-2. Samples are loaded stage by gluing a nut at the bottom

4.3.1.3.2. Concrete samples

To investigate the CHIP on concrete samples, ten field samples collected from in-service bridge decks were taken cores with 19.05 mm (3/4 in) in diameter. Then all sides of the samples except the finished surface were covered with a hydrophobic wax to have one-dimensional diffusion. Next, a PVC nut was glued at the bottom of each sample as shown in Figure 4-3.

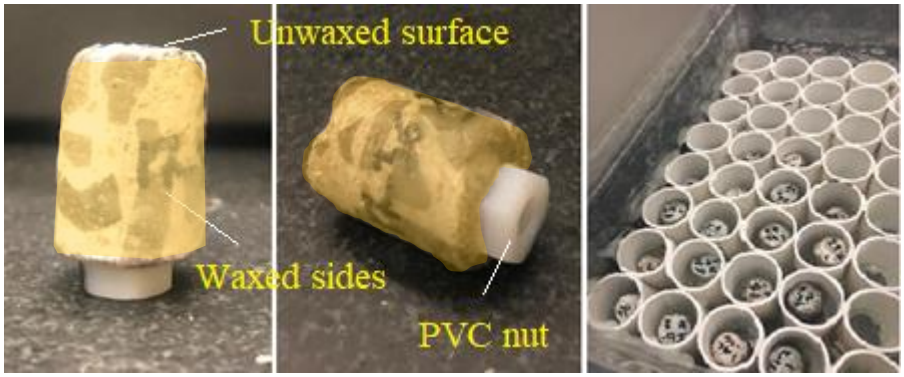

(a) (b) (c)

Figure 4-3. Sample figuration in the case study (a) Waxed sample, (b) A PVC nut is glued, and (c) Samples submerged in the KI solution

4.3.2. Diffusion test

Diffusion is the movement of a substance from an area of high concentration to an area of low concentration. The diffusion test in this study refers to applying a 0.6 mol/L or 10% KI tracer salt solution. The KI concentration was chosen to obtain satisfactory contrast in the TXM technique [33]. Since both CHIP and TXM can image materials with high electron density then they can

observe the iodide from the KI salt as it penetrates the concrete. Fortunately, iodide and chloride ions are similar in size (iodide radius is 206 pm versus a chloride radius of 167 pm). Also, the previous testing has shown that iodide gives diffusion coefficients 24% higher than chloride [33]. This means that iodide penetration can provide important insights into the ability of cementitious materials to resist ion penetration.

Before starting the test, samples were scanned with both CHIP and TXM to get the initial images of the original samples called reference radiographs. To start the diffusion test, 0.15 g of solution was used to cover the surface of paste samples with 2 mm of solution for 14 days. For concrete samples, the solution filled the space between the sample and cell walls to reach 2 mm above the sample surface. In this period, the KI solution was refreshed every five days to keep the concentration constant. During the experiment, the lids of all vials were sealed to prevent any evaporation and change in the solution concentration. All samples were kept at room temperature (23 ^{o}C) during the experiment. After 14 days of ponding, the same samples were scanned with both CHIP and TXM from the same orientation to get the secondary radiographs.

When a solution with high electron density penetrates a sample, the penetrated depths in the secondary radiographs look different in comparison to the reference radiograph. By comparing the secondary radiograph of each sample with its reference radiograph quantitative concentration profiles and penetration depths of the solution can be found. With this information, the concentration profile can be obtained. From this concentration profile then the diffusion coefficient and surface concentration can be obtained. These are engineering parameters that combine the impacts of fluid transport mechanisms of diffusion, absorption, convection, and chemical binding in one term. This work compares the results from CHIP and TXM by investigating the same samples in both techniques. This provides a quantitative way to compare the methods.

4.3.3. X-ray imaging techniques

4.3.3.1. TXM method

A laboratory Skyscan 1172 μCT scanner was used to conduct the experiment. In this machine, each sample was loaded on a fixed stage between the x-ray source and the detector as shown in Figure 4-4. When x-rays are used to investigate the sample, some x-rays are absorbed, and others pass the sample to reach the detector. The detector produces grayscale images called radiographs based on the received x-rays. The schematic view of the mechanism of imaging in this method is shown in Figure 4-5. Radiographs were grayscale images in which each pixel has a gray value between "0" and "255". Pure black has a gray value of "0" and pure white has a gray value of "255". The gray values change by density, thickness, chemistry, or a combination of these. Denser or thicker materials absorb more x-rays and are therefore darker in the TXM radiographs. Air absorbs less x-ray and has been commonly displayed as light gray in the background of each radiograph. As the KI solution penetrates into the sample, the penetrated depths are subjected to gray value change such that the affected regions become darker, and therefore gray values decrease compared to the reference radiograph.

Since each radiograph should be compared with its reference radiograph, it is necessary to get radiographs from identical orientations at each interval of scanning. This identical orientation is obtained by using the stage shown in Figure 4-2. This stage allowed a constant orientation to be used. This constant orientation becomes critical when concrete samples are investigated because of the inclusion of the larger aggregates.

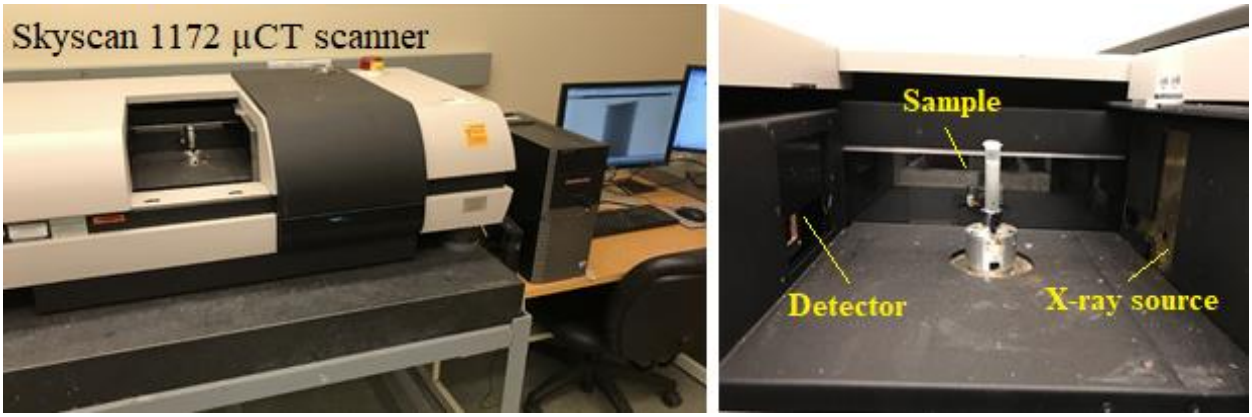

(a) (b)

Figure 4-4. (a) laboratory Skyscan 1172 µCT scanner and (b) sample loaded in the x-ray scanner

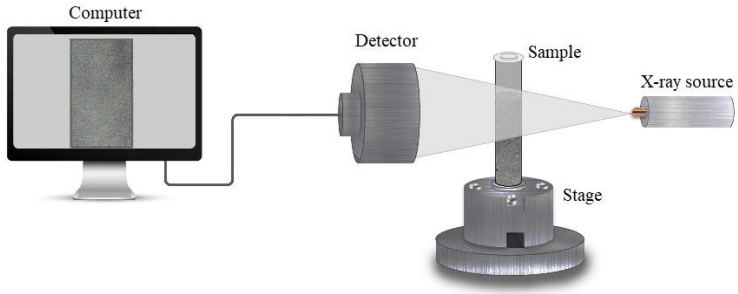

Figure 4-5. Schematic view of the mechanism of imaging in TXM method

4.3.3.2. *CHIP method*

This method was very similar to the TXM. The only differences were the x-ray source and x-ray settings. An overview of this method is shown in Figure 4-6 and the prototype equipment is shown in Figure 4-7. More details can be found in the Appendix. Like TXM, captured radiographs are grayscale images in which each pixel has a value between "0" and "255". Contrary to TXM, in the CHIP method, 255 represents white regions which correspond to a maximum density. On the other hand, zero value represents black spots as a minimum density such as air in the background of each radiograph. Like TXM, to investigate the gray value change in each sample over time, it is

necessary to take images at a constant orientation at each measurement. The same test setup as shown in Figure 4-2 was used with the CHIP to obtain consistent orientations for each image.

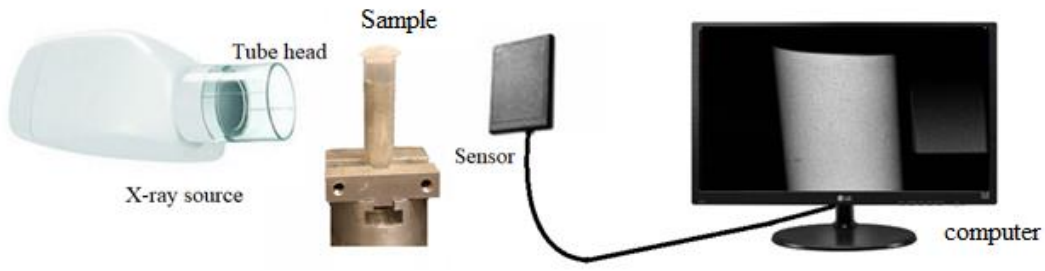

Figure 4-6. Schematic view of dental x-ray imaging technique setup

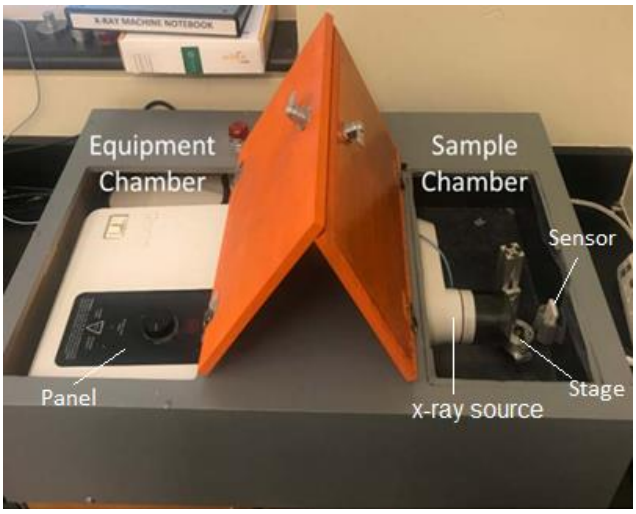

Figure 4-7. Figuration of the finished CHIP prototype

4.3.4. Data collection in both CHIP and TXM methods

All samples were scanned before applying the solution with both TXM and CHIP to measure the initial gray values for each sample. This image was called a reference radiograph. The elevation used for each sample was recorded to use the same height for taking consistent images at the next imaging time.

To compare the results of CHIP with TXM, the same side of each sample scanned in TXM was scanned in CHIP. After 14 days of applying the 0.6 mol/L KI solution on top of the sample, the

second radiograph was taken. Before taking the second radiograph of paste samples, the solution in the vial was poured off, the remaining solution was removed by a paper towel, and then the hose clamp was removed. Before taking the second radiograph of concrete samples, samples were pulled out from the solution and then dried off by a paper towel. All the settings used in TXM and CHIP techniques are summarized in Table 4-3.

To evaluate the repeatability of the CHIP method and to measure the single-operator apparatus precision, each concrete sample was loaded, scanned, and unloaded. This was repeated three times for each sample.

To determine the impact for the direction of scanning on diffusion results, each sample was scanned from angles of 0˚, 60˚, and 120˚ and the results were compared.

Table 4-3. Settings used in TXM and CHIP imaging techniques

Parameter	TXM	CHIP
Pixel size (μm)	8.97	15
Voltage (KeV)	100	120
Current (μA)	100	7000
Filter	0.5 mm Al +Cu	1.5 mm Al*
Exposure time (s)	8.25	8

*No Additional filter was used. The dental x-ray head had an inherent 1.5 mm Al filter.

4.3.5. Data analyzing of both imaging techniques

To be able to compare the images from the two methods, the CHIP images had to be transformed to match the gray value range of the TXM method. To do this a software programming code [42] was prepared to import each image, process the image, and write the output image in BMP format. Eq. (4-1) was used in the programming code to normalize the gray values in the raw image of CHIP and transform the gray values range of CHIP to the gray values range of TXM.

$$GV_i = \frac{GV_d - \mathrm{Min}}{\mathrm{Max} - \mathrm{Min}} \qquad \text{Eq. (4-1)}$$

Where GV_i is the gray value of the processed image. GV_d is the gray value of each pixel in the raw CHIP radiograph. Max and min are the maximum and minimum gray values in the captured radiographs, respectively. In this study, the Max and Min gray values were equal to 4500 and 75, respectively. The reason for having Max and Min values different from the ultimate Max and Min values (6500 and 0) is that in the captured radiographs there was not any pure black or pure white.

To analyze the radiographs, a software programming code [42] with minimal user intervention was prepared to align the images taken after 14 days of ponding with the reference image for each sample. Alignment of the radiographs means applying local displacements (i.e. shifting and rotating) to the secondary radiograph of one individual sample in a way to have it projected on the reference radiograph. Then, to get the average of gray values at each depth for each sample, the central region of each radiograph with a width of 0.88 mm (approximately 100 pixels in TXM radiographs and 60 pixels in CHIP radiographs) as shown in Figure 4-8(a) was used in the analysis. This was done to eliminate edge effects called cupping artifacts [43]. Each line shows the location where the gray value was measured over the depth of the sample. The final gray value profile was an average of all gray value profiles obtained from the considered 100 or 60 lines as shown in Figure 4-8(b). One limitation of this method is that the measurement will focus on the center of the sample. This means that if the sample is not homogeneous then the results will be different for different angles. This will be discussed further for the concrete investigations.

Eq. (4-2) shows the attenuation ($\Delta\mu$) was calculated according to the Beer-Lambert Law [18, 27, 28]

$$(\Delta\mu)x = \ln (I_{ref})x - \ln (I_t)x \qquad \text{Eq. (4-2)}$$

where $(I_{ref})x$ is the transmitted x-ray intensity (gray value) at each depth (x) in the radiograph captured before applying the tracer and $(I_t)x$ is the transmitted x-ray intensity at the same depth after the sample has been ponded with iodide. To convert the calculated attenuations to

concentration, calibration curves were applied. More detail on the calibration curves is provided in the appendix.

Next, the concentration profiles were fitted by Fick's second law of diffusion as expressed in Eq. (4-3). By fitting a curve on each concentration profile, diffusion coefficient (D_c) and surface concentration (C_s) can be found for each sample. The D_c obtained combines the impact of fluid transport mechanisms of diffusion, absorption, convection, and chemical binding in one term. For this reason, the diffusion coefficient obtained from the observation of the applied technique in this study provides a more realistic insight into the fluid transport into the concrete.

$$C_{(x,t)} = C_s\left(1 - \mathrm{erf}\left(\frac{x}{2\sqrt{D_c t}}\right)\right) \quad C_{(x,0)} = 0 \quad x > 0, \quad C_{(0,t)} = C_s \quad t \geq 0 \qquad \text{Eq. (4-3)}$$

Where x is the distance from sample surface; t denotes time; D_c is diffusion coefficient; C_s is surface iodide concentration; C(x,t) represents iodide concentration at the depth of x from the surface after time t; and erf is the error function.

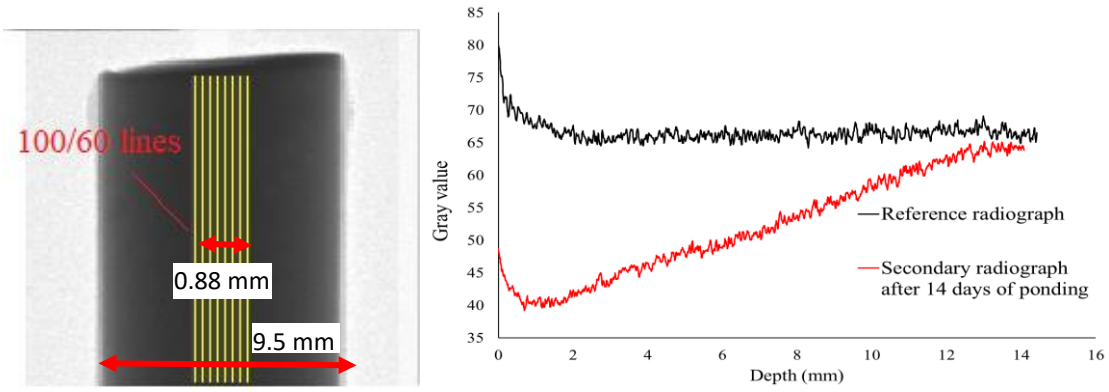

(a) (b)

Figure 4- 8. (a) radiograph with a considered region in data analyzing and (b) averaged gray value profiles

4.3.6. Analysis of variance (ANOVA)

For paste samples, w/c of 0.35, 0.4, and 0.45 were made. For each w/c, 27 paste samples were prepared. An analysis of variance (ANOVA) was completed to determine if the experimental results for different w/c ratios are statistically different. In this study, there are two variables of D_c and w/c. The w/c is considered as an independent variable and the D_c is considered as the dependent variable. The null hypothesis was determined as "there is not a significant difference between the mean of D_c for each w/c" and the alternative hypothesis was defined as "there is a difference between the mean of D_c for one of the w/c compared to the other w/c". This work uses a 5% significant level or a P-value <0.05 to reject the null hypothesis.

4.4. Results and discussions

4.4.1. Comparing TXM and CHIP

To show the repeatability of the two methods, Figure 4-9 shows the concentration profiles of the paste samples with different w/c after 14 days of ponding. The TXM results are shown with a solid line and CHIP results are shown with a dashed line. Figure 4-9 shows the ability of both the TXM and CHIP to measure the movement of ions at different w/c ratios. As the w/c increases, the highest concentration and penetration depth increased as well. Both TXM and CHIP methods can be used to study the importance of other parameters affecting the mass transport properties of the cement-based materials. The average difference in the measurements is 2.74% and the maximum difference is 8.6%. This indicates that there is a good agreement between CHIP and TXM for paste samples. One thing to note is that the CHIP measurement only takes the 20 sec compared to the 60 sec for the TXM. This could be helpful when running a large number of samples. Moreover, in the CHIP method, more depth was observable in each radiograph. The variability investigations of the CHIP are conducted on the concrete samples in section 4.4.2.

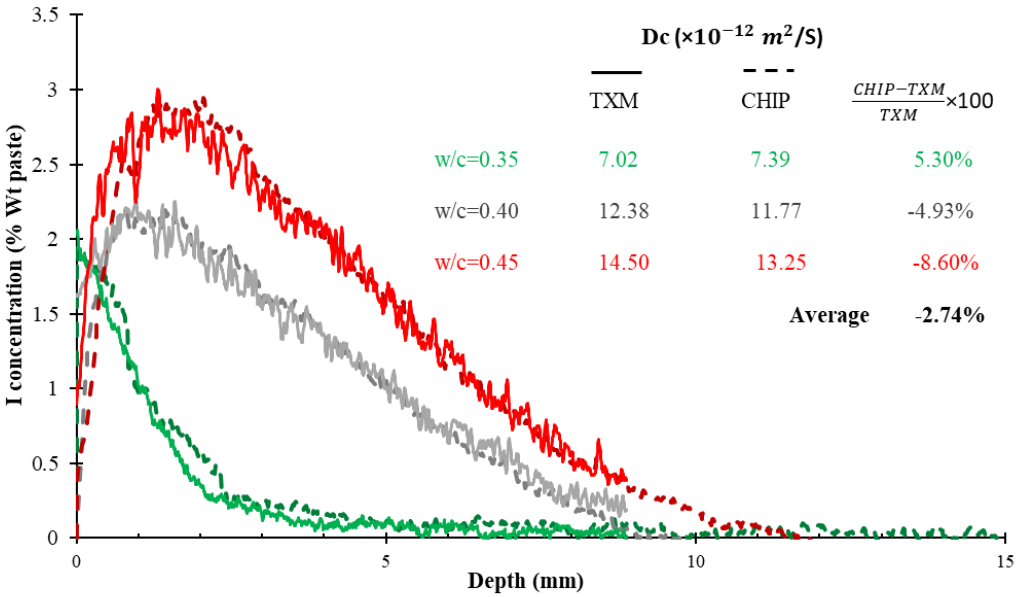

Figure 4-9. Comparing the TXM and CHIP results for paste samples with different w/c ratios

Figure 4-10 shows the concentration profiles of two concrete samples. In Figure 4-10 TXM results are shown with a solid line and CHIP results are shown with a dashed line. The same strong compatibility between CHIP and TXM was observed in the concrete samples with the maximum D_c variability of 15%. The higher amount of variability in the concrete samples may be caused by minor differences in the sample loading in the two x-ray machines.

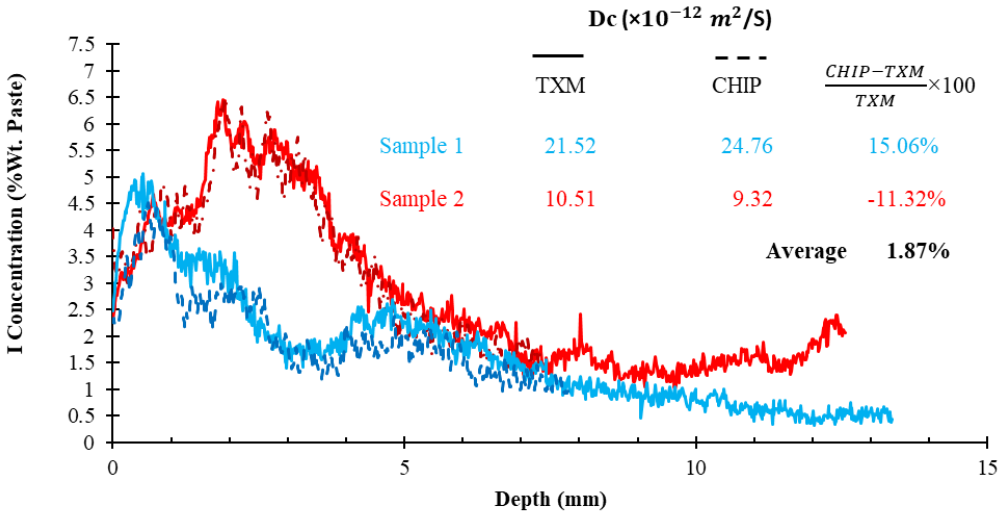

Figure 4-10. Comparison of TXM and CHIP concentration profiles for two different concrete samples

Figure 4-11 compares the diffusion coefficients of 24 paste and 12 concrete samples obtained from the two methods. The average percent difference of the measured D_c between the two measurement methods is -1.02% with a range between -16.9% and +14.8%. The 95% prediction intervals are shown with a blue dashed line in Figure 4-11. A 95% prediction interval is an estimate of the range where a future observation will fall with a 95% probability. For this data, all of the observations are within the 95% prediction interval. Linear regression was plotted with these observations in Figure 4-11. The slope of the linear regression line in Figure 4-11 is 0.986 which is close to the ideal slope of 1. This means that the results of the CHIP and TXM are comparable. There could be some differences in the measurement because of minor differences in the sample loading in the two x-ray machines.

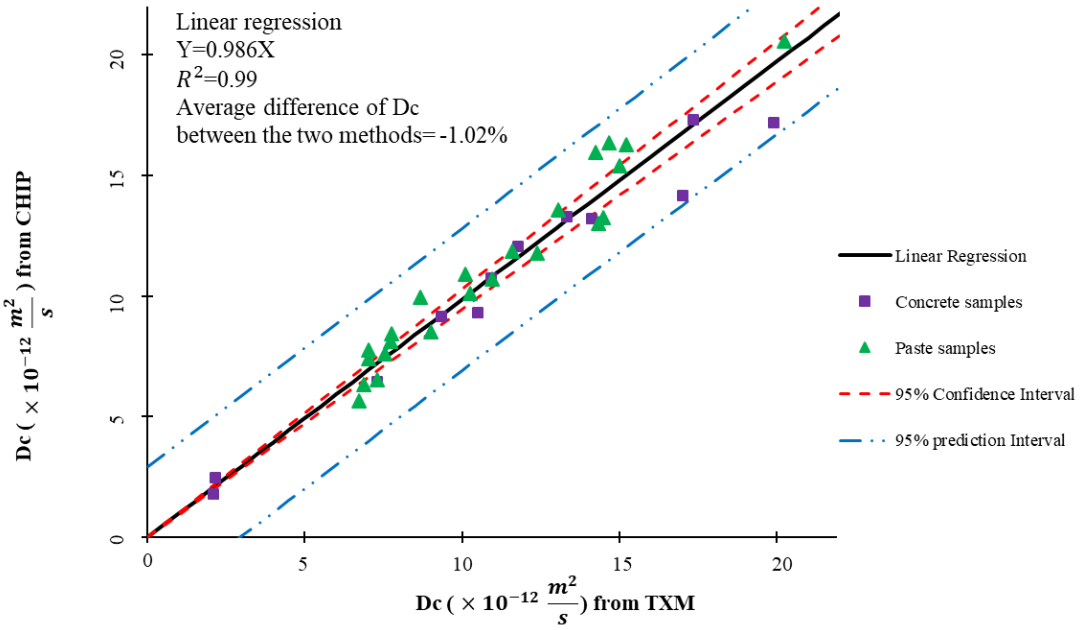

Figure 4-11. Comparison between TXM and CHIP diffusion coefficients for all tested samples

4.4.2. Variation of the CHIP method

Two approaches were considered to evaluate the variation of the CHIP. In the first approach, three cores were taken from the same concrete sample and all three cores were scanned from one direction. This approach examines the variation of cores taken to repeat measurements on a single sample. The results of this evaluation are shown in Figure 4-12. The CV and Std. values were equal to 24.2% and 3.498×10^{-12} m^2/s, respectively. The higher variability values of concrete samples compared to the paste samples reported in section 4.4.1 is due to the inhomogeneity nature of the concrete samples. This shows that repeat measurements of the same sample have some variation. The CV of 24.2% in CHIP is higher than the CV of 14.2% for a single laboratory repeatability of ASTM C 1556. In CHIP a small region in the center with a width of 0.88 mm is considered for analyzing to remove the impact of cupping artifact. Since concrete is a composite material, considering only a narrow strip in the center of each radiograph during data analysis may be impacted by variations in the aggregate found in the concrete samples. This means that different

samples will have a different distribution of paste and aggregates in the central region of each radiograph at each angle. This will have an impact on the results. For this reason, the authors suggest taking radiographs at different angles of a concrete sample, then calculate the D_c attributed to each angle and report the average D_c for each concrete sample. Another solution can be using cubic-cut samples instead of cored samples to eliminate cupping artifact and then consider a larger area for data analysis.

The discussion above brings up a concern about the importance of scan direction in CHIP. To determine the impact of the direction of scanning on diffusion results for concrete samples, each sample was scanned from angles of 0˚, 60˚, and 120˚. These results are shown in Figure 4-13. The reader must remember that only the center of 0.88 mm of each radiograph was analyzed. This means that these samples will have a different distribution of paste and aggregates in the central region of each radiograph at each angle. This will have an impact on the results. While the concentration profiles showed similar trends, the CV is 22.3%. This is similar to the CV found in Figure 4-13 for three different samples from the same concrete cylinder. This means that the variability from three different angles on the same sample is similar to the variability from three different samples from the same mixture.

One way to overcome this variability is to take radiographs from different angles and use the average concentration to calculate the D_c. Taking radiographs at different angles helps to get concentration profiles of a concrete sample from different angles. Each of these concentration profiles gives a D_c. Reporting the average D_c for each sample gives a more precise insight into the sample performance against fluid transport. Moreover, taking radiographs at different angles will help to identify possible anomalies in the sample.

To evaluate the repeatability of this method and to measure the single operator apparatus precision, each sample of the collected field samples was loaded, scanned, and unloaded. This was repeated

three times for each sample. The results of the repeatability check are shown in Figure 4-14. Figure 4-14 shows the strong repeatability of the experiment by a single user with CV equal to 1.7% and Std. of 3.3× 10^{-13} m^2/s. This shows that the CHIP can produce highly reproducible measurements of ion penetration.

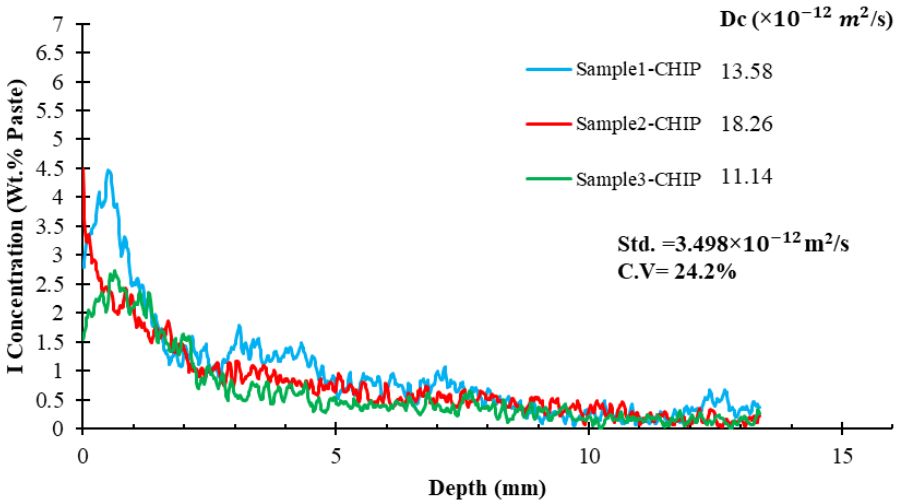

Figure 4-12. Variability of three concrete observations in CHIP method

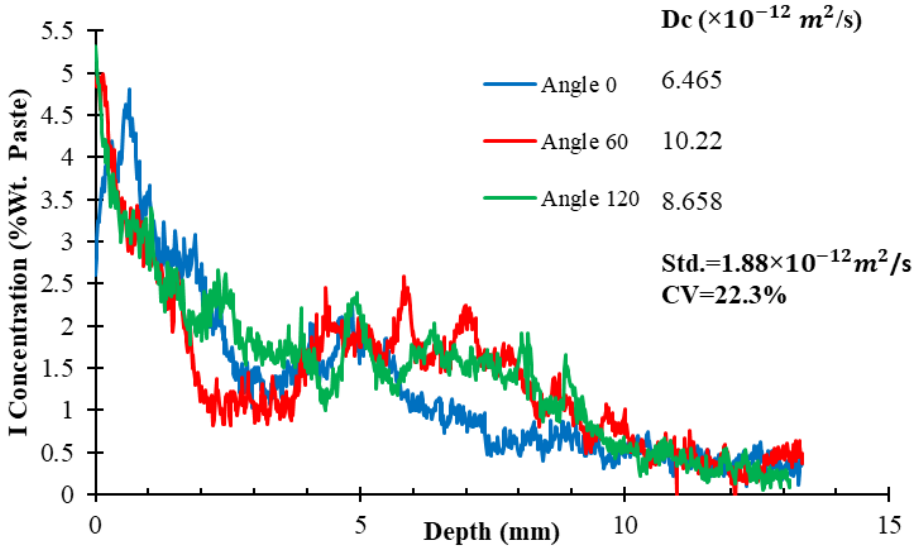

Figure 4-13. Concentration profiles of one concrete sample after scanning from three angles

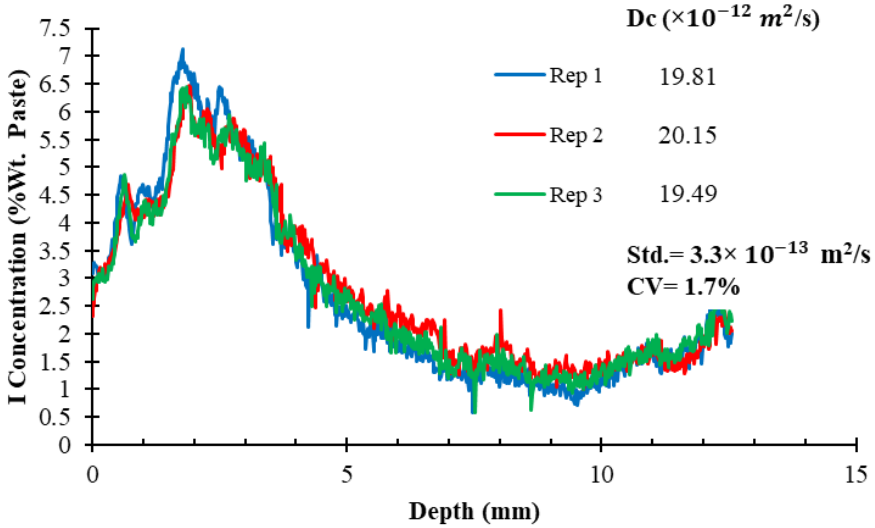

Figure 4-14. Concentration profiles of one concrete sample after scanning one side for three times

4.4.3. CV and ANOVA analysis of the CHIP samples at different w/cm

The coefficient of variance (CV) of the 27 samples per each w/c of 0.35, 0.4, and 0.45 were 11.3%. 12.1%, and 16.8%, respectively. The average CV and standard deviation (Std.) for the D_c were 13.4% and 1.38×10^{-12} m^2/s, respectively. The 95% confidence interval of CV for the paste samples in CHIP vary from 7.46% to 19.35% which shows that all three CV values are in this range and therefore the CV values are comparable between the groups.

Next, the results from the ANOVA is shown in Table 4-4. In this Study the P-value = 0.000.. This value is < 0.05 and therefore it shows that there is a significant difference between D_c of three groups with different w/c. In other words, the CHIP can determine the changes in the D_c of the paste samples changes by changing the w/c by 0.05. While the D_c values are significantly different between the groups of samples with the three tested w/c.

Table 4-4. Results of ANOVA analysis

	Sum of Squares	df	Mean Square	F	P-value	P-value<0.05
Between groups	33.11	2	16.55	8.93	.000	YES
Within groups	131.61	79	1.85			
Total	164.72	81				

4.5. Conclusion

This work establishes a new test method to determine the diffusion coefficient of ion penetration into concrete materials called Checking Ion Penetration (CHIP). This method is compared to Transmission X-ray Microscopy (TXM) to compare the two methods. This work establishes the CHIP as a reliable test method that can be used to evaluate the quality of concrete material samples. The following results can be concluded from this work:

1- The average variability between the diffusion coefficients (D_c) for paste and concrete from CHIP and TXM is 1.02%.

2- The average coefficient of variance (CV) and standard deviation (Std.) for the D_c values calculated for the all paste samples tested with CHIP is equal to 13.4% and 1.38×10^{-12} m^2/s, respectively. While the CV and Std. values for concrete is equal to 24.2% and 3.498×10^{-12} m^2/s, respectively. The higher variability values of the concrete samples compared to the paste samples is likely due to the inhomogeneity nature of the concrete samples.

3- The variability from three different angles on the same sample (CV≈ 22%) is similar to the variability from three different samples from the same mix (CV≈ 24%). One solution to

decrease the variability of CHIP is to scan a sample from different angles or use cubic-cut samples.

4- There is strong repeatability of the CHIP by a single user with CV equal to 1.7% and Std. of 3.3×10^{-13} m^2/s. This shows that the CHIP can produce highly reproducible measurements.

5- ANOVA analysis shows that the measured Dc values are statistically significant between a w/c of 0.35, 0.40, and 0.45. Also the CV of these measurents are all within a 95% confidence interval. This shows that the CV measurements are comparable.

These results show that the CHIP is a promising test method to rapidly evaluate the ion penetration of cementitious materials.

Acknowledgment

The authors acknowledge the financial support of NCHRP-IDEA Project 199 and the research oversight panel. The authors would like to thank Mr.Ali Hendi for giving valuable feedback and comments. Also, the author would like to thank Mr. Hadi Bolooki Pursaheli for assistance in providing schematic pictures.

References

[1] S. Lu, E.N. Landis, D.T. Keane, X-ray microtomographic studies of pore structure and permeability in Portland cement concrete, Materials and Structures. 39 (2006) 611–620.

[2] S.W. Tang, Y. Yao, C. Andrade, Z.J. Li, Recent durability studies on concrete structure,

Cement and Concrete Research. 78 (2015) 143–154.

[3] H. Hilsdorf, J. Kropp, Performance criteria for concrete durability, (1995).

[4] Y. Lu, E. Garboczi, D. Bentz, J. Davis, Modeling of Chloride Transport in Cracked Concrete: A 3-D Image–based Microstructure Simulation, Proceedings of the COMSOL Conference. (2012).

[5] ASTM C1556, Standard Test Method for Determining the Apparent Chloride Diffusion Coefficient of Cementitious Mixtures by Bulk Diffusion, (2016).

[6] AASHTO T 259, Resistance of Concrete to Chloride Ion Penetration, (1980).

[7] ASTM C1152, Standard Test Method for Acid-Soluble Chloride in Mortar and Concrete, (2012).

[8] AASHTO T260-94, Standard Method for Sampling and Testing for Chloride Ion in Concrete and Concrete Raw Materials, (1994).

[9] K.A. Riding, J.L. Poole, A.K. Schindler, M.C.G. Juenger, K.J. Folliard, Simplified concrete resistivity and rapid chloride permeability test method, ACI Materials Journal. 105 (2008) 390–394.

[10] K.D. Stanish, R.D. Hooton, M.D.A. Thomas, Testing the chloride penetration resistance of concrete: a literature review, Department of Civil Engineering, University of Toronto Toronto, Ontario, Canada, 2000.

[11] X. Shi, N. Xie, K. Fortune, J. Gong, Durability of steel reinforced concrete in chloride environments : An overview, Construction and Building Materials. 30 (2012) 125–138. doi:10.1016/j.conbuildmat.2011.12.038.

[12] R. Feldman, L.R. Prudencio Jr, G. Chan, Rapid chloride permeability test on blended

cement and other concretes: correlations between charge, initial current and conductivity, Construction and Building Materials. 13 (1999) 149–154.

[13] T.H. Wee, A.K. Suryavanshi, S.S. Tin, Evaluation of rapid chloride permeability test (RCPT) results for concrete containing mineral admixtures, Materials Journal. 97 (2000) 221–232.

[14] C. Shi, J.A. Stegemann, R.J. Caldwell, Effect of supplementary cementing materials on the specific conductivity of pore solution and its implications on the rapid chloride permeability test (AASHTO T277 and ASTM C1202) results, Materials Journal. 95 (1998) 389–394.

[15] AASHTO TP 95, Standard method of test for surface resistivity indication of concrete's ability to resist chloride ion penetration, American Association of State Highway and Transportation Officials, 2011.

[16] ASTM C1760, Standard test method for bulk electrical conductivity of hardened concrete, (2012).

[17] O. Sengul, Use of electrical resistivity as an indicator for durability, Construction and Building Materials. 73 (2014) 434–441. doi:https://doi.org/10.1016/j.conbuildmat.2014.09.077.

[18] R.B. Polder, Test methods for on site measurement of resistivity of concrete — a RILEM TC-154 technical recommendation, Construction and Building Materials. 15 (2001) 125–131. doi:https://doi.org/10.1016/S0950-0618(00)00061-1.

[19] H. Layssi, P. Ghods, A.R. Alizadeh, M. Salehi, Electrical resistivity of concrete, Concrete International. 37 (2015) 41–46.

[20] W. Elkey, E.J. Sellevold, Electrical resistivity of concrete, (1995).

[21] T. Yang, X. Yao, Z. Zhang, Quantification of chloride diffusion in fly ash–slag-based geopolymers by X-ray fluorescence (XRF), Construction and Building Materials. 69 (2014) 109–115.

[22] T. Danner, K. De Weerdt, M.R. Geiker, µ-XRF–Characterisation Of Chloride Ingress And Self-Healing In Cracked Concrete, In: Nordic Concrete Research, NORDIC CONCRETE RESEARCH. Proceedings of the XXIII Nordic Concrete Research Symposium. (2017).

[23] A. du Plessis, B.J. Olawuyi, W.P. Boshoff, S.G. le Roux, Simple and fast porosity analysis of concrete using X-ray computed tomography, Materials and Structures. 49 (2016) 553–562.

[24] N. Burlion, D. Bernard, D. Chen, X-ray microtomography: Application to microstructure analysis of a cementitious material during leaching process, Cement and Concrete Research. 36 (2006) 346–357.

[25] D.P. Bentz, N.S. Martys, P. Stutzman, M.S. Levenson, E.J. Garboczi, J. Dunsmuir, L.M. Schwartz, X-Ray Microtomography of an Astm C109 Mortar Exposed to Sulfate Attack, MRS Proceedings. 370 (1994) 77.

[26] A. Delagrave, J. Marchand, J.-P. Ollivier, S. Julien, K. Hazrati, Chloride binding capacity of various hydrated cement paste systems, Advanced Cement Based Materials. 6 (1997) 28–35.

[27] S.R. Stock, N.K. Naik, A.P. Wilkinson, K.E. Kurtis, X-ray microtomography (microCT) of the progression of sulfate attack of cement paste, Cement and Concrete Research. 32 (2002) 1673–1675.

[28] E. Gallucci, K. Scrivener, A. Groso, M. Stampanoni, G. Margaritondo, 3D experimental investigation of the microstructure of cement pastes using synchrotron X-ray microtomography (μCT), Cement and Concrete Research. 37 (2007) 360–368.

[29] E. Proverbio, F. Carassiti, Evaluation of chloride content in concrete by X-ray fluorescence, Cement and Concrete Research. 27 (1997) 1213–1223.

[30] V.C. Tidwell, L.C. Meigs, T. Christian-Frear, C.M. Boney, Effects of spatially heterogeneous porosity on matrix diffusion as investigated by X-ray absorption imaging, Journal of Contaminant Hydrology. 42 (2000) 285–302.

[31] M. Khanzadeh Moradllo, B. Sudbrink, Q. Hu, M. Aboustait, B. Tabb, M.T. Ley, J.M. Davis, Using micro X-ray fluorescence to image chloride profiles in concrete, Cement and Concrete Research. 92 (2017) 128–141.

[32] S. Khatibmasjedi, Insights Into the Mechanisms of Salt Scaling of High Volume Fly Ash Concrete, (2014).

[33] M. Khanzadeh Moradllo, Q. Hu, M.T. Ley, Using X-ray imaging to investigate in-situ ion diffusion in cementitious materials, Construction and Building Materials. 136 (2017) 88–98.

[34] A. Michel, B.J. Pease, M.R. Geiker, H. Stang, J.F. Olesen, Monitoring reinforcement corrosion and corrosion-induced cracking using non-destructive x-ray attenuation measurements, Cement and Concrete Research. 41 (2011) 1085–1094. doi:https://doi.org/10.1016/j.cemconres.2011.06.006.

[35] D.P. Bentz, K.K. Hansen, Preliminary observations of water movement in cement pastes during curing using X-ray absorption, Cement and Concrete Research. 30 (2000) 1157–1168. doi:https://doi.org/10.1016/S0008-8846(00)00273-8.

[36] S. Roels, T. van Besien, J. Carmeliet, M. Wevers, X-ray attenuation technique for the analysis of moisture flow in porous building materials, Second International Conference on Research in Building Physics, J. Carmeliet, H. Hens, G. Vermeir (Eds.), AA Balkema Publishers, Lisse, (2003), pp. 151–157.

[37] S. Roels, J. Carmeliet, Analysis of moisture flow in porous materials using microfocus X-ray radiography, International Journal of Heat and Mass Transfer. 49 (2006) 4762–4772.

[38] B.J. Pease, G.A. Scheffler, H. Janssen, Monitoring moisture movements in building materials using X-ray attenuation: Influence of beam-hardening of polychromatic X-ray photon beams, Construction and Building Materials. 36 (2012) 419–429. doi:https://doi.org/10.1016/j.conbuildmat.2012.04.126.

[39] ASTM C150, Standard Specification for Portland Cement, (2019).

[40] ASTM C305, Standard Practice for Mechanical Mixing of Hydraulic Cement Pastes and Mortars of Plastic Consistency, (2006).

[41] ASTM C511, Standard Specification for Mixing Rooms, Moist Cabinets, Moist Rooms, and Water Storage Tanks Used in the Testing of Hydraulic Cements and Concretes, (2019).

[42] MATLAB (R2016a), version 9.0.0, (2016).

[43] J.F. Barrett, N. Keat, Artifacts in CT: recognition and avoidance, Radiographics. 24 (2004) 1679–1691.

[44] L. Kocsis, P. Herman, A. Eke, The modified Beer–Lambert law revisited, Physics in Medicine & Biology. 51 (2006) N91.

[45] L. Cavé, T. Al, Y. Xiang, P. Vilks, A technique for estimating one-dimensional diffusion

coefficients in low-permeability sedimentary rock using X-ray radiography: Comparison with through-diffusion measurements, Journal of Contaminant Hydrology. 103 (2009) 1–12.

APPENDICES

Appendix A. Calibration curve

Calibration curves help to convert attenuation values ($\Delta\mu$) to concentration values. To develop the calibration curves for both TXM and CHIP methods, standard samples with known iodide concentrations were made by adding different iodide concentrations to the mixtures during mixing. Then these samples were scanned and analyzed as stated in sections 4.3.3 to 4.3.5. After scanning the standard samples, the attenuation related to each concentration was extracted. Ultimately, a polynomial curve of order 2 was fitted on the obtained spots to get an equation that converts the attenuation to the concentration. Figure 4-1.Ap and Figure 4-2.Ap show the calibration curves obtained by the two methods for paste and mortar, respectively.

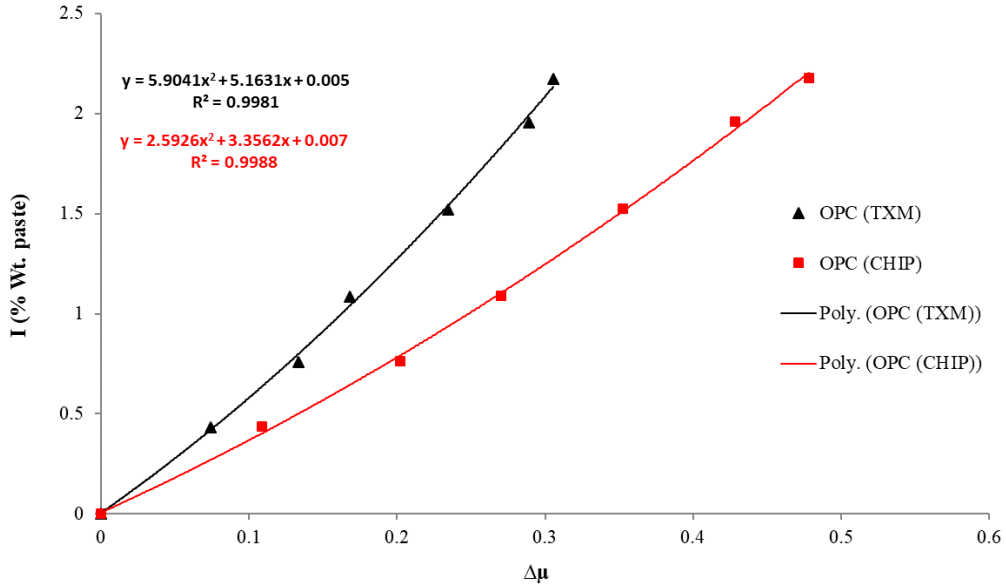

Figure 4-1.Ap. Calibration curve for paste (w/c=0.4)

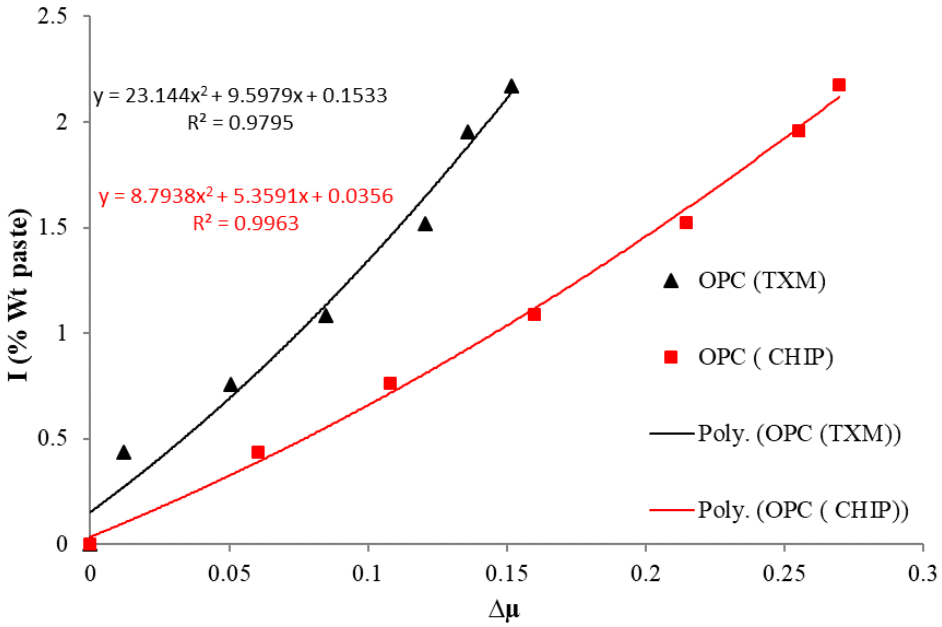

Figure 4-2.Ap. Calibration curves for mortar (w/c=0.4) used to calculate concentrations in concrete samples

CHAPTER V

IMPACT OF CURING TIME ON THE ION DIFFUSIVITY OF FLY ASH PASTES BY X-RAY IMAGING

Abstract

The rate at which deleterious ions penetrate into concrete dramatically influences the service life of the structure. The ion diffusion rate into concrete is dependent on the concrete quality. This chapter examines the impact of extending curing time on hardened paste samples made with seven different types of fly ash. For each mixture, 20% fly ash was used as a partial replacement of ordinary Portland cement by weight with curing times of 45, 90, and 135 days. The cured samples were then ponded with a 0.6 mol/L potassium iodide and by applying the CHIP (Checking Ion Penetration) technique, the movement of solution into the hardened pastes was monitored.

By analyzing the captured images, diffusion coefficient, surface concentration, and penetration depth of the mixtures were compared to each other. Results showed that extending the curing time from 45 days to 90 and 45 days to 135 days reduced the average diffusion rate by 26% and 50%,

respectively.

Keywords: Curing time, Fly ash, Ion diffusion, Dental x-ray imaging, Durability

5.1. Introduction

Corrosion of the embedded steel bars in reinforced concrete due to the penetration of deleterious ions similar to chloride is one of the main durability issues which results in damage or deterioration of the reinforced concrete structures. By assuming a continuous penetration of fluids containing destructive ions into the concrete at a constant temperature, the ingress rate of fluids depends on the microstructure of the concrete cover. Blending cement with fly ash regardless of its composition is known as a common practice to produce concrete with a dense microstructure to reduce the fluid transport into concrete [1–3].

Fly ash is a byproduct of coal combustion in the generation of electricity with the pozzolanic properties [4]. Fly ash particles react with the main cement hydration products i.e. calcium hydroxide in the paste matrix and produce secondary hydration products that strongly decrease concrete porosity [5]. Moreover, fly ash is used as a fine material to fill the pores in the hardened paste matrix after hydration [2]. In addition, using fly ash in a mixture results in a dense structure in the transition zone between aggregates and paste [6]. Therefore, blended cement with fly ash could be a solution to produce denser concretes with less susceptibility to harmful ions ingress [4].

There are a limited number of studies concerning the ingress of ions in concrete made of blended cement with fly ash [1,5,7–11]. Electrical migration [3,7,11] , electrical resistivity measurement [12,13], acid-soluble chloride [8,14], rapid chloride permeability [2,4,9,10], immersion in chloride solution using silver nitrate indicator[4] are the test methods used by researchers in the earlier studies. Most of the applied test methods are not a reliable indicator of ion diffusion into the blended binders because of the difference in the pore solution chemistry induced by using different fly ashes. In addition, some of the current test methods are time consuming and destructive.

Furthermore, most of the established test methods in the field of investigation of ion ingress into concrete cannot represent the exact multi-mechanistic transport of fluids into the concrete. In reality, harmful ions transport into concrete under different mechanisms like diffusion, absorption, permeation, electromigration, convection, and wicking [11,12]. Also, in most of the current test methods, chemical reactions between the diffused ions and cement (binding effect) are not considered. On the other hand, because of the difference in the nature of fly ash sources and their relative effectiveness and different curing times applied in different studies, there is not a consensus among the researchers on the potential of ion binding in cement-fly ash paste and concrete [9]. Moreover, the beneficial effects of fly ash on permeability and diffusivity tend to become more apparent with time.

This study investigates the impact of curing time on the ion diffusivity of blended cement pastes partially replaced with seven types of fly ash. This work uses an x-ray radiography technique called Checking Ion Penetration or CHIP to image the movement of fluids in blended cement pastes. This technique is rapid, nondestructive, and able to provide useful fundamental observations of ion movement in cement-based materials. Moreover, this technique takes into account the multi-mechanism of ion movement into a sample without applying any external force like an electric field to force ions to move. The authors believe that the results of the CHIP are a more direct method to measure the effective diffusion coefficient and the results obtained from this test can be used by modelers to predict the service life of the structures more precisely. More details on using CHIP in mass transport investigation can be found in Chapter IV. In this work, fluid transport studies were conducted on hydrated cement pastes to clarify the impact of each fly ash on the ion diffusion resistance by minimizing intervention from aggregates. In addition, the pore structure of the blended cement paste matrix is related to the ion diffusion in concrete.

5.2. Experiment methods

5.2.1. Materials

Ordinary ASTM C150 Type I Portland cement (OPC) [15] with the chemical composition shown in Table 5-1 was used to make cement paste samples. Seven types of commercially available fly ash provided from various coal sources, boiler designs, and collection conditions in the United States with the chemical compositions shown in Table 5-1 were used as well to make blended-cement paste samples. Fly ashes are classified into Class C and Class F according to ASTM C618 [16] recommendations. The fly ashes used in this work are distinguished from each other by assigning a unique code (C11 to IF1) as shown in Table 5-1. Tap water at room temperature was used for mixing.

Table 5-1. Chemical compositions of cement and fly ashes

Oxide	OPC	C11	IC1	IC2	IC3	IC4	F6	IF1
	N/A	Class C	Class C	Class C	Class C	Class C	Class F	Class F
SiO_2	17.39	30.96	31.82	25.15	29.66	29.85	51.87	58.33
Al_2O_3	4.87	20.77	22.87	21.20	21.03	17.66	25.71	21.87
Fe_2O_3	4.71	6.38	5.68	6.22	5.92	4.73	12.32	6.87
CaO	65.15	27.15	28.24	30.47	30.29	31.75	2.50	3.67
MgO	1.40	7.14	5.52	7.78	5.35	9.32	0.32	1.42
SO_3	2.51	1.59	1.08	1.04	1.87	1.19	0.67	0.59
Na_2O	0.46	3.45	2.28	4.02	2.22	2.57	1.61	2.17
K_2O	0.48	0.73	1.02	0.56	0.55	0.76	4.13	4.25
TiO_2	0.39	0.78	0.78	1.22	1.04	0.83	0.66	0.22
P_2O_5	0.13	0.83	0.46	2.18	1.61	1.08	0.05	0.36
SrO	0.15	0.23	0.25	0.15	0.46	0.24	0.16	0.24

5.2.2. Sample preparation

For all the considered mixtures, the water-to-binder ratio (w/b) was kept constant at 0.45. For each mixture, a 20% of fly ash was replaced by mass of cement (i.e. 80% Portland cement+20% fly ash).

Mixture proportions are given in Table 5-2. Mixing of materials was conducted per ASTM C 305 procedures [17]. In total seven mixtures were prepared for studying the considered seven types of fly ash.

Table 5-2. Mixture proportions

Mixture	Cement (g)	Water (g)	Fly ash (g)	w/b
80%OPC+20%Fly ash	711.1	400	177.8	0.45

Molds for casting cement paste samples were plastic transparent vials with dimensions of 9.5×46 mm. Vials were filed up within 5 mm of the top with the fresh paste as shown in Figure 5-1(a). Big air voids were taken off by physically rodding with a wire measuring 1.45 mm in diameter until no air voids with diameter > 0.25 mm were longer exist in the sample. For each mixture, four samples were prepared. After casting, the samples were sealed and packed tightly to keep them upright. Immediately after casting, the samples were transferred into a fog room while sealed with 23°C temperature for curing for 45, 90, and 135 days. The room used for curing the samples meets the requirements of ASTM C511[18]. After the curing was terminated, the samples were demolded by peeling off the plastic mold, and a hydrophobic wax was applied to all sides of the sample except the finished surface. Waxing was done to ensure having one-directional penetration from the finished surface towards the deeper depths of the samples. Then a hexagonal polyvinyl chloride (PVC) nut was attached to the bottom of the samples as shown in Figure 5-1(b). The attached nut helped to load each sample with the same orientation and direction in the x-ray machine to take consistent images at each interval of the experiment. More details are in the Appendix. A and Chapter IV.

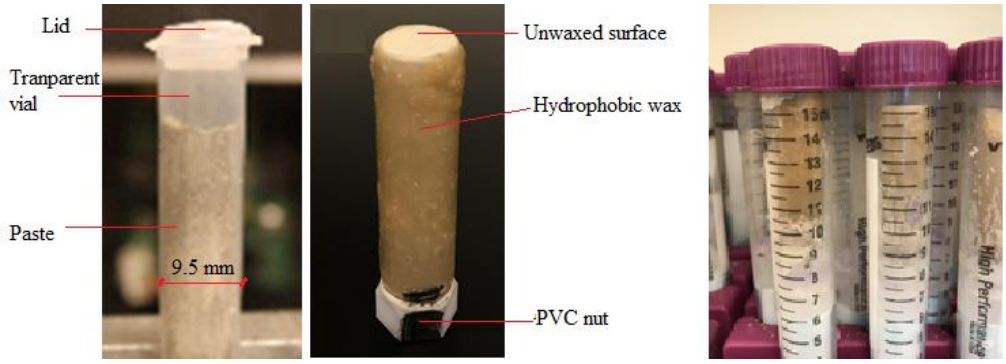

(a) (b) (c)

Figure 5-1. Sample figuration a) casted sample in the mold, b) demolded and waxed sample, and c) samples in the isolated tubes ready for ponding with 0.6 mol/L potassium iodide

5.2.3. Ion diffusion test method with the CHIP

CHIP is a non-destructive method that can project 3D information of a single sample on a 2D image, and therefore gives more information on the bulk sample compared to the test method suggested in ASTM C1556. This technique works similarly to the transmission x-ray microscopy (TXM). Each sample is loaded on a stage which is located between the x-ray source and the detector. By scanning each sample with CHIP, some parts of the emitted x-ray beams pass through the samples and to reach the detector, and as a result, a grayscale image called a radiograph is captured. Each pixel in the taken radiographs has a gray value between 0 and 255. The concept behind this technique is that when a tracer with high electron density penetrates into a sample, the penetrated depths are subjected to gray value change. To check the gray value change at different depths in this method, different radiographs of each sample taken at different ponding days are compared to the radiograph taken from the original sample. All samples were scanned before applying the tracer on top of them to have the initial gray values of each sample. This image was called a reference radiograph. After getting the reference radiograph, each sample was placed in a tube as shown in Figure 5-1(c). Next, samples were ponded with a solution containing a tracer. Then, by comparing the radiographs quantitatively as is explained in the Appendix. A, concentration profiles and penetration depth of the solution can be extracted; by having this

information, the diffusion coefficient, which combines fluid transport mechanisms of diffusion, absorption, and chemical binding in one term, can be calculated.

Since CHIP can capture materials with high electron density, potassium iodide (KI) was chosen to be used as the tracer. Iodide in the KI strongly absorbs x-ray waves due to its high electron density; also, iodide has a similar atomic diameter size and chemical properties to chloride. It has also been shown that the diffusion profiles for iodide and chloride in paste were quite comparable [19,20]. Also, the CHIP shows comparable results to results from TXM; moreover, the coefficient variance (CV) with the CHIP is 25% for concrete samples. More details are provided in the appendix.

The 0.6 mol/L KI solution was kept on top of the samples for 28 days. In this period, the KI solution was changed every five days to keep the concentration constant. During the experiment, the lids of all vials were sealed to prevent any evaporation and change in the solution concentration. All samples were kept in a room temperature (23 ºC) during the experiment. After 28 days of ponding, samples were scanned again. By analyzing the radiographs before and after ponding using Fick's second law and some additional explanation discussed in the appendix, concentration profile, diffusion coefficient (D_c), surface concentration (C_s) for each sample could be obtained. Despite extensive research on threshold level value, no agreement among the values obtained is found. However, threshold chloride concentration values vary but are typically in the range of 0.05 to 0.1% by weight of concrete (0.4 to 0.8% by weight of cement) [21]. In this study for each concentration profile, a threshold level of 0.21% weight of paste (0.05% weight of concrete) is assumed.

5.2.4. Mass measurements for porosity and degree of saturation calculations

The porosity of each sample was determined by following the procedures of ASTM C642 [22] with some minor changes. For each investigation, three samples were taken to weigh their initial weights (W_i). Then, the samples were submerged in water in a vacuum chamber to reach a constant value (equilibrium condition with mass change less than 0.03%). This saturated surface dried (SSD) weight was recorded as (W_{sa}). Next, the suspended apparent mass of the saturated samples was measured and recorded as (W_{su}). Next, the samples were dried in an oven at 110 ºC until an equilibrium mass was achieved (W_d). Eq. (5-1) and Eq. (5-2) were used to calculate the porosity and degree of saturation (DoS).

$$\text{Porosity} = \frac{V\ voids}{Vtotal} = \frac{W_{sa} - W_d}{W_{sa} - W_{su}} \times 100 \qquad \text{Eq. (5-1)}$$

$$\text{DoS} = \frac{W_i - W_d}{W_{sa} - W_d} \times 100 \qquad \text{Eq. (5-2)}$$

5.3. Results and discussions

5.3.1. Ion diffusion testing of different fly ash sources

Figure 5-2 compares the iodide concentration profiles of the studied fly ashes cured for 45, 90, and 135 days. As the trend line of each concentration profile becomes flatter it implies a higher diffusion rate and as the trend follows a sharp slope, it signifies a lower diffusion coefficient (D_c). As shown in all of the concentration profiles shown in Figure 5-2, increasing the curing time resulted in profiles with a higher slope and so a lower D_c. Doubling the curing time period for Samples C11 and IC4 showed minor improvement in D_c while for the other five fly ashes considerable changes in D_c were observed. Extending the curing time from 45 days to 135 days showed significant improvements in all of the fly ash investigated. Fly ash is at least partially a pozzolanic material that needs time for the hydration products to form. Comparing all seven concentration profiles shown in Figure 5-2 shows that as the curing time is extended then the concentration above the

chloride threshold level is reduced. This shows that the microstructure is being refined over time. This also supports an expected lower value for the D_c.

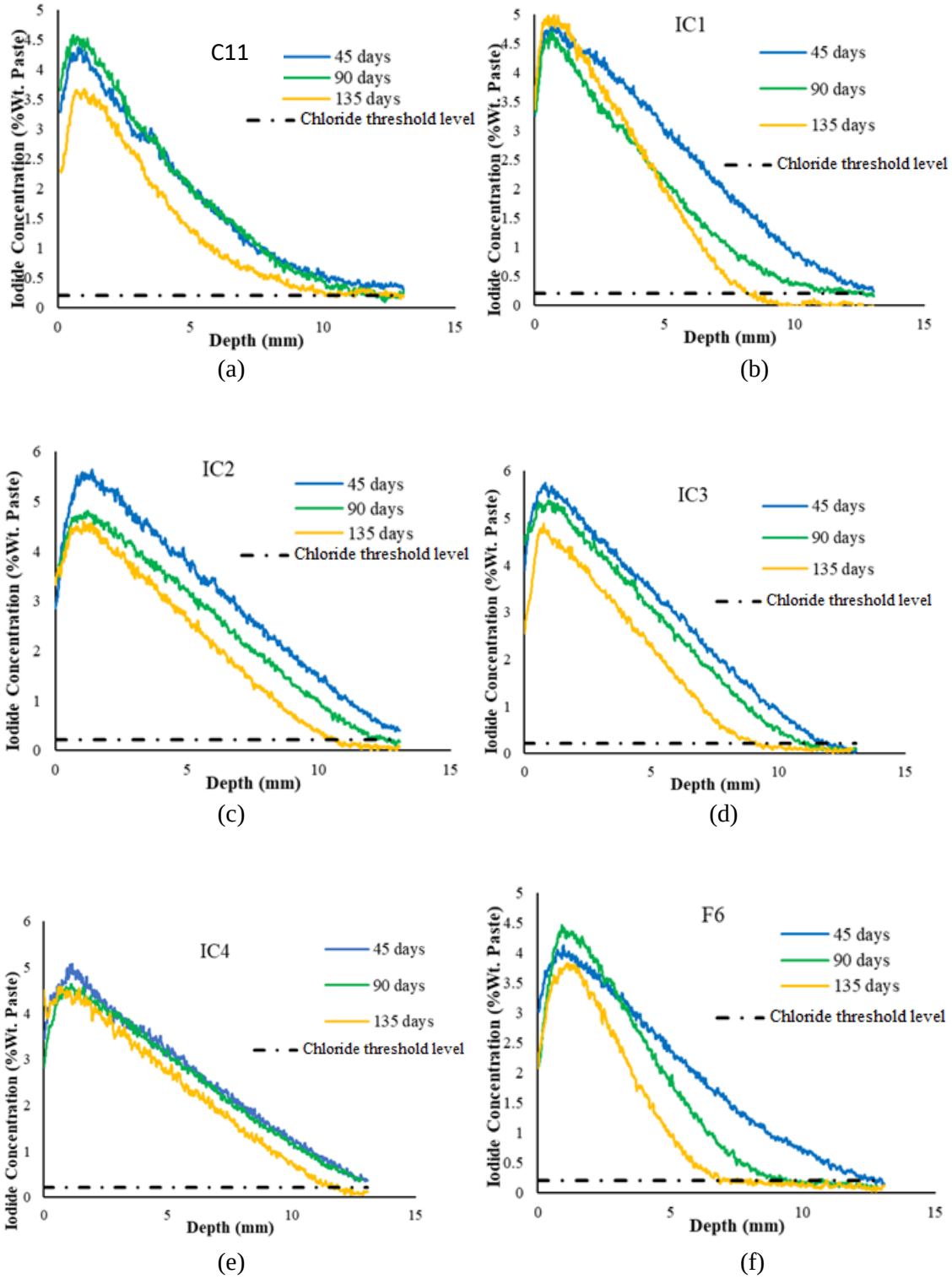

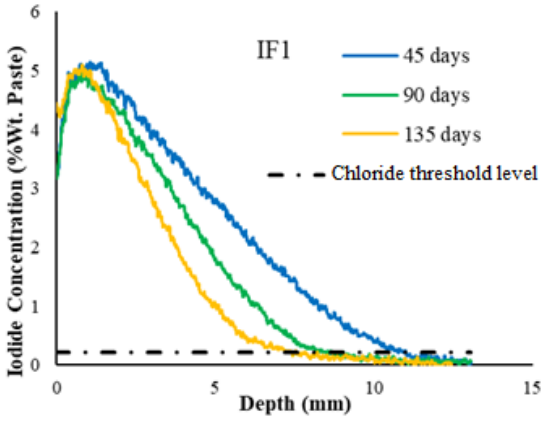

(g)

Figure 5-2. Concentration profiles of the seven types of fly ashes cured for three different times: a) C11, b) IC1, c) IC2, d) IC3, e) IC4, f) F6, and g) IF1.

The quantitative results extracted from the concentration profiles shown in Figure 5-2 are reported in Table 5-3. The degree of saturation for all the samples tested ranged from 81.6% to 92.3%. The depth of penetration seems to be correlated to the diffusion coefficient. This is logical as the diffusion coefficient gives insights into the ion penetration into the sample.

The average coefficient of variance (CV) of D_c for all paste mixtures in this study is equal to 13.4%. The CV for D_c of concrete samples using CHIP is shown to be equal to 25% Chapter IV. Low values of CV in this technique in comparison to other test methods like NT Build 492 test with high range of coefficient of variability (CV= 0.46% to 34.66%), especially when fly ash and other supplementary cementitious materials (SCMs) are used, shows that the applied CHIP imaging technique has enough accuracy to draw reliable conclusions [23].

Table 5-3. Mass transport properties of fly ash

Curing time	Mass transport properties	C11	IC1	IC2	IC3	IC4	F6	IF1
45 days	C_s (%Wt. Paste)	4.77 (0.86)*	5.62 (0.18)	6.55 (0.36)	6.74 (0.19)	5.61 (0.0.47)	4.80 (0.14)	6.31 (0.41)
	D_c ($\times 10^{-11}\ m^2/s$)	0.808 (1.70)	1.19 (1.10)	1.45 (2.40)	1.03 (0.96)	1.43 (2.70)	1.03 (1.50)	0.751 (1.60)
	Penetration depth (mm)	>13	>13	>13	11.92	>13	12.71	11.09
90 days	C_s (%Wt. Paste)	5.17 (0.81)	5.22 (0.76)	5.79 (0.29)	6.53 (0.67)	5.39 (0.26)	5.73 (0.35)	6.39 (0.13)
	D_c ($\times 10^{-11}\ m^2/s$)	0.711 (1.80)	0.703 (0.83)	1.19 (1.10)	0.843 (1.10)	1.42 (1.30)	0.499 (0.57)	0.430 (1.30)
	Penetration depth (mm)	12	12.03	12.55	10.85	>13	9.39	8.51
135 days	C_s (%Wt. Paste)	4.42 (0.04)	6.30 (0.38)	5.64 (0.37)	5.93 (0.34)	5.35 (0.24)	5.28 (0.36)	6.70 (0.45)
	D_c ($\times 10^{-11}\ m^2/s$)	0.518 (1.95)	0.453 (0.99)	0.816 (1.40)	0.568 (1.30)	1.04 (2.90)	0.310 (0.27)	0.261 (0.28)
	Penetration depth (mm)	10.08	8.18	10.60	9.13	11.86	6.83	7.40

*Values in parenthesis represent the standard deviation from four measurements of each mixture.

Figure 5-3 compares the D_c and porosity of the samples. The D_c is shown as bar charts and the porosity is shown as a dashed line. The results show that the porosity and D_c both decrease with curing, but these changes are not proportional.

For D_c when the curing time was increased from 45 days to 90 days the D_c improved by 26.3% on average and the porosity improved by 3.2%. Between 45 days and 135 days, the D_c improved by 49.8% on average and the porosity changed by 6.15%. This highlights how porosity is the measurement of the pore volume and the mass transport and therefore the permeability is a function of how interconnected those pores are inside the material. Porosity and D_c results shown in Figure 5-3 reveal that porosity measurement is not sufficient to evaluate or predict the durability performance of a sample. For instance, all of the mixtures had a very close porosity at 45 days of curing while their D_c values differed considerably from one mixture to another.

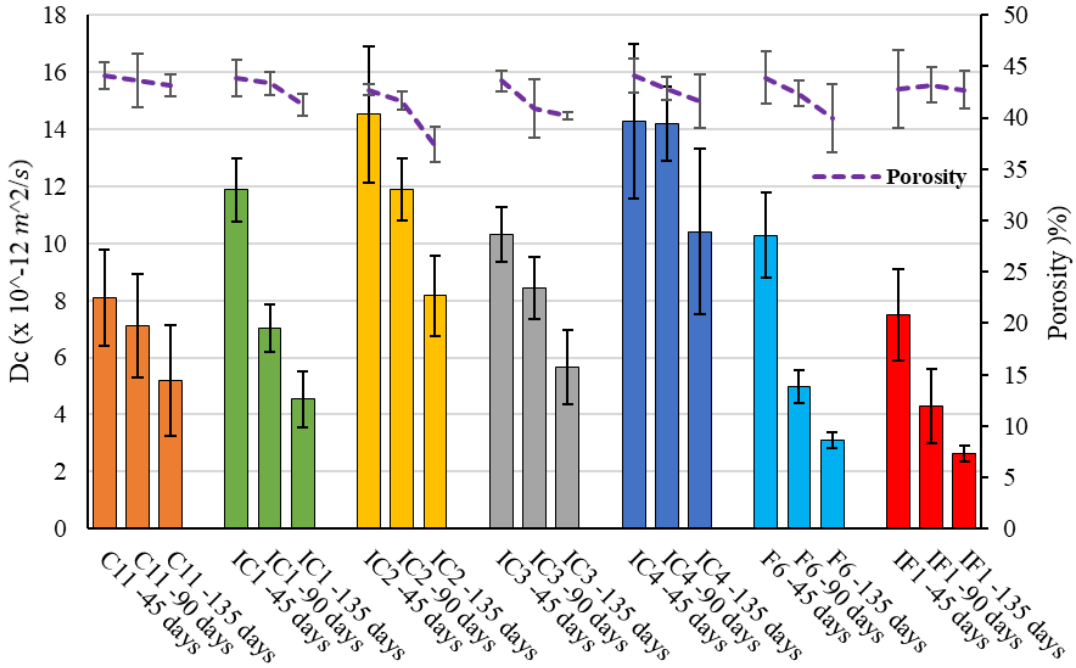

Figure 5-3. Porosity and diffusion coefficients (D_c)

5.4. Practical Implications

Unit costs per cubic yard of fly ash concrete will usually be less than similar concrete without fly ash. One of the concerns using fly ash in concrete is the absence of the durability performance of these materials. Even, it is not easy for a concrete durability modeler to distinguish between an OPC cement and a blended cement. It would be beneficial if the properties of different materials that are desirable for modelers be represented in a single term for easy comparison and judgment. This study used a medical x-ray scanner to directly observe the fluid transport into the paste fly ash samples and evaluate their durability performance by reporting D_c. The outputs of this experiment serve both contractors and modelers. This study showed that D_c can help practitioners make informed decisions in choosing a fly ash source that will help them obtain improved durability against external fluid ingress into concrete. D_c by summarizing different impacting parameters in one term represents the multi mechanism of mass transport into concrete more realistic.

The applied test method in this study could be used to evaluate fly ash that does not meet current specifications but may show great promise or it could be used to investigate the potential use in concrete. This becomes more important when suitable fly ashes are not available near the construction site and fly ash transportation costs may nullify any cost advantage. There is also potential variability of the fly ash quality from the same source. Therefore, the test method applied in this study can be used as a preliminary test to judge the quality and performance of each fly ash before using it in a project.

The results of this study showed how different fly ashes even if are in the same classification (Class C or F) do not result in obtaining similar performances. In other words, not all fly ashes have the same pozzolanic activity to provide good results in concrete. In addition, the results of this study showed that microstructure is being refined over time and maybe longer curing time in comparison to OPC is needed for blended cements to reach their highest possible performance level. This work also showed that some traditional measurements like porosity do not give sufficient insight into the concrete performance.

5.5. Conclusions

The present work employs dental x-ray radiography (CHIP) to investigate the impact of curing time on the ion diffusivity of blended cement-fly ash paste. CHIP by having a low coefficient of variance (CV) values gives quite reasonable results for the diffusion coefficients (D_c) through cement paste. The diffusion test method adopted in this study along with the x-ray imaging technique provided an approach to study the multi-mechanism of ion movement into a sample without applying any external force like the electric field. For this reason, the obtained results of this investigation give a better insight into the performance of blended cement-fly ash paste samples. From the results, it was observed that:

- Extending the curing time of blended cement with fly ash reduces the D_c. On average, for all the tested fly ashes the D_c improved by 26.3% for 90 days of curing compared to 45 days of curing. Increasing the curing time from 45 days to 135 days resulted in 49.8% D_c improvement on average for all mixtures.

- Increasing the curing time results in a denser structure and lower porosity. Lower porosity helps to get less diffusivity.

- The results show that the porosity and D_c both decrease with curing, but these changes are not proportional.

- Porosity measurement is not sufficient to evaluate or predict the durability performance of a sample.

- The average coefficient of variance (CV) of D_c for all paste mixtures in this study is equal to 13.4%. The CV for D_c of concrete samples using CHIP is shown to be equal to 25%. Low values of CV in this technique in comparison to other test methods show the applied CHIP imaging technique has enough accuracy to draw reliable conclusions.

Acknowledgments

The authors would like to express their great appreciation to Dr. Daniel Cook for his valuable and constructive suggestions on this project. The authors would like to thank Ms. Megan Buchanan for helping during the sample preparation.

References

[1] K.O. Ampadu, K. Torii, M. Kawamura, Beneficial effect of fly ash on chloride diffusivity of hardened cement paste, Cement and Concrete Research. 29 (1999) 585–590. doi:https://doi.org/10.1016/S0008-8846(99)00047-2.

[2] Y.-S. Choi, J.-G. Kim, K.-M. Lee, Corrosion behavior of steel bar embedded in fly ash concrete, Corrosion Science. 48 (2006) 1733–1745. doi:https://doi.org/10.1016/j.corsci.2005.05.019.

[3] M.D.A. Thomas, M.H. Shehata, S.G. Shashiprakash, D.S. Hopkins, K. Cail, Use of ternary cementitious systems containing silica fume and fly ash in concrete, Cement and Concrete Research. 29 (1999) 1207–1214. doi:https://doi.org/10.1016/S0008-8846(99)00096-4.

[4] P. Chindaprasirt, C. Chotithanorm, H.T. Cao, V. Sirivivatnanon, Influence of fly ash fineness on the chloride penetration of concrete, Construction and Building Materials. 21 (2007) 356–361. doi:https://doi.org/10.1016/j.conbuildmat.2005.08.010.

[5] Y. Zhang, W. Sun, Z. Liu, S. Chen, One and two dimensional chloride ion diffusion of fly ash concrete under flexural stress, Journal of Zhejiang University-SCIENCE A. 12 (2011) 692–701. doi:10.1631/jzus.A1100006.

[6] M. Kuroda, T. Watanabe, N. Terashi, Increase of bond strength at interfacial transition zone by the use of fly ash, Cement and Concrete Research. 30 (2000) 253–258. doi:https://doi.org/10.1016/S0008-8846(99)00241-0.

[7] E. Zornoza, J. Payá, P. Garcés, Chloride-induced corrosion of steel embedded in mortars containing fly ash and spent cracking catalyst, Corrosion Science. 50 (2008) 1567–1575.

[8] W. Chalee, M. Teekavanit, K. Kiattikomol, A. Siripanichgorn, C. Jaturapitakkul, Effect of W/C ratio on covering depth of fly ash concrete in marine environment, Construction and Building Materials. 21 (2007) 965–971. doi:https://doi.org/10.1016/j.conbuildmat.2006.03.002.

[9] R.K. Dhir, M.R. Jones, Development of chloride-resisting concrete using fly ash, Fuel. 78 (1999) 137–142. doi:https://doi.org/10.1016/S0016-2361(98)00149-5.

[10] I. De la Varga, R.P. Spragg, C. Di Bella, J. Castro, D.P. Bentz, J. Weiss, Fluid transport in high volume fly ash mixtures with and without internal curing, Cement and Concrete Composites. 45 (2014) 102–110. doi:https://doi.org/10.1016/j.cemconcomp.2013.09.017.

[11] M.D.A. Thomas, P.B. Bamforth, Modelling chloride diffusion in concrete: Effect of fly ash and slag, Cement and Concrete Research. 29 (1999) 487–495. doi:https://doi.org/10.1016/S0008-8846(98)00192-6.

[12] A. Boddy, E. Bentz, M.D.A. Thomas, R.D. Hooton, An overview and sensitivity study of a multimechanistic chloride transport model, Cement and Concrete Research. 29 (1999) 827–837. doi:https://doi.org/10.1016/S0008-8846(99)00045-9.

[13] ASTM C150, Standard Specification for Portland Cement, (2019).

[14] ASTM C618, Standard Specification for Coal Fly Ash and Raw or Calcined Natural Pozzolan for Use, (2019) 1–3.

[15] ASTM C305, Standard Practice for Mechanical Mixing of Hydraulic Cement Pastes and Mortars of Plastic Consistency, (2006).

[16] ASTM C511, Standard Specification for Mixing Rooms, Moist Cabinets, Moist Rooms, and Water Storage Tanks Used in the Testing of Hydraulic Cements and Concretes, (2019).

[17] M. Khanzadeh Moradllo, Q. Hu, M.T. Ley, Using X-ray imaging to investigate in-situ ion diffusion in cementitious materials, Construction and Building Materials. 136 (2017) 88–98.

[18] M. Khanzadeh Moradllo, M.T. Ley, Comparing ion diffusion in alternative cementitious materials in real time by using non-destructive X-ray imaging, Cement and Concrete Composites. 82 (2017) 67–79. doi:10.1016/J.CEMCONCOMP.2017.05.014.

[19] M.D.A. Thomas, R.D. Hooton, A. Scott, H. Zibara, The effect of supplementary cementitious materials on chloride binding in hardened cement paste, Cement and Concrete Research. 42 (2012) 1–7. doi:https://doi.org/10.1016/j.cemconres.2011.01.001.

[20] C. Qiao, P. Suraneni, T.N.W. Ying, A. Choudhary, J. Weiss, Chloride binding of cement pastes with fly ash exposed to CaCl2 solutions at 5 and 23° C, Cement and Concrete Composites. 97 (2019) 43–53.

[21] T. Ishida, S. Miyahara, T. Maruya, Chloride binding capacity of mortars made with various Portland cements and mineral admixtures, Journal of Advanced Concrete Technology. 6 (2008) 287–301.

[22] ASTM C642, Standard Test Method for Density, Absorption, and Voids in Hardened Concrete, (2013) 4–6.

[23] K.R. Larsen, Study Evaluates Chloride Limits for Structural Reinforced Concrete, (2017).

[24] MATLAB (R2016a), version 9.0.0, (2016).

[25] L. Kocsis, P. Herman, A. Eke, The modified Beer–Lambert law revisited, Physics in Medicine & Biology. 51 (2006) N91.

[26] L. Cavé, T. Al, Y. Xiang, P. Vilks, A technique for estimating one-dimensional diffusion coefficients in low-permeability sedimentary rock using X-ray radiography: Comparison with through-diffusion measurements, Journal of Contaminant Hydrology. 103 (2009) 1–12.

[27] V.C. Tidwell, L.C. Meigs, T. Christian-Frear, C.M. Boney, Effects of spatially heterogeneous porosity on matrix diffusion as investigated by X-ray absorption imaging, Journal of Contaminant Hydrology. 42 (2000) 285–302.

[28] Curve fitting toolbox : for use with MATLAB® : user's guide, (2001).

APPENDICES

Appendix A. CHIP imaging technique

This method was established and developed for the first time at Oklahoma state university. This technique works very similarly to the transmission x-ray microscopy (TXM) technique. It has been shown that TXM is a reliable technique when mass transport investigation within cementitious materials is desired [19]. The only differences between CHIP and TXM are the x-ray source and x-ray settings. Like TXM, in the CHIP imaging technique, each sample was loaded on a fixed stage between the x-ray source and the detector as shown in Figure 5-1.Ap. When x-rays hit the loaded sample, some parts of the x-rays were absorbed by the sample and some others passed the sample to reach the detector. Detector produced simple grayscale 2-D projection radiographs based on the received x-rays. The schematic view of the mechanism of imaging in this method is shown in Figure 5-2.Ap. The settings used for imaging with the designed equipment are summarized in Table 5-1.Ap. In the captured radiographs, pure black has a gray value of "0" and pure white has a gray value of "255". Values in between make up the different shades of gray. The gray value changes by density, thickness, chemistry, or a combination of them. Denser or thicker materials absorb more x-rays and can be seen brighter in the CHIP radiographs. Air absorbs less x-ray and has been commonly displayed as black in the background of each radiograph. In diffusion testing, as the tracer solution penetrates a sample, it increases the gray value of the penetrated depths and therefore the affected regions become brighter compared to the reference radiograph. By a simple image processing, each radiograph can be converted to the radiograph seen in the TXM technique. In

TXM radiographs, denser or thicker materials look darker compared to materials with less x-ray absorption capability. All the conversion process is described in detail in Chapter IV.

Since each radiograph should be compared with its reference radiograph, it is necessary to get identical radiographs at each interval of scanning. For taking consistent radiographs for each sample an appropriate stage as shown in Figure 5-3.Ap was designed to be matched with the attached nut on the samples to fix the position of the samples in the X-ray scanner. This stage forced the user to load the sample in a constant manner and scan the same side of the samples at each considered interval. Keeping the direction constant becomes more important when composite materials like concrete samples are investigating. A small rotation of the sample or minor differences in the angle of scanning in the reference radiograph compared to the other radiographs leads to imperfect image alignment.

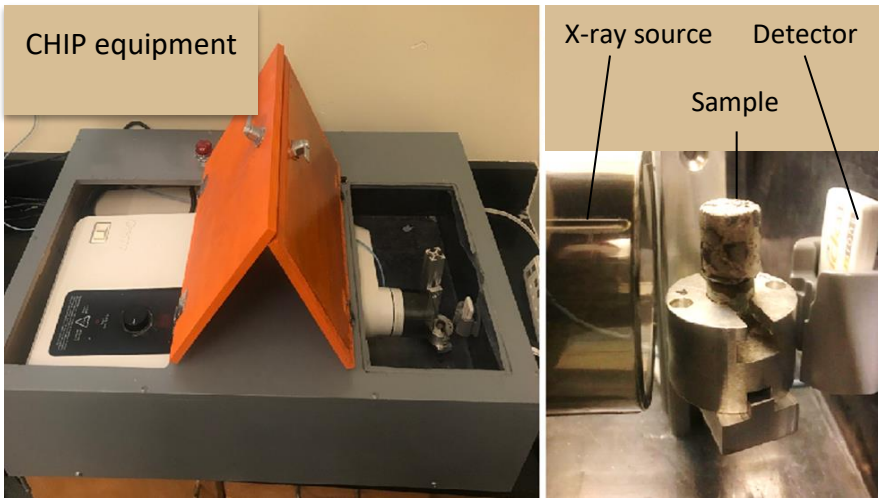

Figure 5-1.Ap. A sample loaded in the x-ray scanner

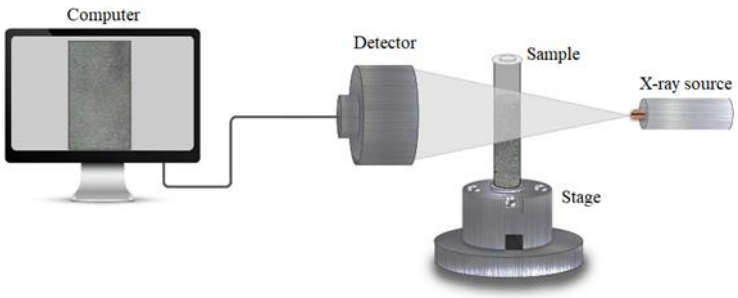

Figure 5-2.Ap. Schematic view of the mechanism of imaging in CHIP method

Figure 5-3.Ap. The designed stage for holding the sample

Table 5-1.Ap. Settings used in CHIP imaging technique

Parameter	Setting
Pixel size (μm)	15
Voltage (Kev)	120
Current (μA)	7000
Filter	Al
Exposure timeout (s)	8
Exposure time (pulses)	7

To analyze the taken radiographs, a software programming code [24] with minimal user intervention was prepared to invert the grayscale of the radiographs and to align the images taken at other intervals with their reference images. Inverting the grayscale means to change the gray values of “0” to “255” and “255” to “0”. The detailed expatiations of the inverting process are provided in Chapter IV. Alignment of the radiographs means applying local displacements (i.e. shifting and rotating) to the all taken radiographs of one individual sample in a way to establish a

point-by-point correspondence between all radiographs and the reference radiograph. Then, to get the average of gray values at each depth for each sample, the central region of each radiograph with a width of 0.88 mm (approximately 60 columns of pixels) as shown in Figure 5-4.Ap-A was

considered to eliminate cupping artifact[2]. Each line passed from a column of the pixels returns a gray value profile like what is shown in Figure 5-4.Ap-B. The final gray value profile was a depth-by-depth average of all 60 gray value profiles for each taken radiograph. The averaged gray value profile for each radiograph was subtracted from the final gray value profile of the reference radiograph correlated to a single sample in the logarithm scale to calculate attenuation ($\Delta\mu$) according to Beer-Lambert Law in Eq. (5-3) [25–27].

$$(\Delta\mu)\, x = \ln (I_{ref})\, x - \ln (I_t)\, x \qquad \text{Eq. (5-3)}$$

Where $(I_{ref})\, x$ was the transmitted x-ray intensity (gray value) at each depth (x) in the reference radiograph and $(I_t)\, x$ was the transmitted x-ray intensity at the same depth in other radiographs taken at other intervals. Finally, the calculated attenuations were converted to concentration by using calibration curves as described in Appendix.B. By having the concentration profiles and using curve fitting toolbox [28] by defining the Fick's second law equation as represented in Eq. (5-4), diffusion coefficient (D_c) and surface concentration (C_s) can be found. The last two parameters are important within service life modeling to predict the life span of each structure. The diffusion coefficient obtained from this test method combines the impact of fluid transport mechanisms of diffusion, absorption, and chemical binding in one term. For this reason, the diffusion coefficient

[2] Cupping artifact refers to a locally bright appearance along the periphery of a sample. Because the tested samples were small cores with cylindrical shape, the center of the sample is denser than the regions near the sides. For this reason, the x-ray beam is "hardened" by passing through the center region of the sample and the mean photon energy will be higher around the center. Since higher energy photons are less attenuated by denser region, the beam will be less attenuated versus identical material near the sides.

obtained from the observation of the applied technique in this study provides a more realistic insight into the fluid transport into the concrete.

$$C_{(x,t)} = C_s\left(1 - \mathrm{erf}\left(\frac{x}{2\sqrt{D_c t}}\right)\right) \quad C_{(x,0)} = 0 \;\; x > 0, \;\; C_{(0,t)} = C_s \;\; t \geq 0 \qquad \text{Eq. (5-4)}$$

Where x is the distance from sample surface; t denotes time; D_c is diffusion coefficient; C_s is surface iodide concentration; C(x,t) represents iodide concentration at the depth of x from the surface after time t; and erf is the error function.

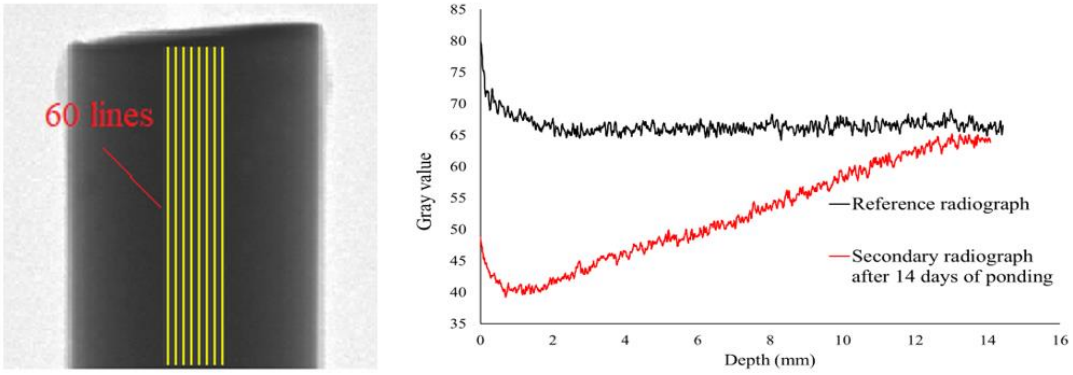

(a) (b)

Figure 5-4.Ap. (a) An inverted radiograph with the considered region in data analyzing and (b) gray value profile of one line

Appendix B. Calibration curves

Calibration curves help to convert attenuation values (Δμ) to concentration values. To develop the calibration curves, standard samples with the same mixture proportions and known iodide concentration were made by adding different iodide concentrations to the mixtures during mixing. Then the standard samples were scanned and analyzed like what was stated in the Appendix. A. After scanning the standard samples, the attenuation correlated to each concentration was extracted. Ultimately, a curve was fitted on the plotted spots (concentration vs. attenuation) to get an equation that converts the attenuation to the concentration. Figure 5-5.Ap shows the calibration curve used for this study to convert the attenuation to iodide concentration.

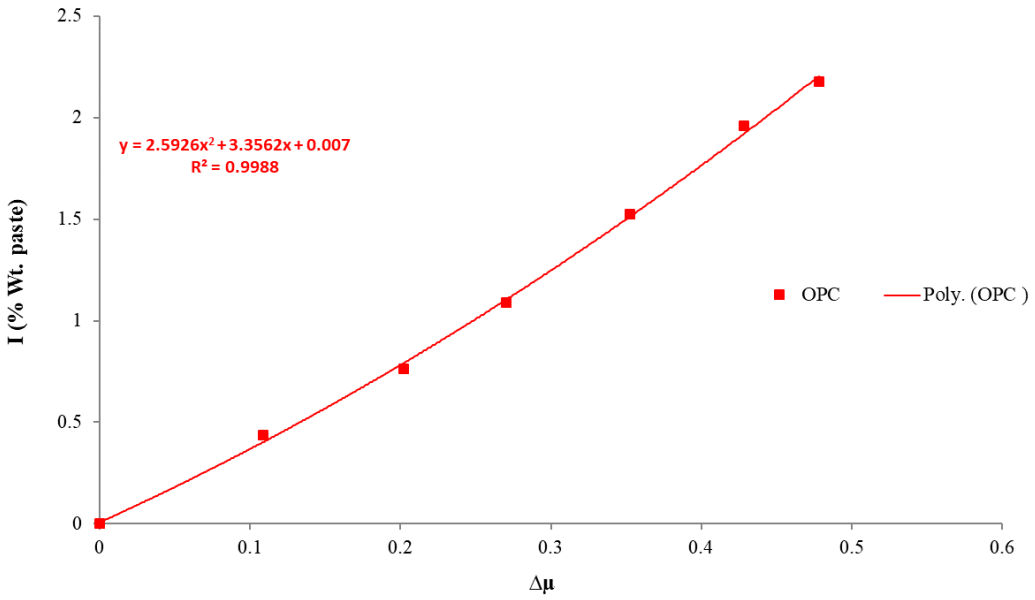

Figure 5-5.Ap. Calibration curve used for converting attenuation to iodide concentration

CHAPTER VI

CONCLUSION

This dissertation aims to show the validity and usefulness of several X-ray imaging techniques to measure the penetration of outside chemicals into cementitious systems. This work was done on a wide variety of materials and also established a new X-ray imaging method called the CHIP (Checking Ion Penetration).

6.1. Impact of Curing Time on The Mass Transport of Alternative Cementitious Materials (ACMs)

- The diffusion coefficient (D_c) for ordinary Portland cement (OPC) was consistent between 35 d to 180 d and then there was a 48% improvement in performance from 180 d to 365 d.

- The D_c for calcium aluminate cement (CAC3) increased over time because of cracking caused by the conversion. After 365 d the pore structure seems to be interconnected and this allows the iodide to freely penetrate into the sample.

- For calcium sulfoaluminate belite cement (CSA2), there was not much change in the D_c between 35 d and 90 d, however, after 180 d and 356 d, the D_c decreased by 50% and 66%, respectively.

- The D_c and ion penetration for calcium sulfoaluminate belite cement with polymer additive (CSA2B) was the lowest of all the samples investigated. After 35 d of hydration, there was minimal penetration of the iodide into the sample.

- For alkali-activated binder with a Class C fly ash (AA1), the most effective curing time between those investigated is 365 d with a 93% improvement in D_c compared to the values measured at 35 d. The reduction in the D_c also reduced the depth of penetration of the iodide into the sample to values that are comparable to OPC.

- Porosity is not a useful parameter for evaluating the Dc or depth of penetration for the binders investigated. The direct measurement of the Dc obtained from the transmission X-ray microscopy (TXM) test method provides a more realistic insight into the fluid transport into the concrete.

6.2. Laboratory and Field Investigation of Alternative Cementitious Material Resistance to Chloride Penetration Using X-Ray Imaging

- For CAC3, 14 days of lab curing was not enough to reflect the long-term performance of the field sample. CAC3 lab results showed an excellent durability performance against Cl penetration while CAC3 field samples with 6 years old showed poor resistance to Cl transport.

- The CAC3 lab sample was the only ACM to show a higher surface concentration than OPC. This suggests a higher level of surface binding. This was important as it will decrease the level of ions that penetrate into the concrete. This was not the case for the CAC3 field sample.

- There was a good agreement between laboratory and field results for CSA2B and AA1 because both lab and field results showed CSA2B and AA1 have worse resistance to Cl penetration than OPC. This matches the laboratory results.

- CSA2B and AA1 binders showed minimal binding both in the lab and field.

- Porosity by itself does not represent the performance of concrete against fluid transport into concrete because the void distribution and connectivity play important roles in this process.

6.3. Using Medical X-Ray Machines to Determine the Service Life of Concrete

- The average variability between the diffusion coefficients (D_c) for paste and concrete from CHIP and TXM is 1.02%.

- The average coefficient of variance (CV) and standard deviation (Std.) for the D_c values calculated for the all paste samples tested with CHIP is equal to 13.4% and 1.38×10^{-12} m^2/s, respectively. While the CV and Std. values for concrete is equal to 24.2% and 3.498×10^{-12} m^2/s, respectively. The higher variability values of the concrete samples compared to the paste samples is likely due to the inhomogeneity nature of the concrete samples.

- The variability from three different angles on the same sample (CV≈ 22%) is similar to the variability from three different samples from the same mix (CV≈ 24%). One solution to decrease the variability of CHIP is to scan a sample from different angles or use cubic-cut samples.

- There is strong repeatability of the CHIP by a single user with CV equal to 1.7% and Std. of 3.3×10^{-13} m^2/s. This shows that the CHIP can produce highly reproducible measurements.

6.4. Impact of Curing Time on The Ion Diffusivity of Fly Ash Pastes by X-Ray Imaging

- Extending the curing time of blended cement with fly ash reduces the D_c. On average, for all the tested fly ashes the D_c improved by 26.3% for 90 days of curing compared to 45 days of curing. Increasing the curing time from 45 days to 135 days resulted in 49.8% D_c improvement on average for all mixtures.

- Increasing the curing time results in a denser structure and lower porosity. Lower porosity helps to get less diffusivity.

- The results show that the porosity and D_c both decrease with curing, but their changes are not proportional.

- Porosity measurement is not sufficient to evaluate or predict the durability performance of a sample.

- The average CV of Dc for all paste mixtures in this study is equal to 13.4%. The CV for Dc of concrete samples using CHIP is shown to be equal to 25%. Low values of CV in this technique in comparison to other test methods show the applied CHIP imaging technique has enough accuracy to draw reliable conclusions.

These results show that the CHIP is a promising test method to rapidly evaluate the ion penetration of cementitious materials.

6.5. Future work

The researches presented in this study open up new subjects for future studies to evaluate the durability performance of a cementitious system more systematically. The following is a list of proposed future work:

1- CHIP technique can be used to study the fluid transport properties of blended ACMs +OPC.

2- CHIP and μXRF techniques can be applied to study the agreement between lab and field data for calcium aluminate cement (CAC3) by considering long curing times for the lab samples.

3- CHIP can be used to study other durability issues like sulfate attack, physical salt attack, salt scaling, sulfate attack. All these environments will cause damages to the concrete structure and therefore the mass transport properties of concrete will change by being in such mediums.

4- The CHIP can be applied to other cementitious systems like latex modified concrete, surface treatments concretes to study the performance of concrete in a complex system.

5- The research presented on fly ash could be extended to investigate the impact of a higher percentage of fly ash replacement on mass transport properties of fly ash blended systems.

VITA

Amir Behravan

Candidate for the Degree of

Doctor of Philosophy

Dissertation: INVESTIGATION OF ION DIFFUSION IN CEMENTITIOUS MATERIALS WITH X-RAY IMAGING TECHNIQUES

Major Field: Civil Engineering

Biographical:

Education:

Completed the requirements for the Doctor of Philosophy in Civil Engineering at Oklahoma State University, Stillwater, Oklahoma in July, 2020.

Completed the requirements for the Master of Science in Civil Engineering at Isfahan University of Technology, Isfahan, Iran in 2012.

Completed the requirements for the Bachelor of Science in Civil Engineering at Islamic Azad University- Khomeinishahr Branch, Isfahan, Iran in 2009.

Experience:

Graduate Research Assistant, Oklahoma State University, Stillwater, OK, 2016-2020.
Primary Lecturer, Islamic Azad University, Isfahan, Iran, 2012-2016.
Site engineer, Bazm Road and Construction Company, Isfahan, Iran, 2012-2014.

Professional Memberships:

American Concrete Institute (ACI), student member	September 2017-Present
The Masonry Society (TMS), member	September 2017-Present
Iran Construction Engineering Organization (IRCEO)	September 2013-Present
Iranian Concrete Institute, member	April 2011- present
Young Researchers and Elite Club, member	March 2011- Present